Dissertation

submitted to the
Combined Faculties of the Natural Sciences and Mathematics
of the Ruperto-Carola-University of Heidelberg, Germany
for the degree of
Doctor of Natural Sciences

Put forward by

Giovanni Cerchiari, M.Sc.

born in Monza (MB), Italy

Oral examination: 18-04-2018

Laser spectroscopy of La⁻ and anion trapping with a view to laser cooling

Referees: PD Dr. Alban Kellerbauer
                PD Dr. Wolfgang Quint

Kurzzusammenfassung auf Deutsch

Eine direkte Laserkühlung von negativen Ionen wurde noch nicht erreicht. Eine wichtige potentielle Anwendung dieser Technik ist das sympathetische Kühlen von Antiprotonen durch gekühlte negative Ionen. Antiwasserstoff, der unter Verwendung von kalten Antiprotonen hergestellt wurde, eignet sich für fundamentale Untersuchungen wie Tests der CPT-Symmetrie und des schwachen Äquivalenzprinzips mit Antimaterie.

Das negative Lanthan-Ion wurde als ein guter Kandidat für die Laser-Kühlung in Rahmen dieser Arbeit durch Laserspektroskopie identifiziert. Ein Strahl von Lanthanan-Ionen von einigen keV Energie wurde mit einem abstimmbaren Laser angeregt. Die Lichtstrahlung wurde den Ionen sowohl in einer kollinearen als auch in einer transversalen Anordnung überlagert, um den Laserkühl-Übergang zu untersuchen.

Mit dem Ziel der ersten Realisierung der Laser-Kühlung wurde der Einfang von Anionen in einer Penning-Falle und einer Paul-Falle studiert, um die Interaktionszeit von Anionen und Licht zu erhöhen. Mit beiden Fallen wurden detaillierte Messungen durchgeführt, um die besten Bedingungen für den Einfang von Anionen zu finden. Alle Fallenparameter wurden in Hinblick auf eine hohe Einfangeffizienz sowie optimale Eigenschaften des eingeschlossenen Ionenplasmas optimiert.

English abstract

Direct laser cooling of negative ions has not yet been achieved. An important potential application of this technique is the use of cooled negative ions to sympathetically cool antiprotons. Antihydrogen, synthesized from cold antiprotons, is suitable for fundamental studies tests of CPT symmetry and the weak equivalence principle with antimatter.

During this work, the negative lanthanum ion was identified as a good candidate for laser cooling using in-flight spectroscopy. Lanthanum anions were produced as a beam with a kinetic energy of a few keV and were excited using a tunable laser. The light radiation was superimposed to the ions both in a collinear and in a transverse setup to study the laser cooling transition.

Trapping of anions both in a Penning trap and in a Paul trap was demonstrated as a prerequisite to increase the interaction time of anions and light towards the first realization of laser cooling. Detailed studies were performed both traps to find the best conditions for anions capture. All trap parameters were optimized with a view to a high capture efficiency as well as optimal properties of the confined plasma.

Parts of this work have been published or prepared in the following references:

A. Kellerbauer, G. Cerchiari, E. Jordan, "High-resolution laser spectroscopy on bound–bound transitions in La⁻", *Phys. Scr.* **90**, 054014 (2015)

E. Jordan, G. Cerchiari, S. Fritzsche, A. Kellerbauer, "High-Resolution Spectroscopy on the Laser-Cooling Candidate La⁻", *Phys. Rev. Lett.* **115**, 113001 (2015)

G. Cerchiari, A. Kellerbauer, M. S. Safronova, U. I. Safronova, P. Yzombard "Ultracold anions for high-precision antihydrogen experiments", *submitted* (2018)

To Miranda

Contents

Introduction

The binding energy of an extra electron to an atom, called electron affinity, is typically weak. However, stable negative ions exist for the majority of the elements. Among the elements, the electron affinity ranges from zero to the maximal value for chlorine of 3.6 eV and is, in general, of the order of 1 eV. No stable doubly charged atomic anions have been observed [11]. This fact can be taken as an indication of how fragile this bound is.

In physics, the interest in observing negative ion systems stems from the fact that their structure is qualitatively different from neutral particles or positive ions. The differences are caused by the short-range interaction between the extra electron and the neutral core. Within the mean-field approximation, the electron is bound by the dipole potential induced on the electric charge distribution in the atom. The new electron polarizes the neutral atom by pushing away the other electrons that are screening the positively charged nucleus, and remains captured in the resulting dipole potential. However, the dipole potential falls off as a function of distance faster than the attractive Coulomb potential that represents the main Hamiltonian term of electrons bound to an atom. The dipole interaction has a short range, and anions do not show a Rydberg series of states but have few, if any, excited states. On the other hand, all negative ions possess many unstable excited states which are embedded as resonances in the energy continuum associated with an atom and a free electron. Negative ions, therefore, offer the unique opportunity to study short-range potentials on an atomic scale.

Spectroscopic studies on atomic systems can give insights into their properties, enhancing theoretical predictions towards more accurate mathematical descriptions. In anions, the electron correlations and relativistic effects may produce significant corrections in the model of their structure. Theoretical studies are often performed by computations on extensive sets of eigenstates of the Hamiltonian to correctly evaluate the interplay relations among electrons. For example, discrepancies in the predictions of the excitation energies of La^- are to date as high as $17\ldots33\%$ [60, 82], and only recently new calculation carried out by M. Safranova in the context of this thesis improved our understanding of the system, matching the measured values within approximately 2% precision.

The principle of most of the experimental observations on negative ions is based on the removal of the extra electron for detection. Conversely, fluorescence or absorption measurements are very challenging in most cases. The probing radiation is typically in the infrared region where no high-efficiency detectors are available, and cross-sections are usually low. Stripping the electron from the ion is therefore preferred. The method allows measuring a massive particle instead of photons, thus increasing the sensitivity very close to single detachment events.

In this way, in the 1970s the first bound states with opposite parity from the ground state were observed in negative ions. Laser-based experiments on alkali elements revealed narrow transitions in Rb^- and Cs^- close to the neutralization threshold [3, 6]. The adopted photodetachment spectroscopy technique provided the first accurate experimental determinations of the electron affinities of alkali atoms, revealing resonances which, at the time, were the narrowest observed in electron–atom systems. Despite the first encouraging results, the theoretical challenge of describing anions was tackled only twenty years later. More systematic calculations on heavy atomic anions were undertaken, and, in addition to the alkalis Rb^-, Cs^- and Fr^- [20], new elements were predicted to have similar opposite-parity states.

There now exist predictions for La⁻ [22], Ce⁻ [26], Th⁻ [25], Gd⁻, Tb⁻, Pa⁻, U⁻, Np⁻, Lu⁻ and Lr⁻ [68]. Following theoretical indications, such a state with opposite parity was first found experimentally in Os⁻ [39].

These atoms are all quite heavy and locatedin the lower region of the periodic table where the orbiting electrons are relativistic, and correlation effects play crucial roles in their description. Most of them are in the lanthanide or actinide groups that contain elements that are characterized by the so-called lanthanides contraction. In the lanthanides, the last filled orbitals 5s and 5p are not external but are hidden inside the 4f sub-shell. This property causes not only very similar chemical behavior throughout all the elements in the series, but also a remarkable compactness of the atoms belonging to those periods. These negative ions are characterized by a lower separation between the ground and first excited states of opposite parity. For instance, La⁻ has nearly degenerate even and odd parity bound states between the configurations[1] [Xe]$5d^26s^2$ and [Xe]$5d6s6p^1$. The property is accompanied by a richer-than-usual sub-level structure among the anions [37], shared with the neighbor Ce⁻ [42]. Thanks to this unique feature, La⁻ was later predicted to possess a dipole-allowed bound–bound transition from the ground state suitable for Doppler laser cooling [69].

To date, laser cooling of a negative ion species has not yet been achieved. For laser cooling to take place, at least two bound states must exist in the anion: the ground state and a bound excited state. This configuration allows a photon to be absorbed, yet preserving the system's integrity with a negative charge. Many absorptions and spontaneous re-emissions of photons are typically required to achieve cooling. Thus, a dipole–allowed transition from the ground state must also ensure a fast relaxation time of the system suitable for a rapid cooling cycle. Consequently, the theoretical and experimental challenge is to find a suitable anion candidate in which a fast and closed cycle can be established that needs as few lasers as possible.

Os⁻ and La⁻ were were indicated as possible candidates for the first observation of anion laser cooling [69]. Both species of anions have been investigated at the *Max-Planck-Institut für Kernphysik* (MPIK) in Heidelberg within the *Ultracold Negative Ions by indirect laser Cooling* project (UNIC) because they were pinpointed as the most promising candidates. Osmium follows lanthanum in the same period after 19 elements and, due to the lanthanides contraction, it is the element with the highest density observed in nature. It possesses a closed dipole-allowed transition of about 1 eV photon energy to the excited state which, in turn, is just 11 meV below the detachment threshold. Osmium has seven stable isotopes, while La has only one. The most abundant isotope (¹⁹²Os) has no nuclear spin and thus no hyperfine structure in the atomic transitions. The only stable isotope ¹³⁹La has a nuclear spin of $I = 7/2$, generating a number of hyperfine spectral lines visible in the spectrum.

Following this research path, the work of this thesis focused on direct laser cooling of the negative lanthanum ion. Initially, particular attention was devoted to the structure of La⁻ and its laser cooling transition. Spectroscopic investigations gave access to the critical information of the required frequencies to establish a closed cooling cycle, as well as the typical timing of the process. Different experiments are currently investigating indirect laser cooling techniques. Following the indirect method [90], negative ions can be cooled in a mixed Paul-MOT trap where laser-cooled neutral atoms are used as a buffer gas to reduce the anion temperature prior to laser cooling.

Negative ions are important not only as systems to be observed, but also as tools. Tandem accelerators, for instance, use the negative charge and double stripping to double the kinetic energy gained in an electrostatic potential. In recent years the cold antimatter community has developed a growing interest in negative ions. Antinuclei have negative charge and can be compared and/or manipulated using ions of the same charge. Precision mass comparisons in Penning trap experiment of the mass of the proton and the antiproton (p̄) are performed by comparing the oscillation frequencies of p̄ and H⁻ in the same trap configuration [83]. At the Antiproton Decelerator (AD) facility at CERN, Penning traps are widely adopted to confine the charged p̄ and positrons (e⁺). The geometry of a Penning trap is cylindrical, with a

---

[1][Xe] denotes the xenon core electronic structure.

superconducting solenoidal coil that generates a strong and homogeneous magnetic field which provides the confinement of ions in the radial direction. Confinement of charged particles in the axial direction, i.e. along the magnetic field lines, is obtained thanks to an electric field which is given by static voltages applied to a series of cylindrical electrodes. Several electrodes, stacked one next to the other, allow shaping the axial potential. The axial confinement is more critical since it is limited by the maximum voltage that can be applied to the end cap electrodes before discharge. Radial confinement is easier, because superconducting materials and technology generate stable magnetic fields which can be as high as a few tesla[2]. Efficient trapping and cooling of $\bar{p}$ has been demonstrated by combining a mixture of electrons and $\bar{p}$ in a Penning trap [17]. Electrons confined in a magnetic field of a few tesla lose most of their kinetic energy via synchrotron radiation, reaching the temperature of the surrounding environment in a few seconds. In turn, antiprotons are cooled by interacting with electrons via the Coulomb force when confined within the same trapping volume [66].

Laser-cooled negative ions may potentially produce antiprotons at a lower temperature than achievable with the state-of-the-art method using electrons [53]. The new technique has the advantage of working both in Penning traps as well as in radiofrequency traps. Cooler antiprotons could increase the precision in the measurement of the gravitational force on anti-atoms. Antihydrogen ($\bar{H}$) at a temperature as low as 100 mK can be synthesized by a charge exchange reaction between cold $\bar{p}$ and positronium, the bound state of an electron and a positron [92]. This synthesis scheme is currently pursued by the AEgIS Collaboration at CERN (*Antimatter Experiment Gravity Interferometry and Spectroscopy*) to compare the trajectories of matter and antimatter in the gravitational field of Earth by a ballistic measurement [54].

The long-term goal of the UNIC project is the sympathetic cooling of antiprotons ($\bar{p}$) to mK kinetic energies by laser-cooled negative ions. Therefore, the apparatus at MPIK is equipped with a Penning trap because a successful demonstration of negative ion laser cooling can be easily integrated into one of the antimatter experiments. Both antiprotons and anions are negatively charged, but there are important differences between the source and the nature of the two ion species. In fact, $\bar{p}$ are delivered from the AD in bunches while the sputter source generates a monochromatic continuous stream of anions. Furthermore, atomic anions are fragile systems since low energetic collisions may detach the extra electron. A trapping technique was consequently developed during this work that allows the benefits of having a high yield of particles to overcome anion fragility. Anions have been captured in the Penning trap successfully both with and without prior loading of e^-.

However, in the Penning trap, the magnetic field that provides radial confinement also eliminates the degeneracy of atomic levels. Laser cooling thus faces further challenges connected to the splitting of the quantum energy levels due to the coupling of the angular momentum of the orbiting electrons around the core with the magnetic field (Zeeman effect). As discussed already in [84] the splitting of the lines in La$^-$ requires the adoption of a large number of lasers. For this reason, a different solution than a Penning trap may pave the way to laser cooling of negative ions with a simple laser system. There are various experimental setups without the presence of a magnetic field in the interaction region of ions and light. For example, laser cooling can be carried out on a La$^-$ beam confined in a storage ring. Such storage rings are described for instance in [13], and in [89] where a magnetic-field-free section is present or a pure electrostatic storage ring is described.

An alternative solution is to confine anions in a radiofrequency trap (Paul trap)[3], which is a widely used solution for laser cooling applications with ions. In analogy to the magnetic field of a Penning trap, in a linear Paul trap, the radial confinement is generated by a periodically oscillating electric field. In the trap designed for the UNIC apparatus during this work, the oscillating field is applied to four parallel and equidistant cylindrical electrodes, producing an alternating quadrupole potential. The time-averaged action of the oscillating field is to push ions towards the axis of the trap where the charged particles

---

[2]A general introduction about Penning traps can be found in [48], chapter 3.

[3]A general introduction about Paul traps can be found in [48], chapter 2

are confined by a static electric field. In the UNIC setup, the Paul trap is mounted downstream of the Penning trap, and has been used directly as a capture device for anions. Alternatively, it may become a secondary trap where anions are transferred after catching and pre-cooling in the Penning trap. In the latter configuration, the magnetic field must be switched off or compensated via additional coils or magnetic elements to suppress the field in the laser interaction region.

Chapter 1

Experimental setup

1.1 UNIC experiment

The experimental work reported in this thesis was carried out at the *Max-Planck-Institut für Kernphysik* (MPIK) in Heidelberg within the *Ultracold Negative Ions by indirect laser Cooling* project (UNIC). The general setup of the experiment is presented in Fig.1.1 as it appears at the time of this thesis. Over the time of this research work, it has been subject to numerous improvements and modifications.

The first section of the experiment, from ion creation to the spectroscopy section, is similar to the one described in detail in [73]. Negative ions are produced in a caesium sputter source and accelerated into a beam by an electric potential. The beam energy is tunable in the range from few hundred eV up to about 10 keV. Mass selection is performed by separating the various mass components in a dipole magnet. A few ion optical elements, such as slits, quadrupoles, einzel lenses, and steering sections, guide the beam along the beamline, improving its intensity, divergence and the quality of the mass selection. After mass filtering, the beam is directed towards two experimental regions, one containing the electromagnetic traps to confine charged particles and one devoted to spectroscopy in flight.

The traps are assembled on a straight line from the mass spectrometer to simplify the trajectory during ion catching operations. The main chamber contains a superconducting solenoid magnet whose field is oriented along the beam axis. It is the fundamental component of a cylindrical Penning trap. After the Penning trap, a linear Paul trap was further developed to perform atomic physics experiments in the absence of magnetic field. The rods of the trap are also aligned along the beam axis.

A chamber dedicated to spectroscopic studies on the beam is located at right angles to the ion direction (Ch. 2). The anions may be directed towards this section by an electrostatic deflector [67] that bends the charged particles by 90° when the appropriate voltage is applied. Along the straight section the beam is collimated by two circular apertures with radii $r = 3.25$ mm placed a distance $d = 730$ mm apart. After the last aperture two parallel-plate electrodes deflect ions into a Faraday cup for current monitoring. Neutral particles present in the beam pass straight ahead, through another 4 mm radius aperture. Four 25.4 mm windows allow introducing light into the straight section. Two windows are used to couple light collinearly with the ion beam path. The second pair of windows allows orthogonal access. The axis of the second pair of windows is 60 mm downstream of the first collimating aperture.

Several particle detectors are located along the experimental setup to control the beam properties and to acquire measurements. The ion beam current is measured directly with Faraday cups. Faraday cups are realized with a cylindrical copper electrode isolated from an external shell. The cups allow the collection of charges deposited inside that are then measured by an picoamperometer. For weaker currents down to single particle events a greater amplification is required, and we used avalanche detectors. These detectors are built by individual or bundles of channels internally covered with a low work function material with high resistivity. A voltage difference of about 1 keV is applied to the front and the back of all channels during operation. An electron stripped from the inner surface is accelerated, generating an avalanche along the wall of the channel several times before reaching the end. Single channel detectors are typically called *channeltrons* and they can reach up to 90% quantum efficiency in electron detection. Channels can be manufactured quite small, down to a few micrometers in diameter, using glass fiber technology. It is possible to arrange them in the form of a flat disc, introducing a slight tilt of the channels with respect to the surface of the disc. Several plates can be coupled in series to obtain superior gain performances. The angle tilt of the channels is favorable for the initiation of the avalanche process offering more active surface. The assembly of one or several of these plates composed of adjacent channels is called *Microchannel Channel Plate* (MCP) detector. MCP detectors can be coupled at the end to a metal anode or a phosphor screen. With both devices it is possible to capture the amplified electrical signal, but the latter has the advantage of converting the amplified current signal into a 2D image.
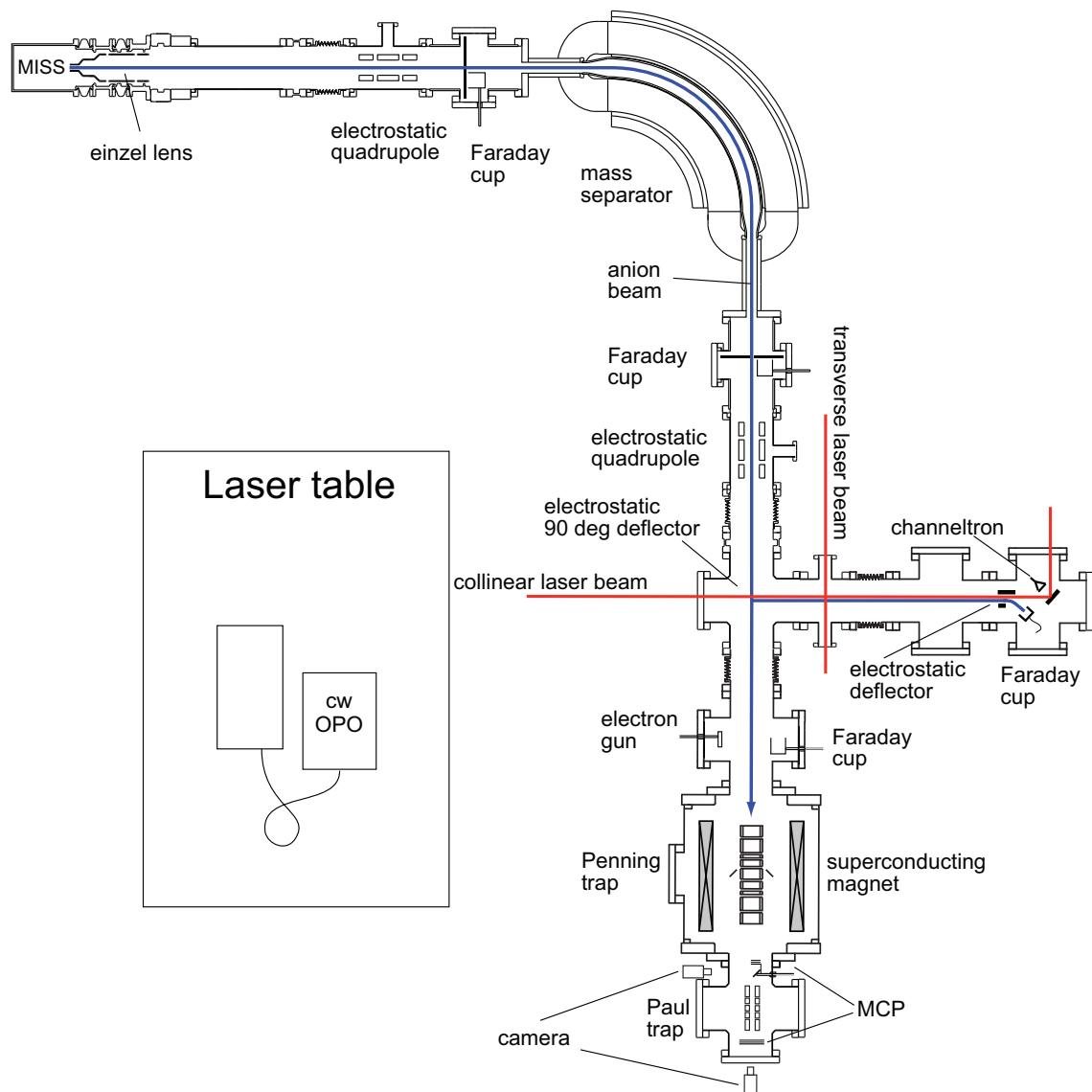
MISS

einzel lens

electrostatic
quadrupole

Faraday
cup

mass
separator

anion
beam

Faraday
cup

electrostatic
quadrupole

electrostatic
90 deg deflector

collinear laser beam

transverse laser beam

channeltron

electrostatic
deflector

Faraday
cup

Laser table

cw
OPO

electron
gun

Faraday
cup

Penning
trap

superconducting
magnet

camera

Paul
trap

MCP

Figure 1.1: Schematic drawing of the experiment.

1.2 Cesium sputter ion source

Negative ions can be formed from neutral atoms by electron capture in a dense electron cloud. In Penning traps, low energy electrons directed in the trapping region can be captured by neutral atoms or molecules [14]. Penning traps confine charged particles by superimposing static magnetic and electric fields. The magnetic field bends the trajectory in a spiral and the additional electric field prevents the ions from escaping along the magnetic field lines. The trap confines any particles of the same charge at the same time and, therefore, negative ions are compatible with the presence of electrons [31, 46]. This kind of production scheme relies on a three-body interaction. The electron affinity has to be removed from the system at recombination by a further electron which is expelled from the newly formed ion. The pressure of the neutral gas with contaminants, which may be present in the Penning cavity, can limit the lifetime of the ions due to possible further charge exchange. In some instances, the rest gas can perturb or modify of the ensamble under investigation, but in general the produced negative ions are already trapped and remain in a favorable environment for the study of their properties.

A second common way to produce negative ions is to attach an extra electron to a neutral atom via a charge exchange by a donor atom. This reaction has the advantage of being only a two-body interaction and thus a lower-order reaction. In this scheme, the binding energy of the electron from the donor is partially converted into electron affinity of the newly formed negative ion without the need of an additional partner collecting extra energy. Charge exchange sources are typically combined with extraction via a static electric field that accelerates the anions away from the charge exchange chamber. A beam of negative ions exiting the synthesis volume has some advantages over the volume production method. It is possible to transfer the newly formed ions to a more isolated environment with reduced quantities of residual gas, to load an accelerator or a storage ring, or to apply a purification process on the ion's path. In some instances, like in the case of La^-, several contaminants compete for negative ion formation (Fig. 1.7). The low electron affinity disfavors the production of La^- against its hydrides and oxides. It is therefore practical to adopt a charge exchange source, generate a negative ion beam and add a following mass selective element on the ion path to remove undesired secondary charged particles.

A widely adopted electron donor is cesium, which is present as a vapor in the charge exchange chamber to favor interactions with the material wanted as negative ions. Alkali elements, like Cs, have a weakly bound outer electron with the lowest ionization energy within each period of the elements in periodic table. In particular, Cs has the weakest bound, being the last stable alkali metal. A confined differentially pumped section containing Cs is therefore commonly used in charge exchange chambers. In some synthesis scheme a positive ion beam is produced and guided in a Cs vapor chamber where two electrons have to be transferred to generate negative ions [12]. Generated anions are collected at the exit along the propagation path of the incoming beam. The technique is adopted in connection with gas media where the positive ion production scheme adapts usually better.

A production design working on a similar charge exchange process has been described by Middleton [18]. This source type not only takes advantage of electron transfer but also uses positive Cs ions to sputter and ablate solid materials. The production chamber is filled with Cs vapor. An hot wire (*ionizer*) is heated to a temperature of about 1000 K by a current of $20\ldots30$ A. The neutral Cs atoms may lose an electron colliding with the ionizer surface. Then Cs^+ is accelerated by a suitable potential difference towards a solid target containing the element. The kinetic energy acquired by the positive Cs ions is generally enough to sputter material out of the specimen with a typical peak efficiency between tens and a few hundred keV [4]. In the sputtered material some negative ions may form. As described in Ref. [10] the sputtering process removes very high-temperature fragments from the target. In addition to the simple charge exchange some of this excess energy is disposed of by a three-body reaction process. The density of neighboring atoms is the highest near the target surface, indicating that region as the most likely formation place of the negative particles. Cesium coverage of the target plays a critical role in determining the final current of converted negative ions [1] which are accelerated back and extracted by

the same field used to guide Cs^+ onto the target.

The experiment at MPIK makes use of a Cs sputter source for anion production [55]. The source was developed, realized and maintained with the help of the vast know-how available at MPIK which was acquired operating tandem accelerators [5, 8, 24]. During the thesis, the source was partially upgraded to improve the yield at the challenging task of delivering La^-. As we will discuss later in this section the source works quite well for producing high-affinity materials. The binding energy of Os^- is about twice as that of the electron affinity of La^-.

For negative ion production, the target, the ionizer and the extraction potentials are set to increasing values so as to constitute an always accelerating static electric field for extracting negative ions. Higher yields of ions from the source is registered for higher potential differences, since both the sputtering process and the focusing acceleration effects favor the formation of more intense currents with small emittance. The source is operated with potential differences of a few kV instead of the optimal tens of kV, with a typical final energy of the beam in the range from 4 to 10 kV. The maximum operating voltage is limited by discharges in the high voltage connectors and the power supplies. The lower limit for the potential was set to obtain a current of La^- ions of a few pA in the experimental spectroscopy region as minimal acceptable working condition. The 4 kV minimal acceleration at La^- production was not only adopted to improve beam quality and current, but also necessary for mass purification. The resolving power of mass selection performed by a dipole magnet improves at higher kinetic energy, thus helping to separate the La^- from LaH^- and LaH_2^- contaminants.

In Fig. 1.4 we report a measurement of the anions produced with mass close to La^-. The peaks of La^- (at 139 amu), LaH^-, LaH_2^-, LaH_4^- and LaO^- (155 amu), LaO_2^- (171 amu) are highlighted. The first group composed by the hydrides constitutes the neighboring contaminants which are difficult to filter. They were possibly present in some fraction during experiments performed with La^-. The second group of the oxides shows a remarkable variation in mass intensity ratios after some days of operation. The oxides are naturally formed on the surface as the target is exposed to air when installing the vacuum chamber or exchanging the ionizer. During the sputtering operation, the surface is progressively ablated and therefore cleaned from these compounds. The difference in a few days is a relative change in the production yields of different compounds. The normalization over the La^- current highlights the detail in the picture (the La^- current was 1.2 pA at the beginning versus 0.25 pA in the end). The different noise level in the data stems from a different averaging procedure. In fact, in the beginning, the behavior of the source is changing rapidly, and the mass spectrum must be acquired in a short time. Conversely, thanks to the higher stability reached after a few days, ten times more measurements are averaged in the second curve. In the case of Au^- production, the source can be operated at much lower voltages down to a few hundred of volts in ion energy. This is attributed to the exceptionally favorable condition in which the source produces negative gold ions since gold has a high electron affinity and a high work function.

In the case of thermionic emission, the escaping electron must have an energy greater than the binding barrier constituted by the first ionization potential of Cs of 3.9 eV. As the collision of a Cs atom with the surface takes place, both partners may lose an electron, either the Cs or the surface. In the case of electron surface emission from a metal surface, the rate of process is governed by the Maxwell-Boltzmann distribution $f_{MB} = e^{-E/k_bT}$ in the high temperature approximation. The emitted current j follows the Richardson-Dushman equation:

$$j = A\,(1-r)\,T^2 e^{-\Phi_w/k_bT}\;,$$

where A is a constant and r accounts for the geometry of the surface. The energy Φ_w that appears in the exponential is the work function, i.e. the binding energy of electrons to the surface. The exponential dependence on the temperature is common to ionization of a single atom too, depending only on the Boltzmann distribution. The binding energy is in this case not the work function but the first ionization potential. From the formula we can deduce that the current rises exponentially as the temperature T of the ionizer increases. The power dissipated by the wire resistance favors surface ionization and also increases
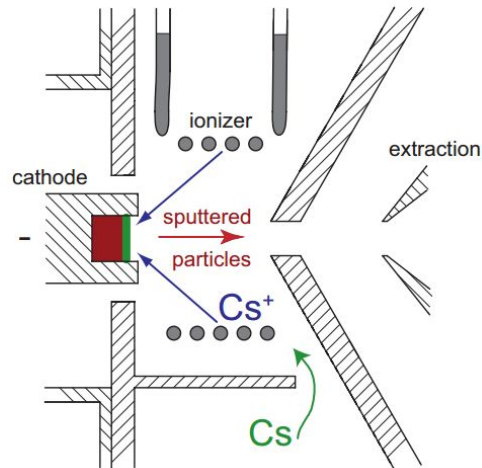
Figure 1.2: Schematic drawing of a Middleton-type negative ion source. Cesium vapor diffuses into the production region where the contact with the hot surface of the ionizer may remove the outer electron. Positive Cs ions are hence accelerated towards the target ablating some material. In the same field used to accelerate positive particle onto the target, the newly formed anions are accelerated outward exiting the trapping region as a beam. Adapted from [55].

Figure 1.3: One of the first experimental attempts to modify the ionizer material. Platinum thin foils were wrapped around the surface of a W ionizer.

the vapor release from the Cs reservoir that is thermally connected to the production chamber. Ionizer materials with higher work function favor electron loss from Cs instead of the surface. The equation also clarifies why high electron affinity and hence work function materials are produced better. As Middleton already observed, Cs^+ current is between 1 and 1.5 mA but the cathode current (the current supplied by the cathode power supply) is usually between 2 and 5 mA. The latter is larger because it includes the electrons emitted by the cathode, that mainly remain in the source. The magnitude of the electron current depends on the cathode material, where low work function materials produce more electrons. There is a correlation between work function and electron affinity, and therefore by producing low-electron-affinity negative ions more free electrons are generated. The achievable current density is however limited and in the source this results in a lower yield of negative atoms or molecules with low electron affinity materials. To give a quantitative example, we can compare the performance of the source in producing La^- ($\approx$ 560 meV electron affinity) against Au^- (2.3 eV electron affinity). We obtained a La^- current of about $10\ldots20$ pA with 7 kV acceleration and $3\ldots4$ kV sputtering voltage of Cs with 30 A ionizer current. Conversely, we observed a few nA of Au^- current with 1 kV acceleration and 0.5 kV sputtering voltage of Cs with 20 A ionizer current.

A relevant fraction of the target material is expected to leave the target surface due to the sputtering process. The cylindrical geometry of the ionizer favors a general directional acceleration towards the extraction point located on the axis facing the target on the opposite side of the ionizer. However, during operation, only a part of the produced negative ions make their way out of the chamber. A large amount of them remains in the source following the path already traveled by the positive Cs and landing back on the ionizer surface. After some hours of operation, the surface work function of the ionizer starts changing, approaching the value of the contaminating materials. For most of the sputtered materials, this does not constitute a real problem. If the overall work function remains greater than the ionization energy of Cs, the ionization process will continue. For other materials, including La, the opposite is true, and the yield of the source degrades over time. As the surface of the ionizer is covered by low-work-function contaminants, the probability for Cs to lose an electron progressively decreases. The process is referred to in the literature as *poisoning*. The reduced ionization rate results in a reduced sputtering rate and a reduced yield. The source, in the long run, switches itself off as operation goes on.

During operation, the source and the beamline have to be adjusted frequently. The general trend of the current is decreasing as consequence of the ionizer poisoning. Typically, after 2-3 days, a severe degradation of the system is observed. A short-circuit appears between the target and the ionizer and no more anions exit from the source. It is a clear indication that poisoning happened, preventing further operation. In this situation, the reduced sputtering rate can no longer be compensated by the quantity of incoming Cs vapor because the ionizer surface has become less active. The increased Cs quantity favors the formation of the short generating a direct discharge inside the chamber between the target and the ionizer, thus stopping Cs^+ formation and acceleration. In some cases, like presented in Fig. 1.5, a few more acquisition hours can be gained by reducing the temperature in the Cs oven. The diminished partial pressure of Cs may often restore good conditions for the sputtering to continue for some additional hours.

Several target materials were tested to produce La^-: LaO powder, LaB_6 and the pure metal. The latter was finally preferred for the higher yield. In all other cases, the additional components act just as additional sputtered contaminants, reducing the already low La^- current yield. With those targets, no improvement was registered in prolonging the operation time. Despite the suggestion in [43], where a recessed target was adopted, a protruding La target was preferred. This modification was selected to suppress the formation of anions other than pure La^-. By this configuration, higher quality and current of the beam was registered which was also determinant to obtain longer observation time.

Concerning the operation time, a different ionizer material proved to be important. Platinum and iridium are the metals with highest work function, and pure element wires were tested as replacements of the tungsten ionizer. While this modification, from the one hand, did not prevent poisoning from happening, it allowed extending the operation time of the source. In fact, the adoption of Pt or Ir ionizer
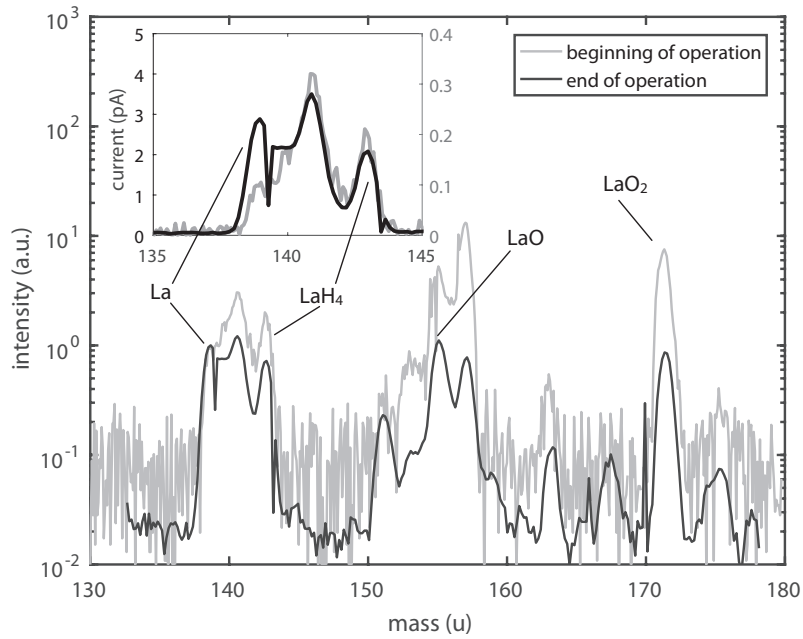
Figure 1.4: Mass spectra registered with a metallic La target. The curve *beginning of operation* was measured a few minutes after sputtering was started and the data at named *end of operation* after 2 days of continuous sputtering. The different noise levels have to be attributed to different data acquisition statistics. In the main figure the spectra normalized to the La peak to appreciate the ratio in the contaminants. Inset: The close view of the mass region of La in linear scale. The left scale refers to *beginning of operation* and right scale to *end of operation*.
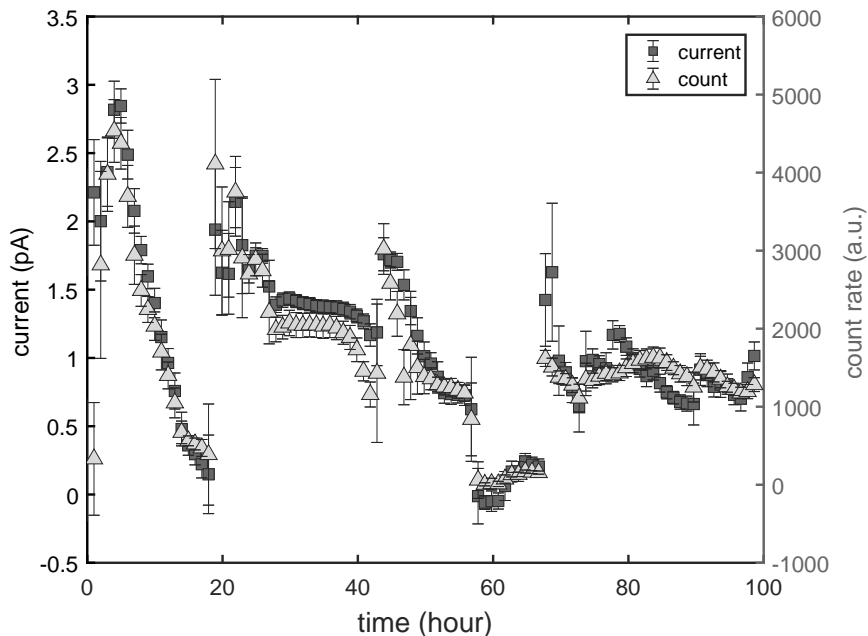

Figure 1.5: Measured current of La^- on the last Faraday cup (squares, left scale) and count neutral rate induced by the laser (triangles, right scale). The degradation behavior in the source caused by the ionizer poisoning is visible between hours 57 and 68 as a short-circuit. The neutral count rate is the corresponding neutral production rate of photodetached atoms by the laser (see Ch. 2)

14

kept the La⁻ current at the end of the beamline at an acceptable level (1 . . . 10 pA). The experiment time was thus extended to a few days against only 4 hours registered with the W wire of the original design.

The result was an overall higher negative-ion current exiting from the source due to more favorable condition for Cs ionization. An increase or decrease of the poisoning rate was not systematically investigated and the extended operation time was attributed mainly to the bare performance improvements. A higher Cs⁺ current produces a higher sputtering rate and consequently more La⁻ ions. A faster La sputtering speeds up the ionizer contamination. By contrast, much more La must be deposited on the surface to significantly lower the work functions of Pt or Ir wires. It is possible that these two counteracting effects balanced each other, up to a certain extent, hiding modification in the poisoning rate.

Several restoring procedures were studied to clean the ionizer surface after contamination. The material cost of the ionizer and the long bending process of the wire are among the reasons for investigating methods that allow resuming the work function properties. The replacement restores the yield to full performance while avoiding the time-consuming operation of breaking the vacuum twice to switch the targets. Removal of the contaminants from the wire surface can be performed by sandblasting or by treatment with acid. The latter solution was finally adopted. During the first experiments, the ionizer was boiled in *acqua regia*, but an ultrasonic bath of a few minutes in 37% concentrated HCl proved to be sufficient. The exposure of the wire to air does not affect the cleaning, and the ionizers can be cleaned any time after the exchange. Besides, after oxidation, La becomes a powder that easily separates from the ionizer surface.

Due to the intrinsic difficulties in the source handling, La was not the only ion used in this work. Gold was extensively employed in experiments to test the apparatus when the interaction with light was not required. Gold is a heavy element which has only one stable isotope: ^{197}Au. The mass value makes it similar to both Os and La regarding the motion induced by electric and magnetic fields. Exceptionally easy to produce by the same source, it features an electron affinity of 2.3 eV corresponding to a photon energy of green light. In contrast to Os and La, Au is chemically stable in air and constitutes no safety hazard. Therefore no particular precaution was needed in handling the specimen and the vacuum chamber.

The idea to combine two functions of sputtering and charge exchange by using Cs allows the realization of compact and powerful negative ion sources. However, this scheme is severely limited at producing negative ions of lathanides like La⁻. The poisoning effect of the ionizer is ultimately of detrimental impact for a long time operation of the Cs source. In the future, a viable solution may be represented by the division of the two functions, to be realized by different means. Creation of particles as positive ion may remove the sputtering role to the Cs, which would be used for the charge exchange reaction only. Alternatively, the adoption of laser desorption production has shown promising results as an alternative solution to the source design concept [71].

1.3   Mass selection

Many species of negative ions are produced by the Cs source as the sputtering process occurs. Especially when generating La$^-$ ions many other competing contaminants are present in the extracted beam since the capture process of the electron by La is highly suppressed. The La$^-$ ion current is not the strongest even in the case the target material is made of the pure metallic element only. To filter out unwanted species, a magnetic mass filter is installed in the beamline. Mass selection is provided by a dipole magnet which deflects the beam by 90 degrees. The magnet radius is $R = 0.5$ m.

Mass spectra of the components may be acquired by recording the amount of current transmitted as a function of the current flowing in the coils of the dipole magnet. In a previous work with the same source [75], a preliminary study of La$^-$ production and selection was performed. Unfortunately, the reported results could not be reproduced during the course of this work. Using a similar preparation for the source and the same calibration scheme, the mass peaks initially identified as LaC$^-$ and LaC$_2^-$ were later found to be usually LaO$^-$ and LaO$_2^-$, leading to a misinterpretation of the acquired values. In Ref. [75] a strong variability in the mass components depending on the sputtering parameters was also observed and in Fig. 1.4 it is shown how surface contamination may induce uncontrolled fluctuations among mass intensity ratios. The former method, relying on the identification of anions based on relative current strength, was then considered unreliable. Thus, a more robust understanding of the variation of the magnetic field as a function of the coil current was preferred.

An ion of mass m and charge q traveling into the magnet region perceives a centripetal force f induced by a homogeneous magnetic field with magnitude B which is proportional to its speed v:

$$f = m\frac{v^2}{R} = qvB \ .$$

As a consequence of the production process, all ions acquire a kinetic energy $W = \frac{1}{2}mv^2 = qV$ due to the common acceleration by the extraction voltage V. Thus

$$W = \frac{1}{2}\frac{q}{m}R^2B^2$$

Typically, the magnetic field is proportional to the current I flowing through the magnet coils. It is possible to approximate the dependency of the magnetic field on the current as a second order polynomial. A least-squares linear problem models the system by the following equation:

$$\sqrt{Wm} = a_0 + a_1I + a_2I^2 \ ,$$

, where the unknown variables are $\sqrt{m}$ and the a_i coefficients. The polynomial on the right-hand side is a approximate expression of the magnetic field B. The main term is expected to be linear proportional to a_1. The coefficient a_0 accounts for the residual magnetization, and a_2 describes further hysteresis effects at high current.

The procedure followed to obtain these variables started by acquiring several mass spectra at different anion kinetic energy. No mass component was identified at first to prepare the fitting problem. In each mass spectrum, the same masses appear for a different current value. Around that current a transmitted intensity peak as a function of the current is visible. Each peak can, therefore, be recognized by three values: the mass (unknown), the acceleration energy and the current in the coils.

Without direct identification of any particular particle species, the analysis had to rely on the general appearance of the detected signal. Due to the relative positions and shapes, it was possible to recognize several similar structures in each spectrum. The same mass component was associated with similar peaks taken with different accelerating voltages. Several data points are therefore available for each mass since they appear at different current depending on the extraction energy, thus reducing the linear least squares problem into a solvable vector space. After the fit only one mass species had to be identified to calibrate the absolute scale. Lanthanum was found at the expected value of 139 u by assuming unitary negative charge for each peak.
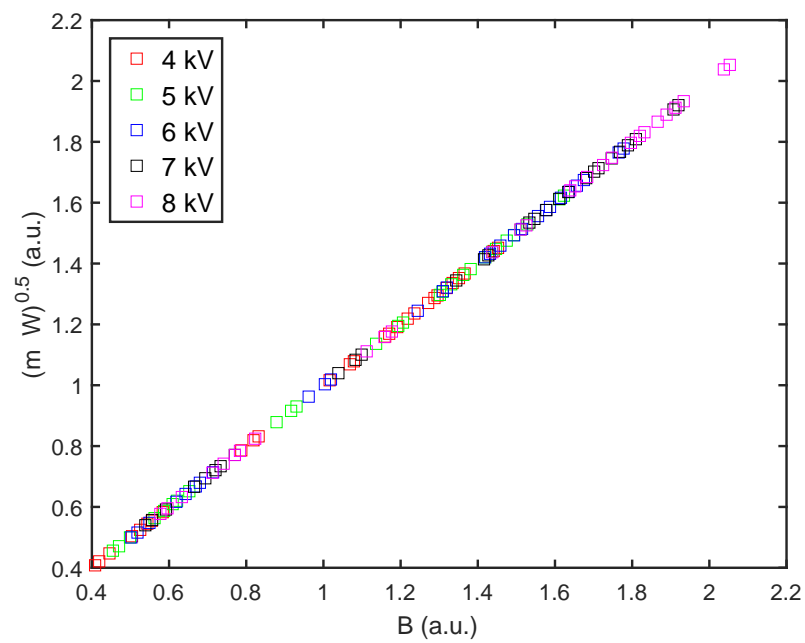
Figure 1.6: Test curve for mass calibration method described in the text. Each point corresponds to one mass peak in one particular acquisition. After performing the magnetic field to current fit all points align on the same straight line proving the validity of the analysis. Each data point corresponds to a measurement of Fig. 1.7
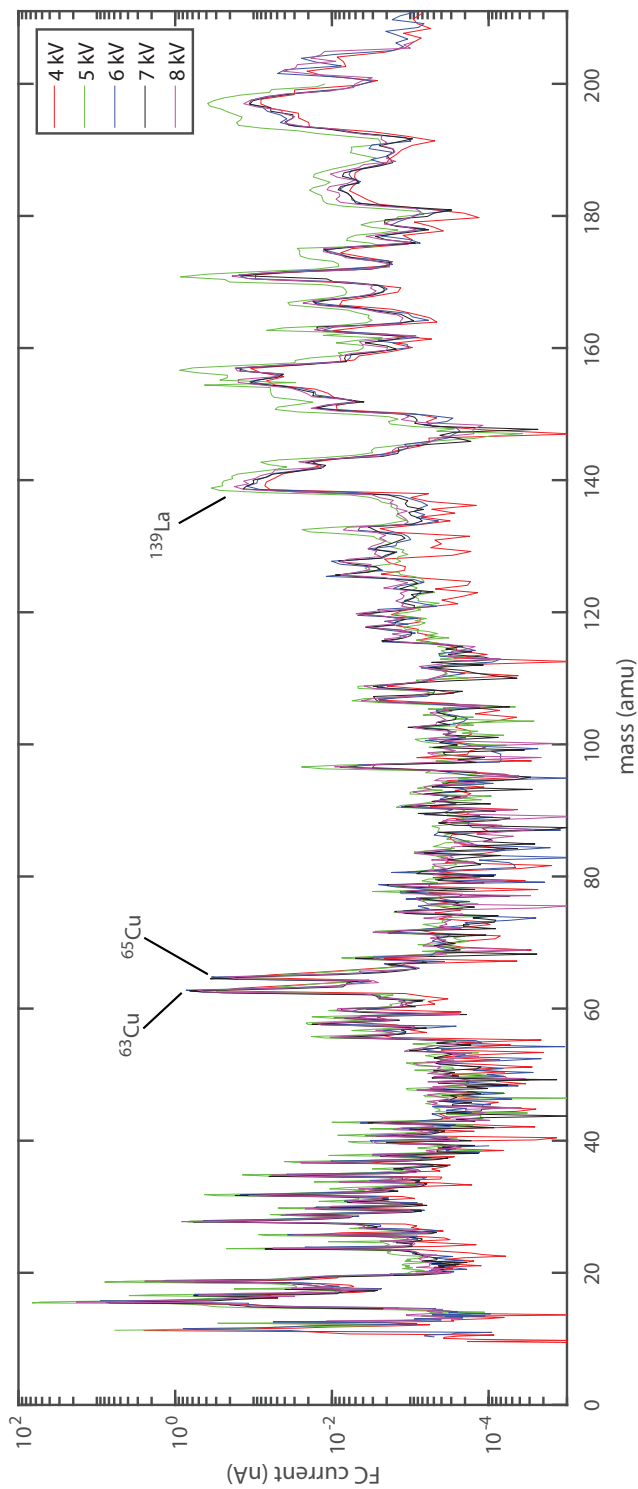
Figure 1.7: Mass spectra registered at different extraction energies. The spectra were analyzed as described in the text. The peak of ^{65}Cu was used reference mass for calibration of the absolute scale. The peak corresponding to La$^-$ is just one of the many anions produced. Mass selection is therefore fundamental to purifying the composition of the beam.

18

1.4 Control system for trapping experiments

The trapping experiments required several procedures which can modify experimental configurations and procedures and find the best working conditions. A control system was thus realized to operate automatically, under software control, both configurations and measurements. This preparatory work allowed acquiring a large number of measurements and making intensive use of the system both during data taking and data analysis.

The control system of the experiment was developed such as to separate high-level operations and precise timing control. The high-level operations were implemented using Labview2010 and C++ on two personal computers. They included the initialization of controllers, the sequential setup of instruments, power supplies, wave function generators and data transfer from the measuring instruments. The flow control of the execution that gave precise timing and triggers to the hardware was realized by a dedicated logic card (SpinCore Technologies PulseBlasterESR-PRO). A compiler for the card was written in C++ during this work to convert statements of a programming language into a sequence of logic output[1]. The compiler includes variable definitions, functions, recursion and simple math operations, however it is missing floating point operations and selection constructs. The programmable statements in the compiler are translated to logic waveform on a 24-bit registry mapped to the 24 TTL outputs of the card. The compiler translates the code into output state changes that are executed with defined timings from the program start. The time base is controlled by the onboard clock (100 MHz) of the logic card.

The general flowchart of an experimental sequence is presented in Fig. 1.8. In the beginning, the computer acts as master and starts by initializing the system. Then the execution script is compiled and sent to the card and the computer goes into slave mode, waiting for instructions from the pulse card. After the pulse sequence is transferred to the PulseBlaster card the execution of the program is started. At this moment, the computer enters slave mode, and the card takes control of the system, giving the precise execution triggers to the hardware. Part of the output of the card is dedicated to communicating commands back to the computer to follow execution steps. The commands addressed to the computer by the logic card are encoded on the last output bits of the interface register and sent to an acquisition card mounted in the computer. At the end of each measurement sequence, the pulse card sends a command to the computer to exit slave mode; then the Labview program takes care of downloading data from the instruments and recording the acquisition in a dedicated folder.

Further to the timing script a second tabular text file was used to define the states of the power supplies and other hardware and was used by the Labview program in slave mode to completely define the specific instrument settings. For instance, the values of the voltage configuration on the power supplies can be selected from different lines of the tabular file depending on the command given to the computer by the pulse card. A third and last file associates the two text files (script and tabular) for execution.

The general advantage of this approach is a great flexibility in deciding rapid changes in the behavior of the experiment from one acquisition to the next, and to implement time sorting of the instruction at compile time. The rapid changes are implemented by modifying the execution scripts that are simple text files. Several scripts have often been batched to scan experimental parameters such as the storage time of the particles. Moreover, the scripts can easily be saved in the acquisition folder to record the execution modalities for each measurement.

The sorting of the instructions in time simplifies the handling of the parallel workflow of different devices during procedure execution. A typical example is the acquisition of an image from the MCP detector. In this case, the following events must happen in sequence:

1. the computer starts the camera program waiting for an image,

2. the MCP voltage is turned on,

3. a trigger pulse is sent to the camera,

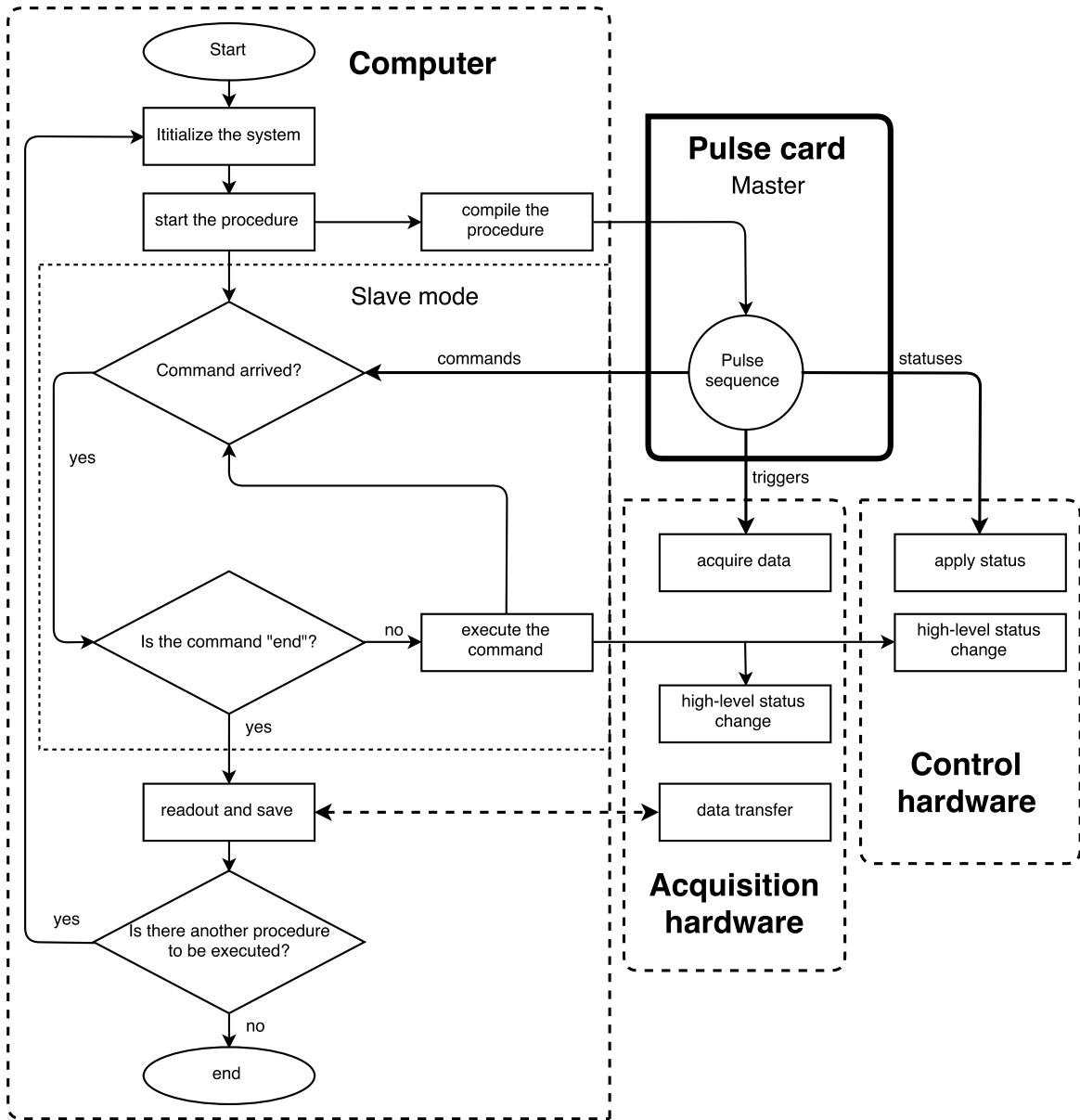[1] The compiler manual is in appendix Sec. A.1

Figure 1.8: Flow chart of the execution of experimental procedures.

4. the MCP voltage is turned off.

This type of sequence is handled by sending three different commands to the computer at different times: 1, 2, and 4; while one of the output channels of the pulse card is connected directly to the camera to perform 3. The computer commands can request a certain amount of time to be executed and a function can be written such that at a definite time t after the beginning of the sequence the snapshot will be acquired, taking into account the timing constraints.

However, the operation of acquiring a picture is tiedied to an event in the experiment, like releasing trapped particles by switching the final end cap. The switch is controlled through another output of the pulse card and during the execution a new instruction

5. switch the endcap

must be introduced between 3 and 4. The time sorting of the instructions relieves the programmer from actively coding the sequence. In fact, instructions 1-4 are written into a function and the time sorting inserts instruction 5 between 3 and 4 automatically. In this way, the programmer only has to request the picture to be taken at a defined time without entering into all details of the experimental requirements[2].

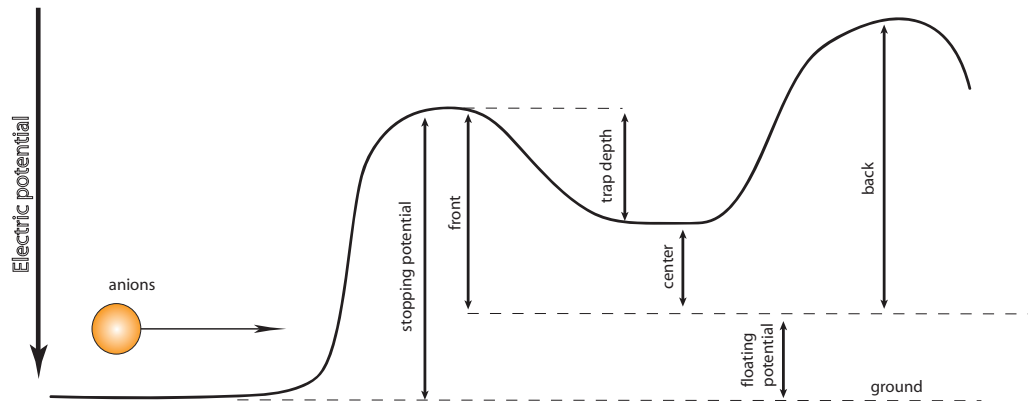[2]see appendix Sec. A.1 for code example

Figure 1.9: Schematic of the trapping DC voltage designation for axial confinement.

1.5 Trap potential well

During this thesis work, a Penning trap and a linear Paul trap have been used. Both traps provide radial confinement and axial confinement in a cylindrical geometry. In the Penning trap, the radial confinement is obtained by a magnetic field, while in the Paul trap it is due to a quadrupole radiofrequency field. Axial confinement in both traps is realized by an electric potential well generated applying three voltages on three neighboring electrodes. Voltages are applied to the first and the last end caps with respect to the central one to push ions towards the center.

All power supplies are mounted on a high-voltage platform (max. 5 kV) and have a common floating potential with respect to ground. Using these power supplies, front, center and back electrodes of the traps can be set to three potentials which define the electric potential well of the trap. By modifying the floating potential the full trap can be raised or lowered with respect to ground without affecting the internal electric configuration of the well. To be clear in what follows it is useful to give some names to the absolute potential (to ground) and relative potential (to the floating potential) that will be used in the description of the experimental setup:

- *ground*/*enviroment* is the potential of the external vacuum chamber and the reference for the entire experiment.

- *front* potential is the potential applied to the front end cap measured with respect to the floating potential.

- *center* potential is the potential applied to the central electrode of the trap, measured relative to the floating potential.

- *back* potential is the potential applied to the last end cap, measured with respect to the floating potential.

- *floating potential* or *trap reference* is the bias voltage applied to the high-voltage platform and is used as reference for all internal power supplies

- *stopping* or *decelerating potential* = *front* + *floating potential* is the voltage applied to the front end cap, measured with respect to ground

- *storage potential* = *center* + *floating potentials* is the potential at which the particles are trapped with respect to ground.

22

- *depth = center − front* potential is the difference between the central and front electrode typically defines the depth of the trapping well.

This setup allows changing the potential energy of the stored ions without affecting the properties of the trapped sample. This can be used to adapt the stopping voltage for the anion beam and favor the loading operation of the trap. After capture, the reference potential can be varied at will while preserving the internal properties of the system. Even though it is possible to set the reference (floating potential) equal to ground, this was in practice never realized, and a minimum potential of a few hundreds of volts was always kept to give anions a sufficient momentum when ejecting towards the MCPs mounted up- and downstream from the trap on axis. The corresponding kinetic energy favors the secondary-electron emission in the channels for detection of the trap content.

1.6   Penning trap

The Penning trap of the UNIC experiment is composed of a superconducting solenoid and a stack of 13 coaxial cylindrical electrodes. The solenoid is used to generate the axial magnetic field responsible for the radial confinement of charged particles. The maximum field intensity in the central region of the magnet is 6 T and is tunable by varying the current flowing in the solenoid. The map of the magnetic field on axis is shown in Fig. 1.11. The cryogenic system drives the temperature of the coils below 5 K to ensure the superconductive state and lowers the electrodes temperature to about 30 K. The cylindrical electrodes have a diameter of 33 mm and the length is shaped to enhance the harmonicity of the confining electric potential along the axial direction as suggested in Ref. [16]. The central electrode is divided into four angular sectors to allow applying a *rotating wall* excitation so to add torque to the confined plasma [41]. The geometry of the electrodes is shown in Fig. 1.10.

At the beginning of this work, the mechanical parts of the Penning trap were already assembled, and during this thesis the system was revised as concerns the electronic hardware and the control system (see Sec. 1.4). The commissioning work of the electrical parts included power supplies, switches, detectors and a partial rewiring of the electrodes for high voltage (5 kV) compatibility.

The Penning trap is placed downstream of the electrostatic deflector after the spectroscopy section[3]. Ions exiting the mass separator travel on the axis of the trap. The center of the trap and the mass separator are 2.5 m apart. The trap was carefully aligned with respect to the beamline by using the central position of the external flanges and relying on the mechanical assembly for the alignment of the inner components. The trap axis is directed towards the mass-separating magnet with a precision of 1 mm and $1°$. A series of differential pumping stages, which separate the various sections of the experiment, allowed the preservation of a vacuum level of a few 10^{-11} mbar against a few 10^{-7} mbar measurable right after the Middleton source. The pumping sections are defined by vacuum constrictions along the experiment, the last one with a diameter of 7.5 mm separating the trap region from the spectroscopy part of the apparatus.

The trap was often operated with several electrodes connected together. The shorting of some electrodes allowed the reduction of the number of high-voltage switches and power supplies needed to operate the trap. In all experiments, only three voltage levels were present at the same time: on the central region and on the two end caps. The central voltage must be higher than the end caps to obtain confinement of negatively charged particles. Approaching from the beamline the *front* potential was applied to electrodes 0, 1 and 2 shorted together (see Fig. 1.10). The next series of electrodes from 3 to 7 were interconnected to define the *central* region. The last end cap (*back*) potential was applied to electrodes 8, 9 and 10 to be symmetric to the front end cap. Each end cap was connected to a switch that could rapidly change the voltage between two predefined levels. Possible use of these switches was to open the trap on one side polarizing the corresponding side electrode to the same potential of the central electrode, thus leaving the ions to leave the trap from that side.

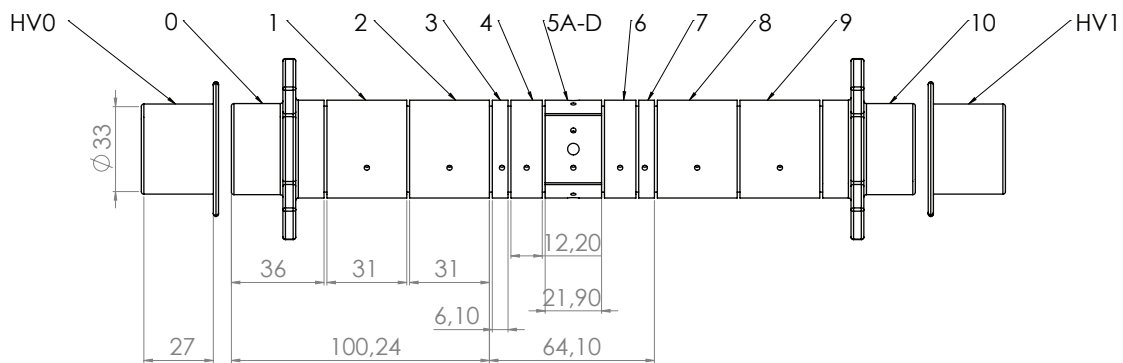[3]In Sec. 1.1 an overview of the experiment is given.

Figure 1.10: Schematic view of the electrodes of the Penning trap. Dimensions are in millimeters. The central electrode is split into four angular segments for rotating-wall excitation. Labels of the electrodes are indicated above.
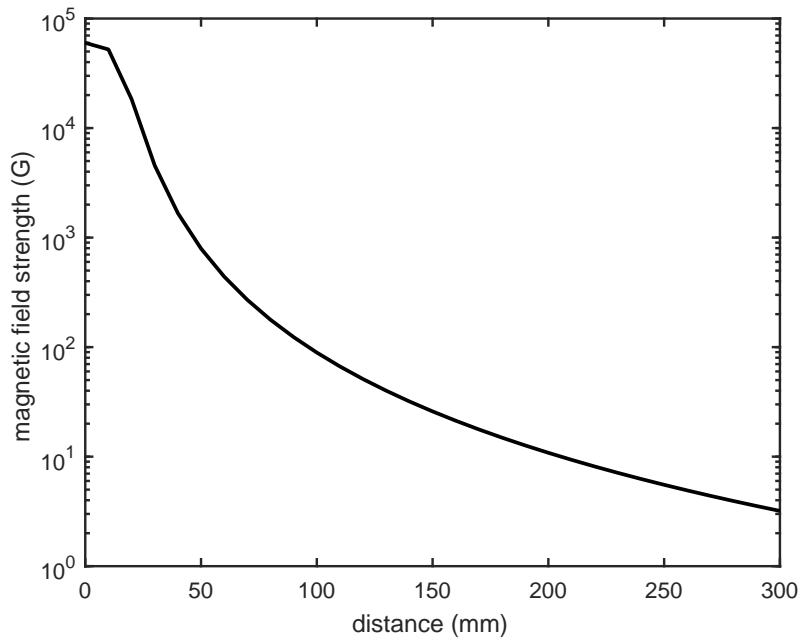

Figure 1.11: Axial magnetic field strength as a function of the distance from the center of the solenoid. The field is 6 T in the central region.

Electrons can be loaded into the trap by an electron gun situated upstream that can be inserted into the beamline by a pneumatic linear actuator. Three detectors were available during the measurements. The first is a movable Faraday cup near the electron gun and directed towards the incoming beam to measure the current of anions entering the trap region. The second is an MCP with a metal anode, oriented towards the trap and assembled on a pneumatic feedthrough next to the electron gun and the Faraday cup. The third detector is a further MCP, with a phosphor screen, mounted downstream along the beam line at 280 mm from the trap center[4]. Charged particles exiting the trapping region and traveling towards the detector tend to follow the magnetic field lines. The motion of a charged particle exiting the field has as adiabatic invariant Ba^2, where B is the magnetic field and a the cyclotron radius [35]. At the distance of the MCP, the field reduces by va factor 8 compared to the value in the center. Thus the acquired data have been scaled accordingly by $\sqrt{8}$ in order to analyze plasma dimensions and particle densities.

All trapping techniques were established with Au^- ions because of the favorable production in the ion source. In particular, the high electron affinity allows operating the source at remarkably low voltages (down to 400 V accelerating potential) still providing a sufficient amount of current (> 100 pA). At the same time, the ionizer was not poisoned, and the source could be kept running with a standard tungsten ionizer for months without maintenance.

---

[4]This MCP was later removed to insert the Paul trap in the apparatus

1.7 Paul trap

During this work, a linear Paul trap was developed to perform experiments with trapped anions in the absence of a magnetic field. The trap is mounted in the main apparatus downstream of the Penning trap (see Sec. 1.1 for a general overview of the setup)[5]. The main differences of our design in contrast with the others are twofold. The first one is the geometry of fast switching electrodes that allow axial optical access and can be operated at relatively low voltage. The second is the possibility of floating the electrodes to match the keV beam energy of negative ions from a Middleton source and mass selection.

An ideal linear Paul trap produces a quadrupole alternating electric field. Such a field can be generated by two pairs of opposing hyperbolic electrodes rotated $\pi/2$ one with respect to the other. A radiofrequency of amplitude $V_0/2$ and angular frequency Ω is applied to the electrodes. Two opposite electrodes oscillate with the same phase, while the other two oscillate with a phase shift of π. The system produces an electric potential in the radial (x, y) plane with the following expression:

$$\Phi = \frac{V_0}{2} \frac{x^2 - y^2}{2R^2} \cos(\Omega_{RF} t) \quad .$$

To simplify the machining of the electrodes as well as to gain optical access, it is common practice to realize the electrodes as cylindrical linear rods and to place them with their axes at the four corners of a square. The cylindrical, and not hyperbolic, geometry of the rods leads to a field deformation that can be modeled with the expansion series

$$\Phi = V_2 \left(x^2 - y^2 \right) + V_4 \left(x^4 - y^4 \right) + \dots \quad ,$$

where V_2 and V_4 are constants. The expression corresponds to a 4th order multipole expansion where the chosen symmetry allows only even powers. Suppression of the V_4 term can be obtained by carefully adjusting the distance of the cylindrical rods. The necessary distance can be obtained by equating the derivatives of the equipotential lines of Φ to the derivative of the electrode surface expression. Two rods will be placed on the x axis and two on the y axis. The distance of each rod from the center will be designated as d, and the rod radius R. The electrode surface geometry whose axis is in $(x, y) = (0, R + d)$ is then described by the function

$$y(x) = d + R - \sqrt{R^2 - x^2} \quad .$$

The equipotential surface at the electrode $(x, y) = (0, d)$ including only 4th-order terms is given by

$$y(x) = \sqrt{\frac{1}{2} \left(\frac{V_2}{V_4} + \frac{1}{V_4} \sqrt{V_2^2 + 4\Phi V_4 + 4V_2 V_4 x^2 + 4V_4^2 x^4} \right)}$$

Equating the series expansion of these two functions at $x = 0$ we can find the condition to suppress the 4th-order term of the Taylor expansion. The solutions of this equation system is

$$\frac{V_2}{\Phi} = \frac{2}{d(d + R)} \qquad \frac{V_4}{\Phi} = \frac{1}{d^4} \left(\frac{R - d}{R + d} \right) \quad .$$

The 4th-order term is thus suppressed if the distance between to opposite rods is equal to the diameter of the rods. The cylindrical rods were hence designed to be close to this geometry. The diameter of each rod is of 14.8 mm and each of them is fixed at the corners of a square of side equal to 28.8 mm. The radiofrequency is applied to the rods with frequency $\Omega_{RF}/2\pi = 1.93$ MHz and a typical peak-to-peak amplitude of $V_{pp} = 630$ V.

The rods have been segmented to apply a DC voltage to different sections to provide axial confinement. Each rod is composed of a stack of 5 cylindrical stainless steel electrodes with lengths 44.5 mm,

---

[5]Detailed description of linear Paul traps and how to operate them may be widely found in the literature [79], [77].

14.5 mm, 14.5 mm, 14.5 mm, 46.5 mm, respectively. Both ends of each electrode are shaped to accommodate a cylindrical ceramic insulator of 12 mm diameter and a length of 8.5 mm. The insulators align the axis of neighboring electrodes and provide an inter-electrode distance of 0.5 mm for electric isolation. The stack of electrodes and insulators is held together by a long screw passing through a borehole between two metal plates. The plates are electrically grounded and shorted together by the long screws. The first plate is 1 mm thick and has a ring shape with diameters 50 mm and 15 mm. The last plate is also a ring with a larger external diameter (150 mm) and thickness (6 mm). This last ring supports the entire trap. The Paul trap is designed for a standard 6-way CF160 cross. From a CF160 flange, three M6 threaded rods are used to adjust the position of the trap inside the cross, by modifying the mounting position of the ring plate. The mutual positioning of the rods is achieved by two insulators that firmly attach at the center of the first and last electrode of the stack (the long ones of 44.5 mm and 46.5 mm). Each electrode has two threaded holes located on the side facing away from the trapping region which allow an electrical connection as well as pumping the otherwise dead volume inside the hollow cylindrical stacks.

After the design and manufacturing, the Paul trap was upgraded with two fast switching electrodes to be used as end caps. The electrodes were realized as part of the work [95]. The reason for introducing new electrodes disconnected from the rods resides in their electrical properties. The electric potential of the rod segments cannot be switched quickly, thus slowing any trap potential reconfiguration. This limitation is due to the coupling circuit for the radio frequency and DC potentials which damps voltage oscillations towards the DC input with a low-pass filter. This low-pass filter also affects DC switching which should occur faster than the timescale of anion motion which corresponds to risetimes less than a few μs. The geometry of the electrodes is shown in Fig. 1.13. The two lobes facing each other enter the trapping region, avoiding any contact between electrode and rods. It was calculated and confirmed by measurement that the potential on axis is 0.18 times the applied voltage. The linear geometry leaves space in the orthogonal direction to axially introduce a laser beam axially into the trap at an angle up to a few degrees.

The geometry of these two lobes introduces an asymmetric force in x and y directions while providing confinement along the axis z. For the following considerations we will now assume the geometry to be rotated by 45° so that the lobes are aligned along the y axis. The potential near the trap axis, in the adiabatic approximation and disregarding orders higher than the second is

$$\phi = \frac{x^2}{\alpha_x^2(z)} + \frac{y^2}{\alpha_y^2(z)} \tag{1.1}$$

$$\alpha_x^{-2}(z) = -\frac{1}{2}m\omega_r^2 + \frac{qU_0}{a_x^2(z)} \tag{1.2}$$

$$\alpha_y^{-2}(z) = -\frac{1}{2}m\omega_r^2 + \frac{qU_0}{a_y^2(z)} \quad , \tag{1.3}$$

where U_0 is the potential applied to the end caps and m the mass of the ions. ω_r is the angular frequency of the macromotion induced by the radiofrequency in the absence of axial confinement. ω_r is a function of the rods, diagonal half distance r_0, the mass m and charge Q of the ion, as well as the parameters of the radio frequency field:

$$\omega_r = \frac{QV_{pp}}{mr_0^2\Omega_{RF}\sqrt{2}} \quad .$$

To estimate asymmetric effects of the two lobes the eccentricity $\epsilon = \sqrt{1 \pm a^2/b^2}$ as a function of the position was calculated. The parameters a and b correspond to the semi-major and semi-minor axis of an equipotential line approximated by fitting the potential near the axial region with a quadratic function. The equipotential lines give, in fact, a hint of the shape of the ion cloud once the energy of the trapped sample is fixed. The sign in the eccentricity formula is to be used positive in case the
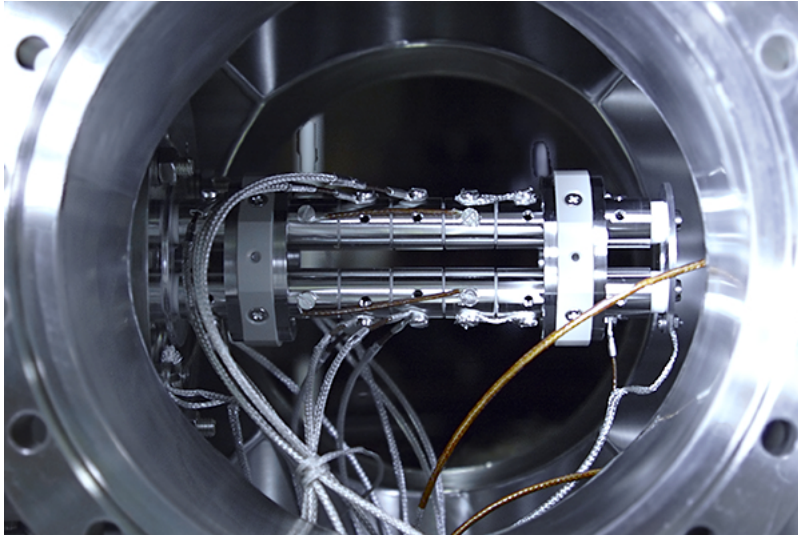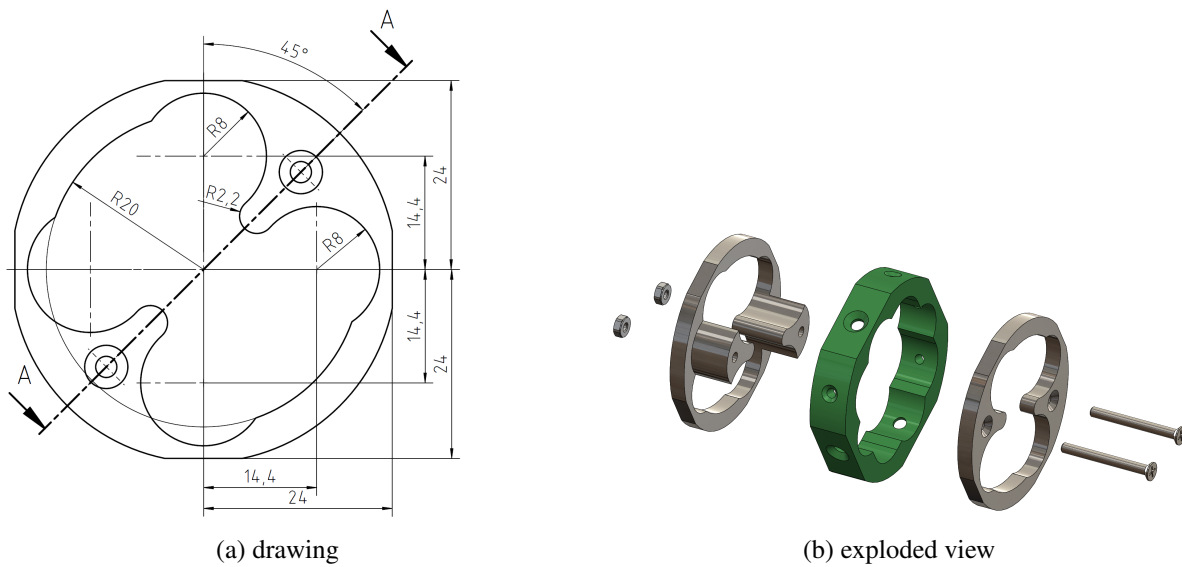
Figure 1.12: Photograph of the Paul trap mounted in the vacuum chamber.

(a) drawing

(b) exploded view

Figure 1.13: Transverse cut and exploded view of one DC fast switching electrode. It is mounted on the plastic insulator depicted in green that defines mutual distances and parallelism relative to the cylindrical rods. The length of the assembled electrode is 18 mm.
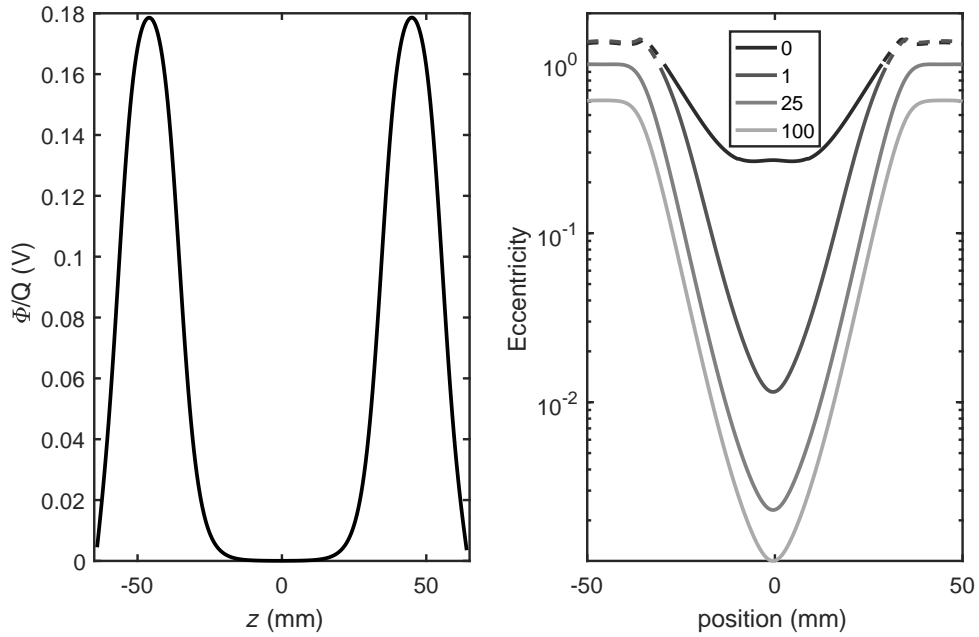
Figure 1.14: Right pane: Axial electric potential if 1 V is applied to the DC electrodes and 0 V on the rods. Adapted from [95]. Left Pane: Eccentricity of the equipotential lines as a function of the position along the z axis in the trap center. The asymmetry of the lobes causes an asymmetry of the equipotential lines in the transverse plane. The solid lines correspond to confining potentials in both directions and the dashed lines to confinement in only one direction. The eccentricity formula was used with parabolic or hyperbolic convention as reported in the text. The different curves correspond to different ratios between the RF amplitude and the DC voltage on the switching electrodes as specified in the legend.

potential is deconfining in both x and y direction, but negative in case confinement in y direction is present. Notwithstanding the asymmetry introduced by the lobes, it must be noted that the confining RF term strongly suppresses this asymmetry (Fig. 1.14), and the potential was considered approximately symmetric in the field configuration used during the experiments.

	pair	anti pair
Length (mm)	10	5
Inner diameter (mm)	80	80
Outer diameter (mm)	90	90
mean position (mm)	15.7	44.9
H ring 1 (kA/m)	-287	-419
H ring 2 (kA/m)	-288	-439

Table 1.1: correction magnets. Position refers to distances from the middle of the Paul trap

1.8 Magnetic-field-free laser interaction

The double trap setup of the UNIC experiment can use the Penning trap to catch and cool ions, which are then transferred to the Paul trap. Working with both traps simultaneously opens the challenge of removing the magnetic field in the trapping region of the radiofrequency trap where the laser cooling will take place. The scheme allows stopping La$^-$ ions by using electron cooling, as described in Sec. 3.3, thus improving the catching efficiency of anions by several orders of magnitude. Shielding the magnetic field requires a passive medium that could flexibly compensate the magnetic field generated by the superconductor. A typical solution of this kind adopts a second superconducting coil because superconductors freeze the magnetic field flux inside of them when the transition to the superconducting phase takes place. This effect allows freezing fluxes of any allowed values, even zero. Alternatively, the coil of the superconducting magnet of the Penning trap can be switched on and off, resulting in a so-called *combined trap* [23, 34]. A combined trap is a mixed trap where both radiofrequency and magnetic fields are used to provide confinement. The process of tuning the current of the superconductor on and off in the UNIC setup can take several minutes, but the ions could already start the laser cooling at the low temperature reached by electron cooling (see Sec. 3.4).

Alternatively, the magnetic field may be compensated by additional magnets. Compensation, like shielding, may increase the repetition rate of the experiments because both traps can be operated at the same time. A small part of this thesis was devoted to the design of a compensating system based on permanent magnets. The geometry of the magnets is reported in Tab. 1.1. A set of four compensation permanent ring magnets was designed to compensate the field at a distance of 802 mm from the Penning trap center. Two magnets compensate the strength of the field inside the Paul trap, while two others correct the residual gradient. The homogeneity region for the magnetic field would extend for about 10 mm length on the axis of the Paul trap with fluctuations below 1 G compensating a field of 100 G. However, the use of permanent magnets is subject to some technological challenges. In particular the drifts under external field and thermal instabilities may constitute limitations. We decided to use samarium cobalt magnets (Sm_2Co_{17}) to reduce the effect of the environment. Compared to more common magnets based on neodymium, samarium cobalt has a slightly lower residual magnetization ($10 \ldots 20\%$ less), but are characterized by higher stability of the field under external influences. Samarium cobalt magnet shows high demagnetization resistance, excellent anti-corrosion resistance and outstanding thermal stability ($3 \ldots 5$ times higher Curie temperature and corresponding higher stability to thermal drift compared to Nd magnets). However, the mechanical properties of samarium cobalt make the assembly challenging. The material is hard and brittle and therefore difficult to handle. Another disadvantage is that the compensating system requires an adjustment to the actual magnetic field present in the real apparatus. Accurate tuning of the current in the superconducting magnet is necessary to compensate the field inside the Paul trap. A direct measurement would allow taking into account the additional material ignored in the model and fine-tune the parameters of the real magnetic field generated by the superconductor. In the end this solution was not investigated further due to time limitations.

1.9 Laser wavelength generation

The laser radiation used during the spectroscopy experiment (Ch. 2) is generated by the commercial system Argos$^{\text{TM}}$ Model 2400 CW OPO (Module B) that can also be used for laser cooling. The system generates IR radiation around 3 μm wavelength from a pump wavelength of $\approx$1 μm thanks to an *Optical Parametric Oscillator* (OPO) in which the light is down-converted by a non-linear crystal into two lower-frequencies light beams. The light generation starts with a *Distributed-Feedback Laser* (DFB) producing IR radiation at 1064 nm. In DFB lasers the gain medium is corrugated as a waveguide to achieve a single-longitudinal operation with extremely narrow bandwidth (few tens of kHz) [49]. A piezoelectric element allows stretching the waveguide, thus tuning the frequency of the output radiation. The light (5 mW) generated by the DFB seeds a fiber amplifier that delivers up to 10 W of light into the down-converting crystal. The *periodically poled lithium niobate* (PPLN) non-linear crystal transforms the photon of the pump into two lower-energy photons called *signal* and *idler*. Signal is conventionally the name given to the radiation at the higher frequency. The crystal is enclosed in an optical cavity (the oscillator), which is designed to select single-mode operation at the signal wavelength. The idler wavelength is determined by energy conservation because the pump and the signal frequencies are fixed. The idler wavelength is adjusted around 3.1 μm for our experiments. The wavelength can be coarsely regulated by changing the properties of the crystal or the cavity, and fine-tuned by applying a voltage to the piezoelectric element in the DFB seed. The output power in the idler beam is up to 1.5 W at full amplifier power with a nominal bandwidth less than 1 MHz.

In section (4.1) we will specify the three transitions to address by the laser to achieve the laser cooling and make use of all La$^-$ ions from the ground state. These transitions are identified by peak numbers 1, 4 and 7 in the La$^-$ spectrum (see Fig. 2.7). Since the highest-frequency difference among the states is about 1.5 GHz, it was possible to generate all radiations by upgrading the existing laser used for spectroscopy by adding two resonant phase modulators. A modulator redistributes the light power from the central laser frequency into nearby sidebands. The sidebands appear equally spaced from the carrier with a frequency shift corresponding to the modulation frequency, and they have symmetric shapes from the carrier. Selecting the carrier as one of the three hyperfine transitions fixes the modulation frequencies to reach the remaining two. To obtain efficient cooling only red-detuned frequencies must interact with the three transitions at the same time. In order to achieve this condition, under the symmetry property of the imprinted modulation, it is natural to choose the frequency of peak 7 to be the carrier while generating the other two with modulations at 665 MHz and 1490 MHz.

We used *Electro-Optical Modulators* (EOMs) to generate the sidebands. In these modulators, the Pockels effect modifies the optical path of the propagating light. In certain crystals, the refractive index n along one crystallographic direction can be linearly modified by applying an electric field to the crystal. Thus, a modification of the optical path can be controlled over time by imprinting a phase shift in the light wave traveling the medium. We used lithium niobate (LiNbO$_3$) crystals with cross section 3×3 mm^2 and length $L = 40$ mm. The crystals respond at 3.1μm wavelength with a refractive index of about $n_0 = 2.1$, and a field of 10^6 V/m produces a fractional index change of roughly 0.01%. The electric field is applied along the longitudinal direction by two parallel plates. A phase modulation of sinusoidal shape is obtained by coupling the capacitive load of the crystal with an appropriate circuit resonant at the desired frequency.

If the electric field oscillates at angular frequency ω then the refractive index will oscillate as a function of time:

$$n(t) = n_0 + n_E \sin(\omega t) \quad ,$$

where n_0 is the refractive index without electric field applied, while n_E is the amplitude of the sinusoidal refractive index modulation. If the oscillation period is longer than the travel time of the light inside the crystal we can neglect the dynamic contribution from the finite extent of the crystal. In this approximation

the speed of light inside the medium is

$$v = \frac{c}{n_0 + n_E \sin(\omega t)} \quad .$$

The time of flight t_f can be approximated as

$$t_f \approx \frac{L(n_0 + n_E \sin(\omega t))}{c} \quad .$$

Using the time of flight we can deduce the time-dependent part of the induced phase shift Φ accumulated along the length L of the crystal:

$$\Phi(t) = 2\pi v \left(t_f - \frac{L}{c} n_0 \right) = 2\pi \frac{L}{\lambda} n_E \sin(\omega t) \quad .$$

Thanks to the Fourier theorem any periodical function has a discrete spectrum. Any harmonic modulation at frequency $v = \omega/(2\pi)$ modifies the spectrum of the laser, generating additional frequencies spaced by v in frequency domain. The new frequencies closest to the carrier are the 1st-order sidebands and the ones lying at frequency mv to the carrier are referred as the m-th order sidebands. The modulation depth

$$b = 2\pi \frac{L}{\lambda} n_E \tag{1.4}$$

is inversely proportional to the wavelength. This reduces the efficiency of the modulation at 3.1 μm as compared to optical radiation where these devices are normally benchmarked. Experimentally we noticed that with the available setup and 10 W radiofrequency power the modulation depth was still quite limited, reaching $b = 0.48$ rad and $b = 0.71$ rad for the 1490 MHz and 665 MHz modulators, respectively. Little modulation leads to very weak sidebands, and the overall power must then be increased considerably to reach saturation of the atomic transition using a sideband. However, high power is to be discouraged as excited states of La$^-$ may absorb a second photon from the laser and be photodetached.

To increase the modulation depth with the use of a single crystal, the light can be reflected back, such as to travel through each modulator twice. By reflecting the light right at the end of the crystal modulating at 665 MHz the depth increased from 0.71 rad to 1.3 rad. The measurement of the modulation effect for 665 MHz obtained with a scanning Fabry-Perot cavity is presented in Fig. 1.15. Conversely, For the 1490 MHz modulation, by reflecting the light right at the exit of the crystal, the modulation signal was lost. This is due to the speed of the phase change induced by the crystal compared to the time of flight of the light through the modulator. The elapsed time Δt between two subsequent passages of the beam in the middle of the modulator depends on the position of the mirror. Carefully selecting the distance of the reflecting mirror allows tuning Δt in order to obtain a deeper modulation. The optimal value of the additional optical path is such that the time of a subsequent pass matches the period of the modulation; in this way the imprinted phase is coherently added to the previously obtained shift. For the 1490 MHz modulation, the optimal distance of the reflecting mirror from the exit face of the crystal should be $d = 57.4$ mm. This value is remarkably close to the crystal dimension, and the position of the mirror was, therefore, found to be critical. By respecting this condition, it was possible to increase the modulation depth from $b = 0.48$ rad (obtained with a single-pass) up to $b = 0.72$ rad with the round trip. Placing the mirror to match the phase condition over a round trip was not necessary for the 665 MHz modulation since, in this case, the optimal distance is much larger than the crystal length ($d = 182$ mm).
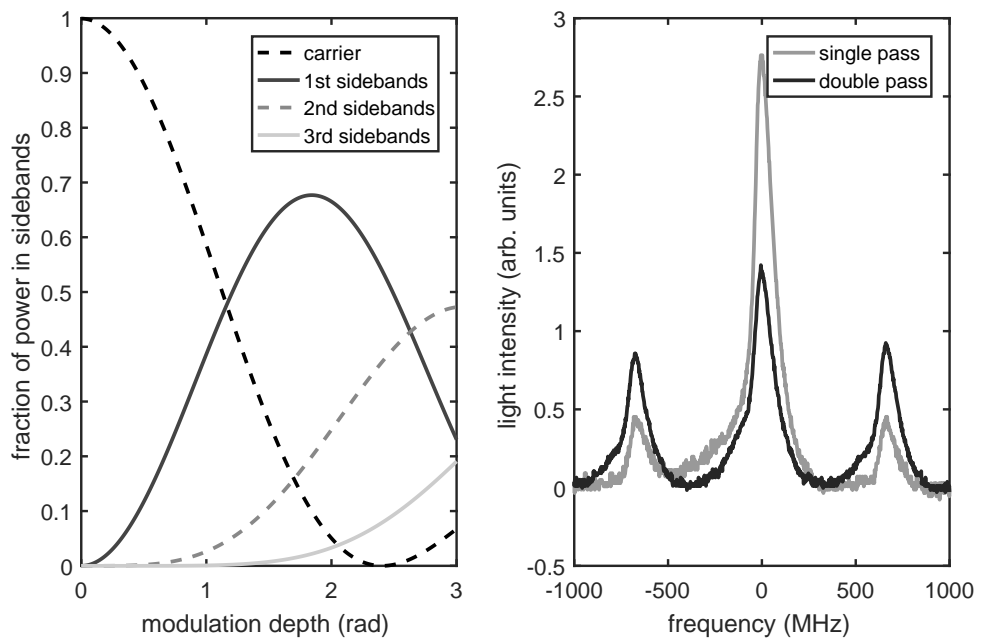
Figure 1.15: The left pane shows the relative power driven into the sidebands at different phase modulation depth b (Eq. 1.4 in the text). The right pane shows the measurement of the sidebands of the 665 MHz modulator performed by scanning Fabry-Perot cavity. In the plot of the transmitted intensity as a function of frequency. In single-pass configuration $b \approx 0.71$ rad to and in double-pass $b \approx 1.3$ rad.

Chapter 2

Spectroscopy on the La⁻ atomic ion

2.1 Atomic anions laser cooling candidates

Electron affinities of atoms commonly range between 1...3 eV. These values are typically lower than the binding energy of neutral atoms and more comparable to the solid-state physics energy scale. Thus, investigation of the level structure in atomic anions is comfortably accessible with standard solid-state laser technology and typically performed with electromagnetic waves ranging from the optical to the far infrared wavelengths.

Photodetachment of the extra electron and detection of the electron or the resulting neutral atom is an established method in anion experiments. Particle detection does not suffer from several drawbacks associated with photon measurements, such as low efficiency detector for infrared radiation. High-sensitivity detection of particles is made possible thanks to channeltron or MCP detectors by which small currents are amplified in an avalanche process. The tremendous amplification obtained with this technology allows the discrimination of faint events generated by single particles. Hence, transitions, electron affinities or cross-sections of different molecules/elements can be measured without changing the detection scheme, regardless of the particular photon energy used.

The disappearance of the negative ion due to photodetachment or chemical reaction is typically adopted as the signal in trap experiments. In [94], the anions are trapped in a radiofrequency trap that, however, cannot confine the light e^- and the neutral particles. Photodetachment leads to the separation of the two components, modifying the storage time of anions in the trap.

The detection of the emitted electron is the second option for negative-ion studies. In the Velocity Image Spectroscopy (VIS) [47] technique, the outgoing lepton is projected onto an MCP detector equipped with a phosphor screen. The accelerating field collects the electron after detachment and ensures the detection of all possible events. In the final result, the entire solid angle is mapped to an image visible on the screen of the detector. In two random repetitions of the photodetachment process, the different initial velocities of the two electrons affect their trajectories and makes them appear as separated events on the phosphor screen. The technique takes advantage of the fact that the leaving electron is practically not influenced by the neutral atom left behind aiming to capture the momentum of the electron emitted by its parent anion. The detected momentum vector further contains information about the electron wavefunction that can be used for an accurate study of the anions.

Detecting the neutral particles is the alternative option in negative ion studies. Neutral particles are largely insensitive to electric and magnetic fields that can separate charged anions from neutral atom trajectories. Usually, this detection scheme involves straight particle beams. Physical alignment of beam and detector is easily achieved by optical methods, and detectors readily intercept neutral particles which preserve their direction of motion. Anions are deflected away, for current monitoring, or bent into the circuit of a storage ring [89]. Alike the electron case, different arrival positions on an imaging detector can give insights over the initial particle momenta.

Experiments designed to capture one of the fragments are simplified if performed on a beam of anions in a field free region, where the interaction with the laser radiation takes place. In this configuration, the fragile anion systems are left unperturbed by static fields, and no shift in the energy levels occurs. The electron collection is typically performed aside from the beam axis, while the neutral atom is customarily detected forward.

All the following atoms in the periodic table of elements have been predicted to have a dipole allowed transition: Os^-, La^-, Ce^-, Gd^-, Tb^-, Th^-, Pa^-, U^-, and Np^- [68]. Unfortunately, only the first three of the previous list have excited states observable by tunable continuous-wave lasers radiation. The transition energies of the others are, in fact, in most cases below 0.3 eV or less and only in Os^-, La^-, Ce^- were expected to have a dipole allowed transition lying > 0.3 eV above the anion ground state. A small number of experimental groups have investigated the properties of the dipole allowed transitions in the laser cooling candidates Os^-, Ce^- and La^- by detecting the neutral fragment of a beam.

Osmium was identified experimentally before any other [39]. Lanthanum and cerium were the-

oretically predicted to be good candidates and later investigated experimentally [56, 82]. The spectroscopy spanning several transition lines proved to be crucial in the identification of the transition frequencies that, in some instances, deviated more the 15% from the predicted values. Finally, only Os⁻ and La⁻ showed promising properties for laser cooling applications.

The suggested cooling technique for these ions was Doppler laser cooling. The method requires fast cycles in order to repeat the absorption and re-emission of photons a large number of times. The two candidates (La, Os) were pinpointed thanks to their relatively fast transition in comparison to the other atomic anions. However, these ions become neutral upon absorption of a photon from the cooling laser in the excited state [69]. This feature is useful for spectroscopy as we will see, nevertheless it is not an advantage for laser cooling. Detachment from the excited state implies a reduction of the number of negative ions present in the system during cooling.

The anions must relax to the ground state to repeat the photon absorption several times. Other quantum states accessible during the relaxation of the system from the excited state can compromise the cooling by breaking the closed cycle. In these *dark states* anions can remain for a long time while not interacting with the laser radiation. For this reason, the probabilities of decay towards different states (*branching ratios*) were studied [68, 69]. Lanthanum was predicted to have better characteristics in this regard. Excited Os⁻, as compared to La⁻, was predicted to decay more easily towards dark states on the fine structure multiples of the ground state. These states would require additional lasers to prevent the cooling from stopping.

Contrary to the Os case, the absence of a zero nuclear spin isotope of La induces hyperfine splitting in the laser cooling transition, complicating the cooling scheme. Unfortunately, the past literature never tackled the implications deriving from the nuclear spin. We addressed this issue after revealing the hyperfine structure via high-resolution spectroscopy [85].

Starting from these preliminary theoretical and experimental works, the first aim was to improve the knowledge of the transition frequencies and transition rates. Osmium was the first anion studied experimentally, and therefore it was the first investigated at MPIK in the UNIC experiment [62, 64, 74, 81]. Because the transition of Os⁻ was found to have unfavorably slow relaxation rate (50 Hz), La⁻ was consequently left as the only possible alternative, with the advantage of an expected relaxation rate 100 times faster than in Os⁻.

During this work, spectroscopy on the laser cooling transition in La⁻ was performed. In a first experiment, we measured the transition frequency in a collinear spectroscopy setup. The spectroscopy was prepared from its design to realization, and contributing with the neutral particle detection technique. A description of the collinear experiment will be given below, but only data relevant to the subject of this thesis will be presented. Additional information and a detailed discussion can be found in [85] and [84]. Furthermore, a second experiment was developed to measure the cross-section of the transition in a mixed transverse and collinear setup. From these results we determined the spontaneous emission rate of excited La⁻.

2.2 Probing internal transitions

An Anion beam moving in a straight trajectory enters a region free from static fields. In this section two laser beams interact with the ions. The first tunable beam excites the anions to an excited state using a resonant frequency, while the second beam detaches the electron selectively from the excited anions. The second step (detachment) is possible only if the first (bound–bound excitation) is accomplished. The acquisition of a spectrum is hence realized by acquiring the rate of the neutralized particles as a function of the laser frequency as it is scanned through the resonance.

The selective photodetachment produces neutral atoms and electrons while some negative ions remain bound. An electric field removes the charged particles from the trajectory while neutral atoms proceed on a straight line and are thus counted by a detector at the end of the spectroscopy section. The
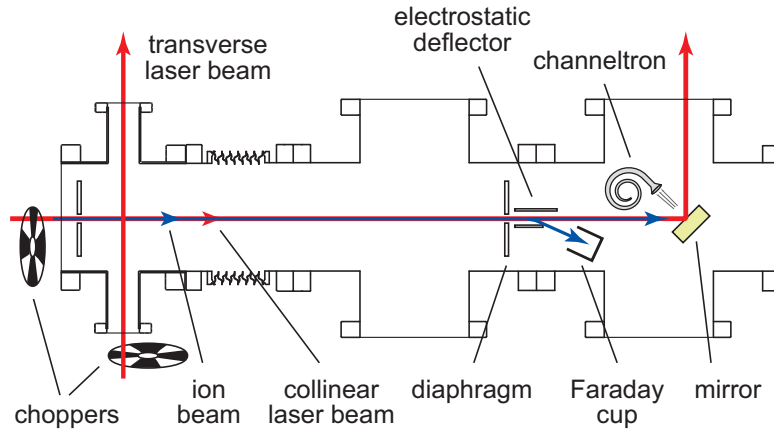
Figure 2.1: Sketch of the collinear/transverse laser spectroscopy setup (top view) with an overlap region of 730 mm. The ion beam is indicated by a blue line, the laser beams by red lines.
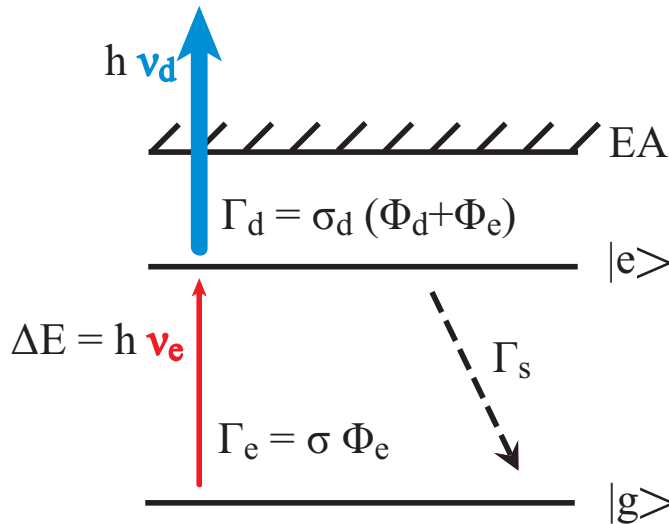

Figure 2.2: Simplified energy level diagram in a negative ion with the ground state $|g\rangle$, a bound excited state $|e\rangle$ and the electron affinity *EA*. The light radiations have energy $h\nu$, photon densities ϕ, and they induce transition rates Γ depending on the cross-section *sigma*. The photodetachment (subscript *d*) light has higher power than the excitation radiation (subscript *e*) because the photodetachment cross-section σ_d is much lower than than cross-section σ of the resonant transition. In our spectroscopy experiments the contribution to the photodetachment rate $\sigma_d\phi_e$ and the spontaneous emission rate Γ_s could be neglected.

count rate can be affected by fluctuations in beam current due to several causes. Thus the charged particles are deflected from the ion beam, at the end of the field free region, and enter a Faraday cup for current monitoring. This current is used to normalize count rate against the total number of anions in the beam.

In Os^- and La^-, the photon energy needed to generate the excited state is higher than the binding energy of that state. It follows that the radiation driving the bound–bound transition may also detach the electron from the excited anions. Thanks to this property, the first experiments surveying the spectra of Os^- and La^- ([39], [82]) were carried out with one laser wavelength only. A pulsed laser beam was directed transversely to the anion beam while the neutral atom count rate was measured. Having just one laser simplifies the experimental setup, but it imposes a severe limitation for precision measurements. The drawback is connected to the enormous difference in cross section of the internal resonant transition ($10^{-12} \dots 10^{-15}$ cm^2) compared with the cross section of the photodetachment process (10^{-17} cm^2). Whenever enough power is used to strip off the extra electron from the excited ion, power broadening affects the signal of the observed transition. Conversely, when the ion is stimulated at the correct power level, the acquired signal is rather weak because the electron detachment is very unlikely to happen. If the bound–bound transition and photodetachment are driven independently, both requirements can be met at the same time. Power broadening can be intuitively understood from the uncertainty principle. If the provided light fluence is large enough to drive the transition much faster than the natural relaxation time, this short excitation time becomes dominant in determining the width of the spectral line. The broadening in the case of La^- could be as large as several hundreds of MHz in our apparatus, thus blurring the hyperfine structure of the transition. In comparison to the previous measurements by other groups, the lasers used in the UNIC experiment produce continuous-wave light and have a narrow linewidth of a few MHz. Since the precision of the analysis was enough to appreciate the effects of power broadening, the separation of the two steps was required. The increased resolution obtained by suppressing power broadening helped to determine the frequency values with higher precision and allowed resolving the hyperfine structure of the transitions.

High resolution spectroscopy on Os^- performed with the UNIC apparatus [62] was actually slightly simpler and did not require two radiation fields. Yet it required the separation of the two steps of excitation of the bound–bound transition followed by electron detachment. Due to the weak binding energy of the excited state of 11 meV, the detachment of Os^- is possible by stripping the electron with the electric field generated in a stack of three mesh grids traversed by the beam. The central mesh is placed at high voltage whereas the external grids are referenced to the rest of the apparatus. Spectroscopy of Os^- was achieved by exciting the resonant transition with a collinear laser beam [63]. The laser beam and the neutral particles impinged at the end onto the face of an MCP detector. This solution was not viable in the case of La^-. The excited state in La^- has about 100 meV binding energy, and the limitation imposed by the voltage discharge limit among the grids made electric field detachment prohibitive. The neutralization of La^- had to happen upon absorption of an extra photon, as suggested at the beginning of this section.

The modification developed in this work of the final MCP detector with the adoption of a gold mirror faced by a channeltron made the measurement possible. The mirror fulfills two different functions, both serving as secondary electron emitter and redirecting light into the experiment from the opposite direction (*anti-collinear*). Upon impact on the mirror, neutral atoms release secondary electrons from the surface, which are then detected by the channeltron. The important consequence of the new design was the added possibility of using the same laser both for excitation of the bound–bound transition and the detachment of the electron. Despite the monochromaticity, as a consequence of the Doppler effect, the ions traveling into the spectroscopy chamber perceive two different frequencies in the rest frame. The collinear light appears for the anions red detuned, while the anti-collinear light is instead perceived as blue shifted. The Doppler shift is much larger than the natural width of the transitions and the situation is thus equivalent to two different lasers being superimposed with the anions. The continuous light field coming from the
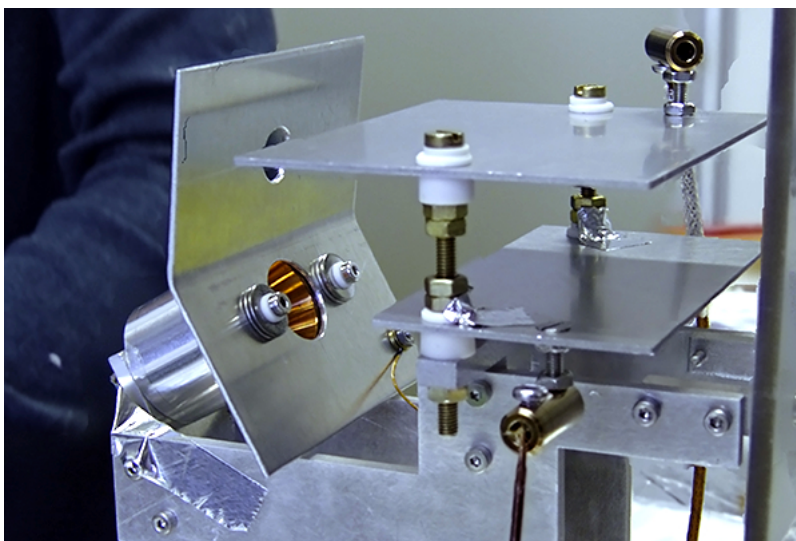
Figure 2.3: Photo of the final deflector region. A suitable voltage applied to the plate electrodes directs the charged anions into the Faraday cup (copper). Neutral particles fly straight through the round aperture.
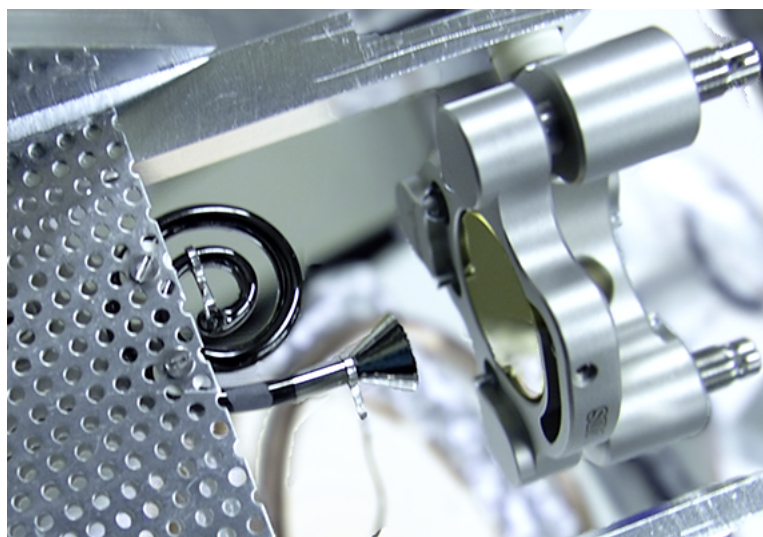

Figure 2.4: Photo of the channeltron detector facing the gold mirror. The 1-inch (25.4 mm) mirror is mounted after the aperture of the final electrostatic deflector in Fig. 2.3.

OPO system (Aculight Argos Model 2400, OPO Module B) was therefore split on the laser table and sent onto the anions from both directions. We carefully tuned the power of the resonant beam to avoid power broadening.

Furthermore, the new detector with the mirror, in comparison with a simple MCP, reflects the light away from the vacuum line. The significant light power used for the photodetachment (≈ 1 W) is hence not released on the delicate surface of the detector which can be damaged instead.

2.3   Detection via secondary electrons

Secondary electron emission is the phenomenon in which a particle impinging on a surface can remove some bound electrons. In this work a detector based on a gold mirror and a channeltron detector was realized to collects and amplifies these electrons as well as reflect infrared light.

This experimental setup was not the first one exploiting secondary emitted electron in the detection scheme. In [88] a similar setup in a storage ring is mentioned. There, a gold-coated glass plate is both the transparent window transmitting the laser and the secondary electron emitter. The transmission coefficient of such a window is substantially lower for IR radiation than the $\approx 95\%$ reflectivity of a gold mirror. Electroplated gold mirrors, based on copper substrates, are readily available on the market without any coating. They are normally adopted in CO_2 laser application Instead of gold, other materials like SiO_2 could be considered acceptable. Silica is widely adopted as a protective coating layer on a lot of commercially available optics of metallic mirrors. However, silica must be used with a correcting voltage under the silica layer as shown in [45]. This precaution eliminates the bulk effect accompanied by the charge up of the insulating material, which could modify the detection efficiency of the system.

Emission of secondary electrons is studied by accelerating electrons with a constant electric potential onto a flat target usually mounted orthogonally to the beam direction. The measured current of *primary electrons* I_{PE} is compared to the generated current of *secondary electrons* I_{SE}. The quantity $\delta = I_{SE}/I_{PE}$ is the number of secondary electrons emitted on average for a single primary electron impinging on the sample. An analytical expression for the SE yield is known as the *universal curve* that is given by [59]

$$\delta = 1.28 \, \delta_m \left(\frac{E_{PE}}{E_{PE}^m}\right)^{-0.67} \left(1 - \exp\left\{\left(-1.614 \left(\frac{E_{PE}}{E_{PE}^m}\right)^{1.67}\right)\right\}\right),$$

where E_{PE} is the primary beam energy; the value of δ_m and E_{PE}^m are determined experimentally. δ_m is the maximum of the function δ which occurs for the primary electron energy of E_{PE}^m.

The maximum yield δ_m increases with the work function. This may seem surprising because a higher work function implies a greater barrier for the electrons to escape from the surface. Nevertheless, δ_m is proportional to the square root of the work function. This fact is attributed to the avalanche process that single scattered electrons may initiate inside the material. In the case of gold the experimental values of the characteristic quantities can be approximated by $\delta_m = 1.5$ and $E_{PE}^m = 0.5$ kV [44]. Other correcting effects have to be considered that modify the yield predicted by the universal curve. For instance, the smoothness of the surface has been shown to influence the process since an increased surface roughness can decrease secondary electron emission [38]. This evidence supports the adoption of a surface polished to mirror grade.

Furthermore, in the latest design, the 25,4 mm circular gold mirror was mounted at 45° to the incoming direction of the neutral atoms. This inclination angle is primarily arranged to reflect the collinear laser light outside the vacuum chamber as well as to introduce the anti-collinear beam. The dependence of secondary electron emission on the incidence angle to the sample can be expressed analytically. Following the description in Ref. [36] the universal curve of a tilted surface depends on the tilt θ and the kinetic energy of the primary electron. The tilt increases the yield of secondary electrons. In fact, an electron impinging on a tilted surface interacts for a longer path in the proximity of the emission region, and the initial momentum is split into an additional component taken away from the implantation
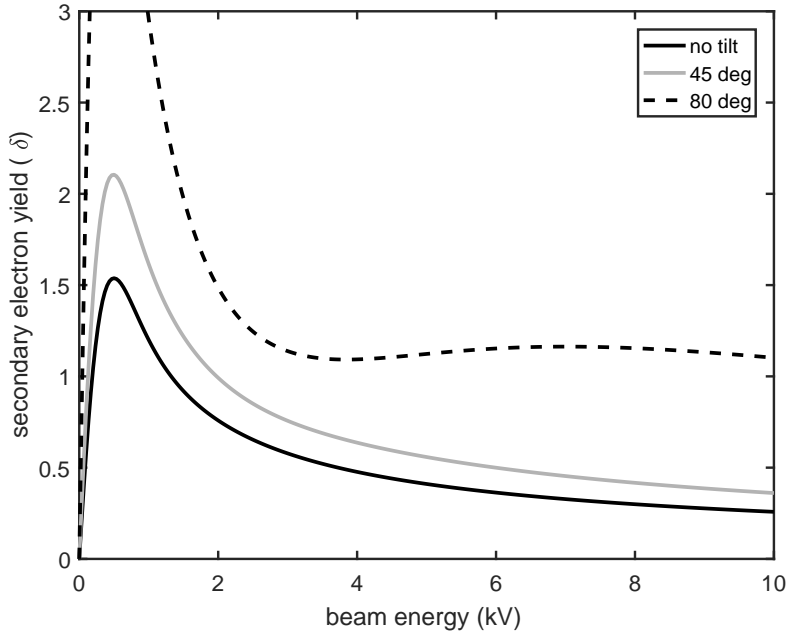
Figure 2.5: Calculated secondary electron emission from gold. Different curves correspond to different angles between the normal to the surface and the incoming particle. The spectroscopy on La$^-$ reported in this work was performed with a mirror tilted 45° with respect to the incoming neutrals. The collinear measurement in [85] was made at larger angle, closer to 80°.

direction. The universal curve depending on tilt and energy is given by the following formula:

$$\delta(\theta) = \delta(0) \; \frac{\xi - \cos(\theta)}{1 + (\xi - 2)\cos(\theta)} \; ,$$

where ξ is the upper limit of the quantity $\delta(\theta)/(\delta(0)\cos(\theta))$ for a given beam energy. The value of ξ was only experimentally investigated in Ref. [36] where it is reported as a function of the energy of the primary electrons. Based on this equation, we calculated an effective value of δ for the relevant experimental conditions in which we carried out the spectroscopic studies on La$^-$ (Fig. 2.5).

To conclude, the initial beam energy, the surface smoothness, and the tilt ensured that every neutral particle could produce on average between 0.5 and 1 secondary electrons. The mirror potential was set to obtain an acceleration stage between the channeltron aperture and the mirror surface. A potential difference of 500 V was found optimal for acquiring the signal. Indeed, [2] describes an expected peak efficiency in the initiation of the avalanche process approximately at this energy. A 90% quantum efficiency of the detector is predicted in this configuration. By detecting neutralized atoms, we could rely on an extremely high sensitivity, closer to single events and not orders of magnitudes lower. Moreover, the absolute value of the count rate was never considered in the measurements. The experiments were designed to rely only on relative count rates during the data analysis. Therefore, the assessment of the absolute performance of the detector was not further investigated.

2.4 Collinear frequency measurement

Resonantly exciting an atomic system requires a defined frequency to match the system resonance. The frequency of the electromagnetic radiation measured in the laboratory differs from a system which moves in the laboratory frame due to the Doppler effect. If the angle between the direction of propagation of the laser light beam and the anion beam is varied, the anions perceive a frequency of the radiation depending

on the angle. We used this dependence to obtain different radiation frequencies on the anions, without the need of multiple laser systems. A monochromatic laser radiation was split on the laser table and inserted into the interaction chamber from different directions. Only one of them was made resonant with the bound-bound ion excitation. The light power of this resonant beam was kept low and optimal to drive the inner transition so to avoid power broadening. In fact, by progressively lowering the intensity, and hence decreasing the power broadening effect, a lower limit in the peak line width in the spectrum was found at ≈ 75 MHz. We attributed the limit to several factors including the thermal spread of the anions into the production region, but also imperfections in the beamline. Conversely, the light power of the laser beam introduced from the opposite direction was kept maximal to detach the electron as efficiently as possible. For this reason, we will refer to the laser light driving the bound-bound transition as the *excitation* beam and the other as the *detachment* beam.

In the experiment with Os$^-$, only the excitation beam was present and sent collinearly to the ions because the detachment of e$^-$ was realized by using electric fields, as already metioned in Sec. 2.2. The spectrum was acquired by modifying the laser frequency, and thus scanning the entire resonance profile. To calculate the rest frame frequency of the transition, several spectra at different anion beam velocities were acquired. The laboratory frequency at zero velocity was extrapolated from those data. In the case of La$^-$, both a collinear and an anti-collinear laser beams were used. The roles of the two light beams could be exchanged, allowing anti-collinear excitation to be added into the data set. In this way, the rest frame frequency was no longer extrapolated, but instead interpolated. This method reduced the associated uncertainty by combining data with positive and negative beam velocities.

Several beam components and confounding events affect the neutral count rate. If the anion beam is correctly aimed towards the final detector, some neutrals will be observed regardless of the presence of laser radiation. These counts come from anions neutralized by collisions with the collimators and the residual gas present in the vacuum chamber. If non-resonant laser radiation is superimposed to the anions, more neutral atoms are registered. The increased count rate stems from spurious contaminants like neighboring mass constituents traveling in the beam, but mainly anions which are already populating the excited states. These anions can lose their electrons by absorbing a single photon. We constantly measured these background signals excluding their contributions from the final results. To summarize the following neutralization rate are present during the experiment:

- The background count rate k in absence of light.

- The rate of photodetached anions by absorption of a single photon from one of the two laser d_1.

- The rate of photodetached anions by absorption of a single photon from the other laser d_2.

- The count rate of anions excited by the excitation laser and detached by the detachment laser c.

Two synchronized mechanical choppers intercept the light beams, preventing them from interacting with the anions part of the time. Four measuring states are possible depending on the position of chopper blades. The first count rate $c_{11} = c + d_1 + d_2 + k$ is registered when both excitation and detachment beams are superimposed to the anions. The second and third states ($c_{10} = d_1 + k$ and $c_{01} = d_2 + k$) are met when either of the choppers occludes a beam. In the last condition $c_{00} = k$, the anions propagate in darkness. The output signal c is obtained by subtracting the counts with one or the other laser illuminating the ions from the one obtained with both lasers interacting. To correctly take into account the background, the counts acquired with both lasers off must once again be added, hence:

$$c = c_{11} + c_{00} - (c_{01} + c_{10}) \,. \tag{2.1}$$

The signal of anions absorbing two photons from the excitation beam is hence lost, but negligible most of the time because of the low power adopted to reduce power broadening; which was low enough to suppress the contribution to electron detachment. The calculated rate c was finally normalized by the

recorded ions current and laser power; the latter was monitored continuously using a power meter by collecting the partial reflection on a transparent CaF_2 window mounted on the laser table.

In order to measure the cross-section of the transition new viewports for transverse illumination were introduced in the experimental setup. The transverse laser was selected as excitation beam. The detachment beam was guided collinearly and reflected back at the end. Due to the incidence angle and Doppler shift dependence, neither collinear direction was resonant in the rest frame of the anions. Therefore the collinear and anti-collinear beams could be considered to be the *detachment beam* of the previous discussion. Furthermore, the transverse excitation direction did not suffer from the Doppler shift observed in the former setup. In the transverse geometry, the excitation occurred in an experimental region free electric fields, while in the collinear setup the anions were already illuminated in the electrostatic bender. This causes a characteristic asymmetric shape of the resonance elongated towards the rest frame frequency in the spectrum. Above all, the enormous difference in interaction times and path lengths of excitation and detachment beams secured the independence of the two processes, decoupling the rate equations of the system (Sec. 2.6).

Nevertheless, collinear excitation has some advantages over the transverse. First, it is not very sensitive to misalignment because the absolute Doppler shift scales with the cosine of the angle between anions and laser directions. The cosine coefficient corrects the frequency as a second order effect in the tilt. Conversely, an angular error from the transverse direction may affect absolute measurements with a larger systematic contribution, due to the sine (first order) dependence. In the practical realization, it is also challenging to know this angle and control the relative position of the anions and laser paths. The collimation apertures in the collinear direction constitute an accurate control over the possible tilt that translates into a few MHz deviation in the final absolute uncertainty. In comparison, the alignment of the transverse configuration was found more critical. We recognized an induced 50 MHz uncertainty in the absolute frequency determination caused by possible angle mismatch. The second advantage of collinear spectroscopy over transverse is the *velocity bunching effect* that reduces the Doppler broadening of the spectral lines. At generation, the anions have velocities dispersed by their thermal velocity spread and are accelerated by a constant electric field. Slower anions accelerate longer than the ones produced with higher initial speed, thus reducing the initial thermal energy spread. Thanks to the velocity bunching effect the apparent line width of each peak was about 75 MHz as compared to later measured value of 120 MHz obtained with transverse excitation.

2.5   Doppler-free spectroscopy

A prerequisite for the cross-section measurement with the transverse excitation scheme was the confirmation of the resonance shape previously acquired in collinear configuration [85]. We could in this way confirm our previous experimental result with the new setup and determine the precise frequency for measuring the cross section of the laser cooling transition (Sec. 2.6). We used the *Doppler free saturation spectroscopy* technique to improve the experimental resolution, to align the transverse laser beam and to reduce the absolute uncertainty of the measurement. The Doppler-free spectroscopy technique relies on the precise alignment of laser beams to record the signal coming from a specific velocity class inside the anion beam. Therefore, provided enough anion current is present, the precision achievable in experiments is no longer associated with the imperfection of the ion beamline. It is rather the properties of the laser system and of the interaction region that become crucial in determining the final precision.

Doppler free saturation spectroscopy relies on the superposition of two counter-propagating laser beams that interact with the anions. The secondary beam was generated by reflecting back the primary transverse beam on itself. The uncertainty in superimposing the reflected beam on the primary beam was measured to be 1.4 angular mrad. Locking the reflected light on the primary beam was fundamental for ensuring the mutual orthogonality of the laser beam and the ion path. The angle between anions and lasers is, in fact, critical for an absolute frequency determination since the Doppler shift scales with the

sine of the tilt angle from orthogonality.

The alignment was done according to the following procedure. A shutter with a 4 s period is introduced to selectively occlude the reflected beam. Two data sets are obtained by scanning the laser frequency with the shutter opened and closed. One spectrum corresponds to a single transverse beam excitation, and one acquisition stems from the double-pass configuration. The single-pass frequency response shows the typical structure of the resonance spectrum containing the known hyperfine peaks. In double-pass configuration, this spectrum structure is present in a regular and in a duplicated structure. The two structures are due to the two exciting radiations not crossing at right angle. This fact justify our decision of fixing the mutual position of the incoming and reflected laser. If one beam is slightly chasing the anions the other is in the same measure colliding, therefore producing a duplicated peak structure in the final result in a controlled way. We actively used this property to correct the misalignment and ensure a perpendicular interaction with the anion beam.

The typical shape of each hyperfine peak in the spectrum is Gaussian. If the laser is red-detuned it excites those anions with a slight velocity component towards the incoming direction of the laser, and vice-versa if the laser is blue-shifted it excites the one with a receding velocity component. Thus the reflected beam doubles, in general, the acquired signal. The count rate is doubled because two symmetric velocity classes are excited at the same time. For example in the case of a red-detuned frequency, some ions moving towards the primary beam as well as some ions moving toward the reflected beam are excited. The doubling of the count rate can only be met for detuned light. Only far from resonance. Exactly on resonance, the two lasers interact with anions belonging to the same (zero) transverse velocity class. In this frequency region, where competition for the same anions occurs, the doubling is no longer possible and a characteristic *dip* appears in the spectrum. The dip is a sharper feature than the Gaussian profile and, since it is due to a single velocity class, the spectroscopy technique is considered free from the first-order Doppler effect. The dip appears only under the condition that the beams are competing in exciting the anions, a circumstance met if the system is in saturation. This peculiarity gives the technique its name.

For any line in the spectrum, each of the two transverse laser beams (incoming and reflected) is expected to generate a Gaussian profile, that appears superimposed after the alignment procedure. Only the Gaussian line produced by the direct beam can be observed. It is evident that it is impossible to measure both Gaussians because one beam is the reflection of the other. However, the following assumptions can be made. First, the two individual Gaussians have the same symmetry as the combined double-pass signal. Second, the two Gaussians have the same height and width. In support of the latter hypothesis, the power reduction after reflection was not significant and the Doppler broadening of the line cannot have been different.

Observing the peaks in the acquired single-pass spectrum, it is possible to resolve the transitions $11/2 \longleftrightarrow 9/2$ (peak 1), $9/2 \longleftrightarrow 7/2$ (peak 2), $7/2 \longleftrightarrow 5/2$ (peak 3) and the last composite one (peak 7). Transitions are listed by total angular momentum F of the ground (left) and excited states (right). For these lines, the Doppler-free signal was calculated with the following analysis. We calculated the mean frequency μ_1 and width σ_1 of the Gaussian from the single-pass data. The symmetry point of the frequency μ_0 of the double-pass spectrum was also measured. The mean frequency of the Gaussian of the reflected beam μ_2 was calculated using the relation $\mu_0 = (\mu_1 + \mu_2)/2$. We then subtracted the sum of the Gaussian profiles from the data of the double-pass configuration. The extracted spectrum, i.e., the filtered dip signal, was finally fitted with a Lorentzian profile (Fig. 2.6).

For the $9/2 \longleftrightarrow 9/2$ (peak 4), $7/2 \longleftrightarrow 7/2$ (peak 5) and $5/2 \longleftrightarrow 5/2$ (peak 6) transitions this analysis was not viable because their Gaussian profiles appear superimposed to each other in the single transverse data. For these peaks, a spectrum including all peaks plus the $7/2 \longleftrightarrow 5/2$ transition was recorded in the same geometrical configuration used for the peak 1 transition data. The results obtained with peak 1 transition were hence used in the data analysis of this spectrum. The width σ_1 was assumed as the width for all four Gaussian profiles that supposedly composed the signal. The single-pass signal
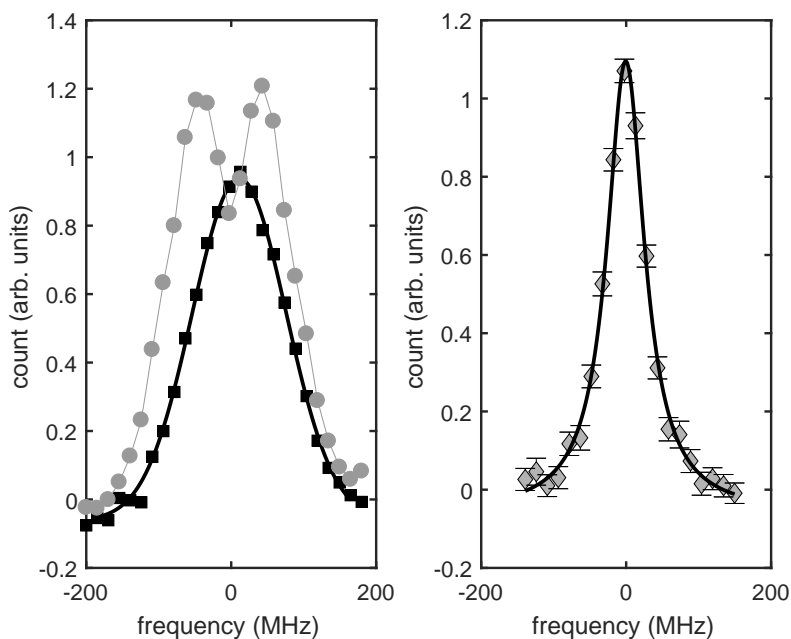
Figure 2.6: Data of the 11/2 ⟷ 9/2 hyperfine transition. Left pane: single (black) and double (gray) pass signal of transverse spectroscopy. The solid black line is a Gaussian fit to the data while the gray line helps to guide the eye. The dip resonance is calculated as described in the text and shown separately in the right pane, where the solid line corresponds to a Lorentzian fit to the data.

was thus fitted by the sum of four Gaussian profiles with frequencies and amplitudes as free parameters. The shift $(\mu_1 - \mu_2)$ of the peak 1 was also used to calculate the contribution of the reflected beam and provide the signal to be subtracted from the double-pass data. The fact that all available Gaussian profiles and frequency shifts are consistent with each other support the validity of the analysis.

The uncertainty of the rest frame of the transition was dominated by systematic effects. An uncertainty of 50 MHz comes from the wavelength meter used during the experiment (HighFinesse Ångstrom WS Ultimate 30 IR). Another 25 MHz is due to a possible misalignment of the two transverse beams caused by residual angle mismatch in superimposing one beam on the other. This corresponds to a potential shift of 47 MHz, which in turn due to the division by two coming from the Doppler-free technique contributes with 25 MHz o the total absolute uncertainty in the end result. We repeated the overall acquisition in two different conditions where the alignment procedure of the laser beam was repeated. Furthermore, some of the peaks were acquired more than once at different times within each configuration. The redundancy of the data was used in the analysis to check for possible mistakes in the alignment or the analysis. The results are consistent between the two sets.

We found the 11/2 ⟷ 9/2 (peak 1) transition at an absolute frequency of 96.592 014(05)(75) THz, in agreement with our previous measurement. Here the first parenthesis represents the statistical uncertainty and the second the systematic uncertainty. The values of the other transition frequencies are tabulated in Tab. 2.1. The width of the individual hyperfine peaks was reduced from $\approx$ 75 MHz in collinear spectroscopy to < 65 MHz in saturation spectroscopy, with the additional advantage of improved symmetry in the line shape. The linewidth is limited by the interaction time of the ions with the laser beam (time-of-flight broadening). The anions beam had a kinetic energy of 7 keV, allowing the interaction with the transverse beam for a fraction of a microsecond only. The improvement in the line width was therefore limited and, as in the prior work, the internal structure of the highest-frequency peak (consisting of three hyperfine transitions) was not resolved.

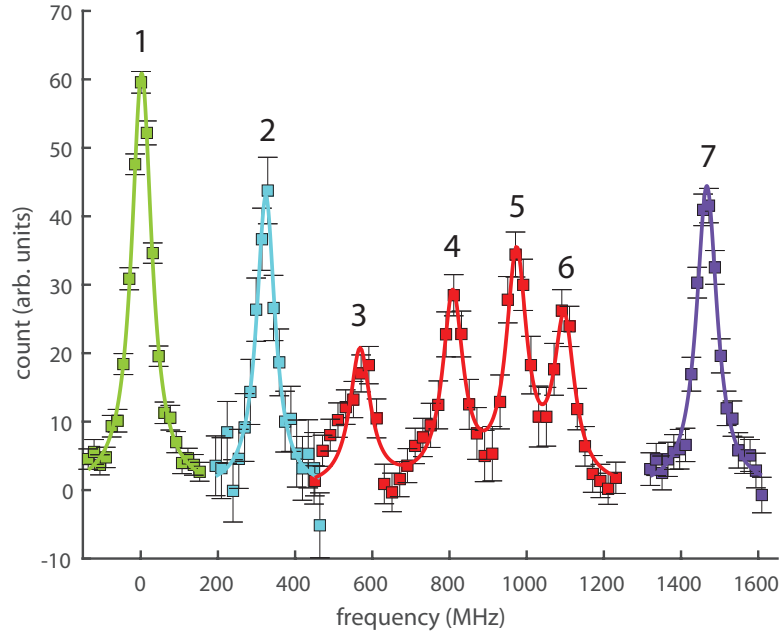Although the different Doppler-free lines were acquired at separate times, one general overview was

Figure 2.7: Composite graph of the $^3F_2^e \longrightarrow {}^3D_1^o$ resonance in La⁻, resolving its hyperfine structure. Different colors correspond to four different acquisitions combined in this plot. Solid lines are Lorentzian fits of the peaks. The FWHM of Peaks 1–6 was found to be 64.3(1.5) MHz.

Table 2.1: Hyperfine transition frequencies with respect to $11/2 \longleftrightarrow 9/2$ [at an absolute frequency of 96.592 014(05)(75) THz]. Transitions are listed by total angular momentum F of the ground (left) and excited states (right).

Peak no.	Hyperfine transition	Transition frequency (MHz)	
		Exp. [85]	this work
1	$11/2 \longleftrightarrow 9/2$	0.0(5.8)	0.0(3.5)
2	$9/2 \longleftrightarrow 7/2$	324.8(5.8)	321.6(4.6)
3	$7/2 \longleftrightarrow 5/2$	604.1(5.9)	585.8(5.8)
4	$9/2 \longleftrightarrow 9/2$	825.1(5.8)	814.2(5.2)
5	$7/2 \longleftrightarrow 7/2$	990.1(5.9)	977.2(5.2)
6	$5/2 \longleftrightarrow 5/2$	1116.2(6.1)	1102.5(5.2)
7a	$3/2 \longleftrightarrow 5/2$		
7b	$5/2 \longleftrightarrow 7/2$	1480.2(5.8)	1467.6(4.0)
7c	$7/2 \longleftrightarrow 9/2$		

recorded to obtain the entire spectrum in a single continuous acquisition. This single-pass spectrum was not considered for the frequency determination, but used to measure the relative peak amplitudes. In fact, the rapidly changing behavior of the source in delivering La⁻ and its contaminants could not guarantee compatibility among acquisitions of various peak acquisitions[1]. The amplitudes obtained with the overview measurement were used to normalize the final spectrum presented in Fig. 2.7, which was obtained by combining different acquisitions. The center-of-gravity frequency, in which the heights were used to weight the frequencies, is 96.592 713(52)(75) THz. The values are again in good agreement with our prior result of 96.592 80(10) THz. The statistical error is here considerably higher, caused by the uncertainties of the peak amplitudes.

2.6 Cross-section

The spontaneous emission rate is the primary parameter which determines the relaxation time of the atomic system and therefore the speed of the laser cooling process. Cooling of atomic systems has the meaning to reduce the coherent velocity in favor of a residual random velocity. This is obtained after many photons get absorbed and then emitted from atoms or ions because the momentum carried by each photon is typically tiny compared to the momentum of the particle. However, the fact that each photon perturbs the system only slightly is also the reason why so low temperature can be reached via laser cooling. In the process, a fast rate of the ground-to-excited-state transition is required to repeat many cycles in a reasonable amount of time. If the cooling time is too long other secondary effects may play an important role and prevent cooling from happening. For instance the photodetachment (cross-section of $\approx 10^{-17} \text{cm}^2$ [69]) of the excited anions by the cooling laser limits the time of the interaction since all anions may be destroyed without significant cooling. The spontaneous emission rate is, therefore, an important quantity to be measured.

A direct measurement of the spontaneously emitted photons using a beam of anions is complicated. The observation often implies long storage times that in a beam setup might be prohibitive. Direct measurements of such processes are typically performed in storage rings or traps where the system can be preserved, in contrast to a beam experiment where the duration is fixed by the geometrical extent of the apparatus. However, the decay rate is connected to the cross-section of the transition. The cross-section is the physical quantity which describes how strongly the laser field interacts with the anions in resonance. In other words, it is sufficient to determine how efficiently the transition can be driven using a laser field to calculate the lifetime of the excited state. Observation times involved in this type of measurement can be significantly smaller than the decay lifetime, thus opening up the possibility to collect the data over a finite path.

The cross-section can be deduced from the flux of photons ϕ that allows a significant fraction of the ground state anion to become excited in a definite amount of time (*fluence*). If sufficient fluence is provided, the two population densities of the ground n_g and excited n_e states tend to equalize. In this steady state regime, the laser moves the same number of anions from the ground state to the excited state that it de-excites in the reverse process of stimulated emission. The system is in equilibrium. In this situation, no variation in the population of excited anions can be achieved by increasing the laser power, and the system is said to be in saturation. Conversely, by reducing the laser power, fewer anions will be excited until a linear behavior is observed. In the linear regimen the number of excited particles is proportional to the fluence. Understanding for which light fluence the nonlinearity sets in is the measure of how much the laser radiation interacts with the system.

The rate equations for the densities per unit volume of anions of this simplified system can be ex-

---

[1]see Sec. 1.2 for the La⁻ source behavior

pressed as

$$
\begin{aligned}
n'_g &= -\sigma\phi\left(n_g - n_e\right) \\
n'_e &= \sigma\phi\left(n_g - n_e\right)
\end{aligned} \quad , \tag{2.2}
$$

where the constant σ is the cross-section of the transition. Only the difference of the population between ground and excited states enters into the equations, as a consequence of the interplay between excitation and stimulated emission. Note that radiative decay of the system was neglected assuming that the excitation time is sufficiently smaller than the spontaneous emission rate. The spontaneous decay would constitute an additional term that transfers the population of the excited anions back to the ground state after a long observation time. In beam experiments, the interaction time is typically fixed by the geometry of the system. The laser is superimposed with the ions in a defined region along the beamline, thus imposing a precise bound on the time the particles travel through the wavefield. The effect of saturation is nevertheless observable by varying the intensity of the radiation field, allowing a measurement of the cross-section.

The adopted setup to observe the nonlinearity in the excitation is already described in detail in the previous section 2.5. The experiment was conducted like the Doppler-free measurement, with the transverse beam driving the internal transition in combination with the collinear and anti-collinear lasers for detachment of the electron. There were only two main differences with respect to the previous design. First, in contrast to the Doppler-free measurement, just one of the two transverse laser beams was used, which, in this case, was locked to the resonance frequency of the $11/2 \longleftrightarrow 9/2$ transition. Second, we adjusted the laser intensity via a half wave plate and a polarizer. Tuning the laser power allows recording the relative number of excited anions as a function of the interacting light fluence by varying the photon flux and preserving the interaction time constant.

It is important to consider whether or not the detachment process plays any role in the final result. The collinear laser is present in the vacuum chamber for the entire length of the field-free path and thus interacts with the anions also in the position where the excitation laser crosses at a right angle. If a large fraction of excited anions are neutralized while excitation is taking place, a new state will come into play. The new channel corresponds to the possibility of losing anions from the system. For the La$^-$ system to be approximated by the suggested rate equations without this extra term, the effect of the electron detachment in the overlap region must be small. If this condition is not met, the variation of the excited-state population is influenced by the detachment laser power as well as by the detachment cross-section. In this way, the reason for upgrading the setup introducing the transverse excitation viewports becomes evident. Due to the larger interaction volume, the detachment step was measured much (30 times) more probable to be caused by the collinear beam. The volume difference is large enough to assume that the electron stripping is likely happening during the flight after the region occupied by the transverse laser. Furthermore, the fact that photodetachment by the collinear laser is 30 times more probable is a sufficient proof that the detachment laser power was far from saturation during the excitation section and thus not influencing n_e. For these reasons, we can disregard the effect of neutralization in the rate equations and considered the system to be closed. We will keep them in the simplified form of a two-level system, interpreting the neutral-atom signal as sampling the excited-state population after excitation.

The transverse laser setup was therefore fundamental in reducing the parameters in the mathematical description, leading to a simplified model to extract the cross-section. Nevertheless, it made the modeling of the excitation process more complicated than in a collinear apparatus. The anions probe the beam profile of the transverse laser while being excited as they sweep through it during the flight towards the detector at the end. Consequently, the volume integral and the solution of the differential equations are not as straightforward as for the collinear interaction case, where anions probe higher homogeneity of the field along the entire section.

The geometry of the experiment can be described in a 3D Cartesian system (x, y, z) where ions move along the z axis with velocity v. The velocity is determined by energy conservation from the accelerating
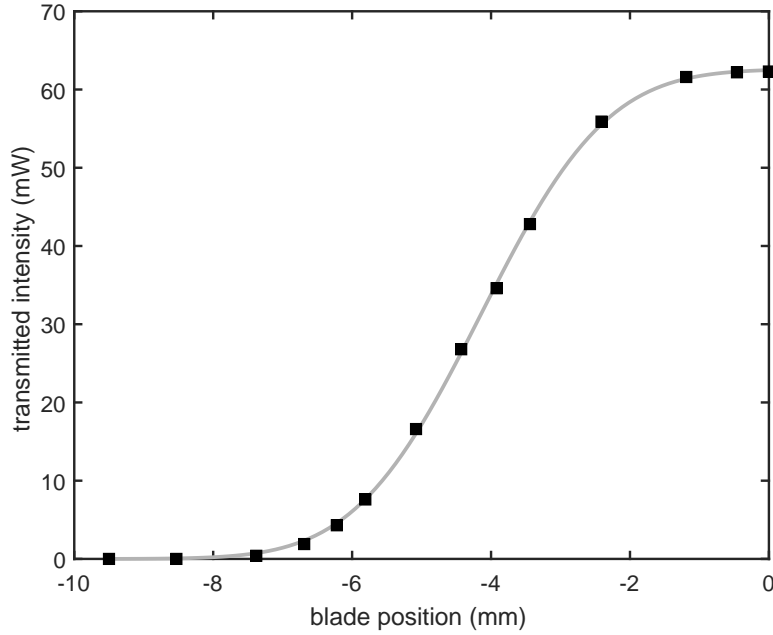
Figure 2.8: Measurement of the laser beam profile performed by progressively obstructing the beam with a blade while recording the transmitted power. The fit function $I_0\left(1 + \mathrm{erf}\left(\frac{x-\mu}{w}\right)\right)$. In this measurement $I_0 = 62.6(3)$ mW, $w = 2.86(4)$ mm and $\mu = -4.14(2)$ mm

voltage U, the charge of the electron e and the mass of the anion m so that

$$v = \sqrt{\frac{2Ue}{m}} \; .$$

The transverse laser propagation direction is along y. The measurement of transverse beam profile was performed by progressively obstructing the power of the beam with a blade from the transverse direction (Fig. 2.8). The measurements of the profile acquired outside the vacuum chamber are compatible with a well-collimated beam of Gaussian shape. We will use the following expression for the laser beam intensity:

$$W = W_0 \frac{2}{\pi w^2} e^{-2\frac{x^2+z^2}{w^2}} \; ,$$

where W_0 is the integrated power and w was found to be 2.69(5) mm. The photon flux ϕ can be calculated using the Planck constant h as $\phi = W/(h\nu)$. Since we need the photon flux we will make use of the relation.

To understand the boundary conditions of the differential problem it is important to consider the meaning of the final neutral rate extract in the experiment. Thanks to the choppers we measure the number of anions excited by the transverse laser and detached from the collinear anti-collinear pair. This signal is unbiased from the anions that could already be found in the excited state as well as any other contaminant that can be counted as neutral. Consequently we can assume that the anions enter the straight section ($t \approx -\infty$) with the following populations: $n_g(-\infty) = n_0$ and $n_e(-\infty) = 0$. The detector at the end does not discriminate the position of the neutralized anions in the beam, and only the total number of events is recorded. Thus the rate equations are to be integrated over the area A defined by the circular apertures of the spectroscopy section. Integrating both sides, the equation for the population difference $n = n_g - n_e$ is

$$\int_A d^2x\, n' = e^{\frac{2v^2t^2}{w^2}} n\left(-\sigma\phi_0 \frac{4}{\pi w^2} \int_A d^2x\, e^{\frac{2x^2}{w^2}}\right) \; .$$
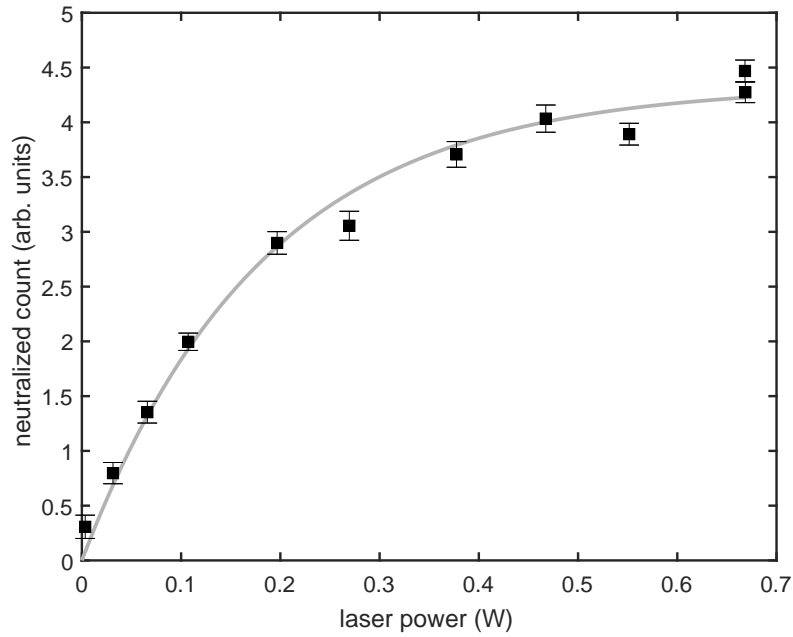
50

Figure 2.9: Relative number of excited La$^-$ anions as a function of laser power. The effect of saturation can be observed from the non linearity of the curve. The solid line is a fit to the data with the function $a\,(1 - \exp\{(bW)\})$ (see text).
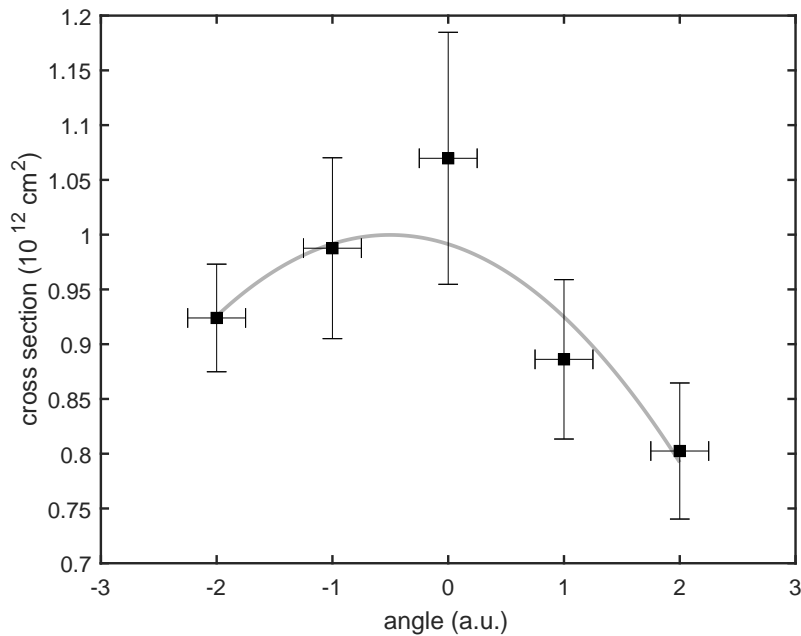

Figure 2.10: To ensure overlap of the laser and anion beams the incident direction of the laser beam was adjusted. For each position a cross-section value was calculated as if the overlap was perfect. The final cross-section value was extracted via a fit with the parabola $a_0 + a_1 x + a_2 x^2$ presented in the plot as a solid line. From the fit $a_0 = 0.991(51)$, $a_1 = -33(15)\,10^{-3}$ and $a_2 = -33(16)\,10^{-3}$; all coefficient are expressed in 10^{-12}cm$^-2$

The second rate equation, constituted by the sum of the two populations $n_g + n_e = n_0$, is trivial and implies the conservation of the number of anions. The spatial integrals account for the geometrical overlap of the anion beam with the laser light. We will assume here perfect overlap of the axes of the two beams and more importantly that the anions are homogeneously distributed over the area A of the circular apertures. In support of the uniform density hypothesis, it must be noted that only a small fraction of the ion current arrives at the end of the spectroscopy section. In fact, the extremely selective geometry induces a ten-fold reduction in the current, measured by comparing the data of two Faraday cups before and after the section. The field-free path is 730 mm long and constrained by the two circular apertures of radius $r = 3.25$ mm. The highly reduced acceptance justifies the reduction factor as the consequence of an imperfectly collimated beam that, expanding, is filtered by the apertures. Thus, the broadening of the ion beam supports the approximation of homogeneous density over the component crossed by the laser that potentially creates a neutral signal at the end. Only one tenth of the anions are guided to the end may deliver a signal, while the remaining fraction do not influence the final result.

Bringing the integrals of the spatial dependence to the right-hand side of the equation they can be absorbed into the coefficient g_c as follows:

$$g_c = \frac{1}{\pi r^2} \int_0^{2\pi} d\theta \int_0^r dR\, R\, e^{\frac{2R^2 \cos(\theta)^2}{w^2}} = e^{-\frac{r^2}{w^2}} \left(I_0\left(\frac{r^2}{w^2}\right) - I_1\left(\frac{r^2}{w^2}\right) \right) .$$

where I_n indicates the modified Bessel functions of the first kind. The coefficient g_c allows rewriting the differential equation in a simplified form and solving it by separation of variables:

$$\int_{N_0}^{N} \frac{dn}{n} = -\sigma \phi_0 \frac{4 g_c}{\pi w^2} \int_{-\infty}^{\infty} dt\, e^{\frac{2v^2 t^2}{w^2}}$$

Both integrals have analytical solutions leading to

$$\log\left(\frac{N}{N_0}\right) = -\sqrt{\frac{8}{\pi}} \frac{\sigma g_c \phi_0}{wv}$$

N, N_0 can be regarded as the total rate of particles per second corresponding to the populations n and n_0. The detectable number of excited anions N_e per unit time have therefore the following dependance with respect to the photon flux ϕ_0:

$$N_e = \frac{1}{2} N_0 \left(1 - \exp\left(-\sqrt{\frac{8}{\pi}} \frac{g_c}{wv} \sigma \phi_0 \right) \right) .$$

This curve was fitted to the acquired data to extract the cross-section. The advantage of fitting the number of neutrals as a function of the fluence makes the measurement independent from the detection efficiency. As the system is driven into saturation with high laser power, the number of detected neutrals does not change linearly, and only the variation is taken into consideration by the analysis. The absolute count rate plays no role in the relative change, and the information about the electron detachment efficiency can be ignored. An example of data set recorded is shown in Fig. 2.9.

In the previous calculation, the analytical solution could be found under the assumption of perfect overlap of the anion and laser beams. In the experimental implementation, this requirement was met by performing several measurements of the cross-section. The incidence angle of the transverse laser beam was adjusted by tuning the orientation of the last mirror coupling the light into the vacuum chamber. We changed the tilt in regular steps, measuring for each a cross-section value. The final value of $\sigma = 1.0(1)10^{-12}$ cm^2 for the cross-section is the maximum of the parabola fit of the preliminary data for various tilt angles (Fig. 2.10).

The relaxation time of the spontaneous emission process can be calculated from the cross section as

$$\tau = \frac{c^2}{4\pi^2 \sigma v^2 \Gamma_{\text{res}}} = 20.4(2.1)\,\mu s$$

where c is the speed of light and Γ_{res} = 119.6(2.5) MHz is the observed linewidth without power broadening. The linewidth was acquired scanning the hyperfine transition at low power (≈ 0.1 W) before locking the laser to the correct resonance frequency. Disregarding any other loss channels, the lifetime suggest that a reduction in temperature from 50 K to the Doppler temperature ($\approx 0.17\mu$ K) would require around 8×10^4 photons and could potentially take place in 8 s seconds, an acceptable observation time during experiments.

Chapter 3

Anion trapping

3.1 Electron trapping

Working with negative ions, Penning traps offer the advantage to simultaneously confine anions with electrons that act as a cooling medium. Electrons are easy to produce in large quantity by a hot cathode. The widely accepted method of trapping consists of preparing a possible trapping region and sending a beam of electrons into the region. The electrons collide with each other and with negative ions, transferring energy and momentum while in the magnetic field. They lose kinetic energy by emitting synchrotron radiation as their trajectory revolves around the axial field. Collisions and cooling allow filling the trap region by a current of a few μA within a few seconds.

The electron source of the UNIC experiment is assembled on a mechanical holder that can be inserted into the beam line in front of the Penning trap. In the assembly, a set of two additional cylindrical electrodes allows accelerating and focusing of electrons into the trapping region [55].

Electrons were trapped in several different configurations to test the electrical performance of the trap. The trap was operated with the floating voltage of the high voltage platform equal to ground. We typically trapped electrons up to the space charge limit with typical quantities of $10^9 \ldots 10^{10}$ e$^-$. Trapping was realized up to the longest trap where HV0 and HV1 were used as end caps. The applied voltages were $U_{front} = -100$ V, $U_{center} = 0$ V and $U_{back} = -300$ V). In this long trap, the effect of field misalignment can be better appreciated. It is known that an electron plasma confined in a Penning trap can expand radially as a consequence of collisions with residual gas or misalignment of the electric field with respect to the magnet axis [41]. The expansion of the plasma can quickly lead to a loss of electrons as they enter into contact with the trap walls. To counteract the expansion, a quadrupole rotating electric field (rotating wall) can be applied to the four innermost electrodes to add torque and compress the plasma towards the axis. The rotating field is obtained by applying four sinusoidal potentials with $\pi/2$ phase shift to the four $\pi/2$ geometrically dephased electrodes. The effect and the efficiency of this method can be observed by measuring the lifetime of the electrons in the trap. We extended the electron lifetime well beyond the typical observation times adopted during experiments (> few hours) by applying the correct compensating rotating-wall field (Fig. 3.1).

The motion of particles can also be affected in the axial direction by superimposing an alternating field to one end cap. In the experiment reported in Fig. 3.2, the trap had front, central and back electrodes, labeled 9, 10 and HV1, set to DC voltages of -105 V, 0 V and -600 V respectively. An oscillatory field of amplitude 10 V was superimposed for 10 ms to electrode 9. After the excitation, the content of the trap was observed with the imaging MCP. The experiment was repeated for different values of the end cap driving frequency. The oscillating axial electric field shakes the particles longitudinally inside the trap. Thanks to the field perturbation, ions can gain kinetic energy and escape. The process is particularly efficient if the field frequency meets particle oscillation eigenfrequencies. Thus, resonant peaks appear in the measured number of escaping particles, corresponding to oscillation eigenfrequencies of the axial plasma motion.

Mixing electrons and negative ions in the same trap allows sympathetic cooling of anions by electrons [30]. Since two different particle populations of different masses fill the trap, it is thus important to establish techniques that could separate the extraction signals due to each component. In fact, the number of stored particles might be markedly different between the two species as will be explained in Sec. 3.3. Electrons are easily produced and trapped in large quantities and may constitute a considerable background. If released together with the anions on the detector the signal can cover that induced by the negative ions, thus preventing the optimization of the trapping parameters. Following the suggestion in [50] it is possible to separate the two species with a short pulse applied to one of the two end caps. The pulse was typically applied to the front electrode, equalizing the front and central potential for a short amount of time. As the trap is opened on one side, the particles are free to leave. However, during the pulse, the movement of the heavy ions is much slower due to the mass difference. The duration of the pulse can hence be tuned to strongly reduce the number of electrons while preserving the anions.
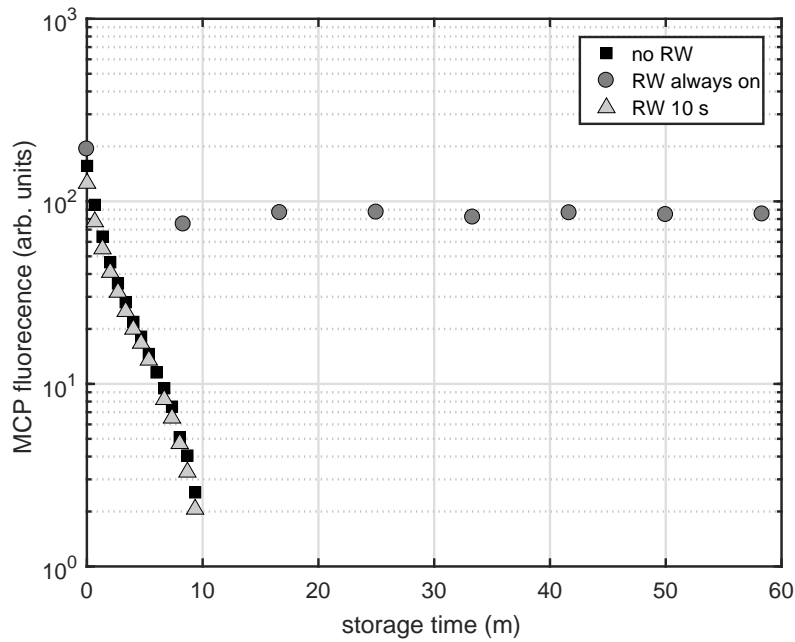
Figure 3.1: Number of remaining electrons as a function of the storage time in the long trap. The measurement shows how a constant rotating-wall drive may extend the lifetime of the trapped electrons by preventing plasma expansion and losses, as described in the text. The applied rotating-wall waveform at 5 MHz had an amplitude of 5 V only for 10 s (*RW 10 s*) or 0.5 V for the entire time (*RW always on*).
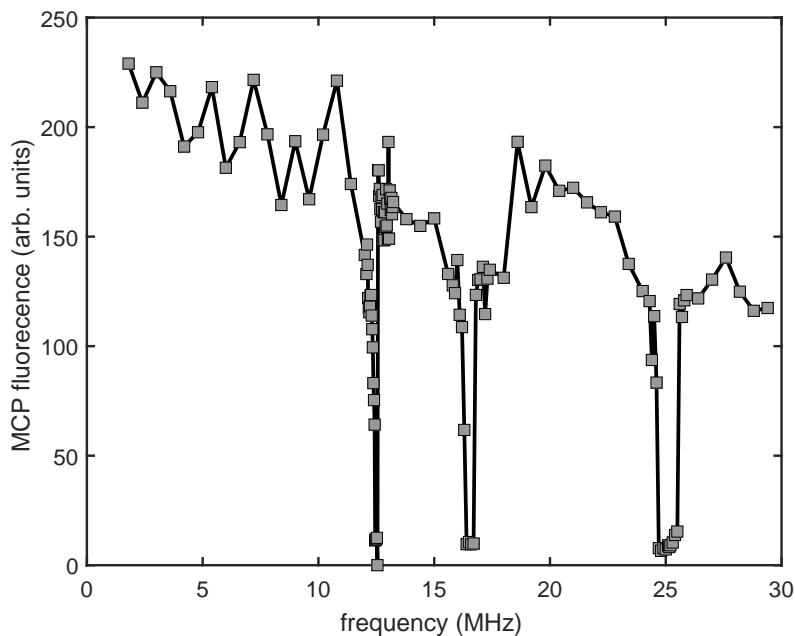

Figure 3.2: Number of remaining electrons as a function of the axial excitation frequency. Some resonances, corresponding to plasma eigenfrequencies, are visible in the spectrum. DC voltages of (−105 V, 0 V, −600 V) were applied respectively to front, center and back trap electrodes labeled 8, 9, 10. An oscillating potential of amplitude 10 V was superimposed to electrode 9 for 10 ms.
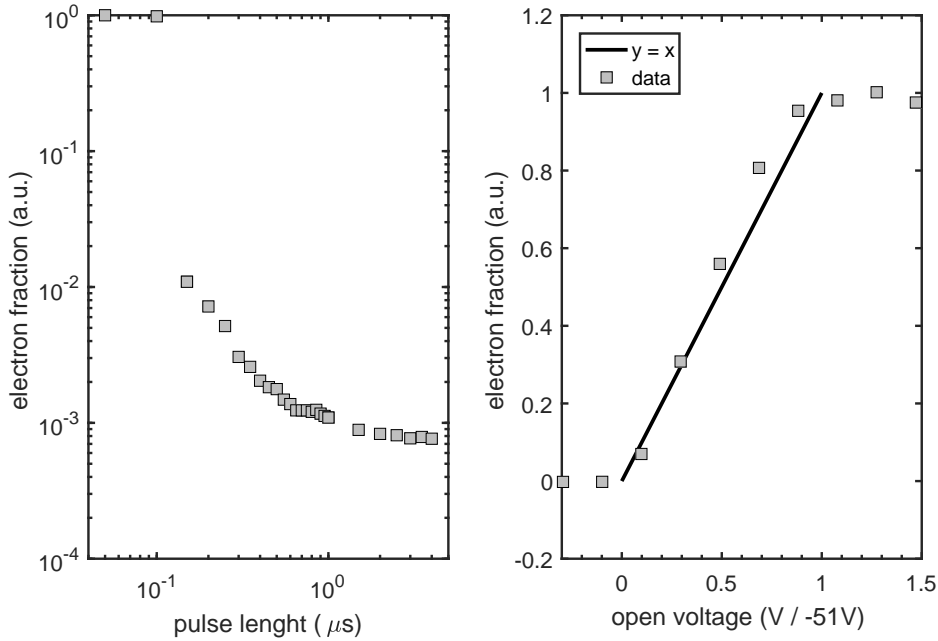
Figure 3.3: Fraction of ejected/detected electrons as a function of the ejection pulse time. The fraction of electrons is measured by taking a reference image of the content of the trap without the pulse. End caps electrodes were made by connecting 0-2 and 8-10 electrodes, while the central connecting 3-7 electrodes. The trap depth was −51 V. Left pane: Fraction of remaining e⁻ in the trap with a pulse of −51 V on the front electrode for different pulse lengths. Right pane: Fraction of ejected electrons as a function of the pulse amplitude with a 1 μs pulse. The pulse amplitude is given normalized to the front potential at trapping (−51 V). The line corresponding to the equation $x = y$ is shown to guide the eye.

The process leaves, unfortunately, the open question of how many negative atomic ions are lost during the pulse while electrons are accelerate outwards. The electrons rapidly exiting the trap may, in fact, can collide with an ion on the way through the slower anions and detach the extra electron. The pulse technique may, therefore, reduce both the background and, unfortunately, the signal to be measured. However, the reduction is drastically different, and the pulse technique proved to be fundamental to suppressing the e⁻ signal by increasing the sensitivity to the number of anions down to single trapped particle. It is therefore reasonable to assume that the number of anions given in our analyses is a lower limit of the real number of trapped particles. This effect of signal suppression is expected to be stronger in measurements with a large amount of electrons involved (Sec. 3.3)[1]. The pulse was always applied before releasing anions towards the MCP to ensure that e⁻ would not affect the acquired signal.

During the axial pulse, electrons are removed much faster than 1 μs (Fig. 3.3). Yet, since the rise and fall times of the pulses was measured to be slightly more than 100 ns, the e⁻ real dynamics could not be fully identified due to this experimental limitation. A pulse of > 300 ns on the front electrode was found sufficient to remove most of the e⁻, and we often used pulses between 300 ns up to 1 μs long. The number of ejected electrons can also be controlled by reducing the amplitude of the pulse to a fraction of the trap depth (Fig. 3.3 right pane).

It was found that the application of the pulse to one end cap heats the electron plasma. The heating caused by the pulse cannot be attributed only to the shape of the potential but also depends on the details of how the shape is switched on. Switching one of the end caps and modifying one side of the trap causes a heating action rather than opening the confinement changing the central potential. In the two cases the potential has a ladder structure that leaves electrons free to escape towards the front side, but even though

---

[1]See appendix Sec. A.6

the shape of the potential appears to be similar, e⁻ exit the trap with a completely different timescale. Surprisingly, when raising the central potential, we could still observe some electrons in the trap after $130\,\mu s$ [2].

To conclude, with this set of measurements we finalized the commissioning of the trap and established a robust procedure to load and manipulate negatively charged particles. We also successfully applied a pulse technique that could be used to separate electrons and anions stored in the same trap. After this preliminary work we started to establish the correct technique for capturing anions without electrons. As we will describe in the next sections, even tough this is actually possible, the best efficiencies are achieved when using electrons as a cooling medium.

---

[2]See appendix Sec. A.5 for further details.

3.2 Anion trapping in the Penning trap

Negative ions are routinely trapped in several experimental sites. In particular, within the cold antimatter community, robust methods have been developed to capture and manipulate antiprotons. A few weeks during the time of this work were spent working with the AEgIS experiment at CERN, in Geneva. At CERN a complex of particle accelerators and decelerators produce and select $\bar{\text{p}}$ which are subsequently delivered to experiments in bunches (10^7 particles) approximately every two minutes at an energy of 5.3 MeV. All state-of-the-art experiments use Penning traps to capture and cool the incoming $\bar{\text{p}}$. Each experiment implements a further deceleration step down to a few keV to achieve trapping with static voltages on the order of 10 kV. A common strategy is to introduce a thin degrader foil in the beamline that antiprotons traverse before entering the trap. The trap is normally preloaded with electrons in preparation for the arrival of the antiproton bunch. The electric shape of the trap has a double (nested) structure. In the main long trap, the electrodes can be typically driven to high voltage near 10 kV. Inside the central region, between the two end caps, a second smaller trap is created, thus generating a further positive potential well of 100 V in the middle with a few electrodes. The $\bar{\text{p}}$ capture starts by loading electrons in the short trap. The long trap is opened towards the front. As soon as the antiprotons bunch enters the trap, the front voltage is quickly lowered, closing the trap axially. The captured $\bar{\text{p}}$ loose energy by interacting with the electrons and many of them are finally confined in the short trap after cooling down. In the strong magnetic field, the e^- dissipate the kinetic energy of the mixed plasma by emitting synchrotron radiation. The process reaches equilibrium at the temperature of the surrounding environment within a few seconds [72], trapping a cold sample of about $10^5 \ldots 10^6$ $\bar{\text{p}}$.

This scheme is not viable with negative ions in place of antiprotons because, in contrast to antiprotons, the internal binding energy of anions is extremely weak. At the energy scale of the antiproton bunch, both electrons and antiprotons appear as indivisible particles and collisions among each other cannot modify their nature. Conversely, the electron affinity in negative ions is in the order of the eV and thus several orders of magnitude lower than the kinetic energy acquired at production. At the energy of few keV, anions are fragile systems and the capture scheme must take into account the possibility that collisions will likely detach electrons. However, $\bar{\text{p}}$ are produced in very low quantity 10^7 per bunch (every two minutes) and, by contrast, the 1-10 pA of La$^-$ current delivered by the sputter source correspond to $10^7 \ldots 10^8$ ions per second. After the degrader foil, the energy spread of the $\bar{\text{p}}$ extends from 0 V to well above the maximum trapping capability (10-20 kV). On the other hand, the energy distribution of the anion beam from the sputter source is in the range of just a few volts.

One of the main contributions of this work was the modification of the established trapping technique popular using electrons to capture negative ions. The energy of the anions is on the order of few keV. The high energy is required for the mass selection process, but must be reduced to prevent collisional detachment of the anions. We first attempted the deceleration by using a pulsed drift tube but, finally, a static solution was preferred. The deceleration was provided by floating the entire trap voltage close to the accelerating potential of the source. Anions entering the trap climb a potential hill, reducing the absolute momentum. In the trapping region, therefore, collisions might still take place but at much lower energy. Compared to a pulsed drift tube, this solution makes all incoming anions available in the capturing process, thus taking full advantage of the continuous current from the source.

The trap is prepared in the following way. The front potential (electrodes 0–2) is set to a few volts below the accelerating potential, whereas the first electrode HV0 is grounded to the rest of the apparatus. Thus, the deceleration region is located between HV0 and the front end cap. The region is well defined and located close to the center of the magnet, such that the beam divergence induced by the deceleration is compensated by the magnetic field confinement in the radial direction. After anions travel past the front electrode, they enter the central region (electrodes 3–7) that is set to a lower voltage to create the confinement. In the end, the back potential (electrodes 8–10) is the lowest and typically set to a voltage ranging from -100 V to -120 V with respect to the central value. This trap configuration is kept

constant and starting from an empty state the trap fills gradually. The particle current can be interrupted by switching the voltage of an electrode behind the mass separating magnet. The time interval during which anions stream into the trap determines the characteristic *loading time* for the process. A typical range of values of the Au^- beam current was between 0.5 nA and a 5 nA.

It might seem surprising that ions can be stopped in a static configuration. Following energy conservation, a single ion should enter the trap, be reflected from the last end cap and travel backward to the entry point. However, a deflection of the trajectory may transfer part of the axial momentum into the radial direction. This may happen due to the conservation of phase space volume during deceleration or as a consequence of a collision in the central region. The reduction of axial momentum provides stable confinement conditions. There are several possible collision mechanisms including anion-anion elastic scattering, anion-anion inelastic scattering (detachment of the extra electron), interaction with the residual gas or three-body processes and, as the trap fills, deflection by the space charge potential (a schematic representation of the process is presented in Fig. 3.4).

We performed measurements varying the front and central potential to find the best conditions for trapping. The result is presented in Fig. 3.5. In the acquisition we sampled different values of the absolute front voltage (which is the *stopping* deceleration potential perceived by the anion beam) and the *trap depth*, defined as the difference between front and central potential. The stopping potential proved to be an effective parameter to be set just a few volts below the accelerating potential. In this way, anions spill into the trapping region and remain trapped if their axial energy is reduced by a few eV. The fact that the optimal stopping potential is just 2 ... 7 V below the beam energy regardless its absolute value proved to be a general behavior. In this condition, the optimal trap depth determining the residual energy of trapped anions ranged in the tens of volts. Two competitive effects come into play. On the one hand, the higher the trap depth, the lower is the relative momentum to be transferred in the radial direction to achieve trapping. Conversely, the larger the final radial speed, the stronger the radial confinement must be to prevent anions from escaping and to preserve a good density. In this model the trap depth has an optimal value that should increase with the magnetic field (Fig. 3.7). We observed an increase of the optimal value of the trap depths from 0.5 T up to more than 3 T. To understand the scales of the process, it is interesting to calculate that if the depth is converted in kinetic energy and the momentum is directed in the angular direction the diameter of the cyclotron motion associated with the corresponding magnetic field is about 1 cm. Thus, the optimal trap depth corresponds to a diameter of the cyclotron motion of about 11 mm, a value close and yet smaller than the electrodes diameter (33 mm).

The anion beam alignment relative to the magnetic and electric fields of the trap proved to be crucial. If the anions enter the trap with a tilt angle from the axis, the net effect of the stopping potential is to deflect the ions excessively sideways onto the electrode structure. Thus, it is fundamental that the precise alignment o fthe incoming ion beam could be adjusted as far upstream as the mass separator. In this way, it was possible to observe particles traveling through the trapping region thanks to the MCP imaging detector. The first step of the alignment method consisted of grounding all electrodes, while leaving the magnetic field active. In this condition, the beam was guided through the trap. Then, the electrode potential was lowered, decelerating the particles in the central region of the magnet. In case the alignment is sufficient, the image of the beam rotates and periodically focuses as the voltage is lowered, due to the longer time of flight spent by the particles in the magnetic field. The beam must remain visible up to the reference voltage being equal to the acceleration voltage. It is important to underline that this condition rarely corresponds to maximizing the ion current reaching the end of the apparatus while no voltage is applied. After the alignment, the trap well can be shaped as desired to collect the particles.

The observation of trapped negative particles in the Penning trap is not a sufficient condition to claim that anions have been trapped. Electrons detached in collisions can fill the trap while the neutral atom is free to leave. The ejection of the trap contents by pulsing the front end cap shows, however, that some particles with much higher mass than e^- are trapped during the loading procedure. As described in Sec. 3.1, the contents of the trap can be released upstream by applying a voltage pulse of variable duration
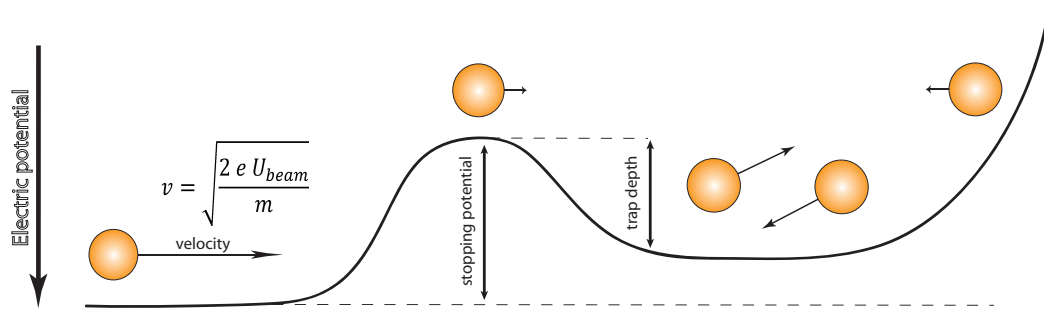
Figure 3.4: Schematic of the trapping principle. Anions approach the trapping region with energy U_{beam} and climb the stopping potential. Momentum transfer into the radial direction in trapping region may lead to stable confinement due to the reduction in the axial velocity component.
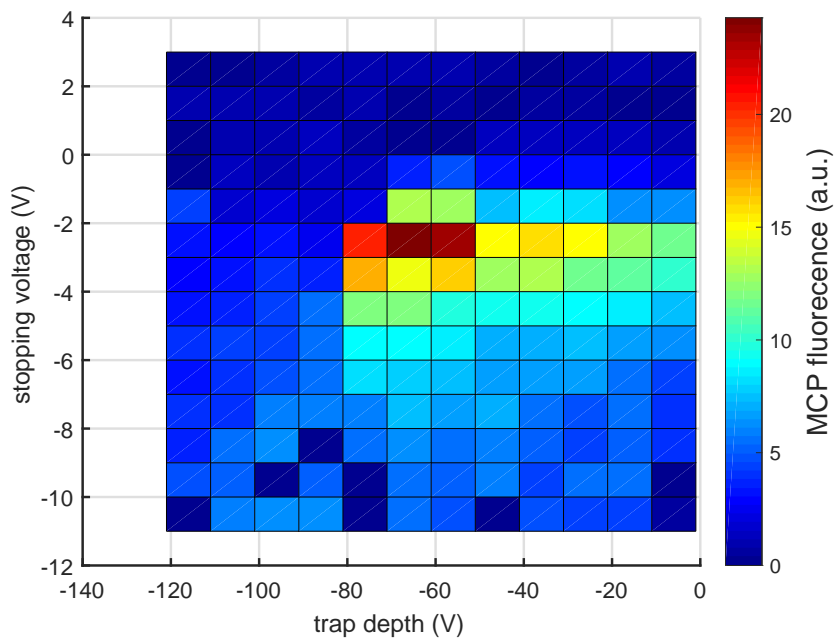

Figure 3.5: Trapping efficiency as function of stopping voltage and trap depth. The stopping voltage is relative to the beam accelerating voltage of −471 V. The magnetic field was 5 T, and anions were loaded for 5 s.

on the front electrode. During the pulse, the front potential is at the same level as the central electrode, and particles are free to leave the region. The measured quantity is thus the time it takes for the particle to leave the trapping volume as the confinement is eliminated. The trap depth was −55 V, the beam energy was 458 eV, and ions were loaded for 20 s. To remove all stored ions, the pulse had to last a few tens of μs, instead of the few hundreds of ns required for electrons (Fig. 3.6). Furthermore, heavy ions are observed only in case the trap is loaded by the described procedure. We observe no anions by this time-of-flight technique if the trap is filled only with electrons and they and are kept confined for a long time (10 min or more). This ensures that the anions are not due to contamination of residual gas and formed by electron capture.

To conclude, the loading process does not directly suffer from the collisional neutralization of negative ions. In fact, electron detachment constitutes just another possible cooling mechanism which does not prevent the trap to fill gradually. Setting the trap electrodes to a deceleration potential almost equal to the acceleration potential is the ideal solution to use all the available anions so that the largest fraction is trapped. The trapping mechanism is effective because at the entrance the momentum of the anions is manly directed on axis but is redistributed in the trap (randomized). This enlarges the phase space of the anion motion reducing the axial energy and providing stable confinement conditions.
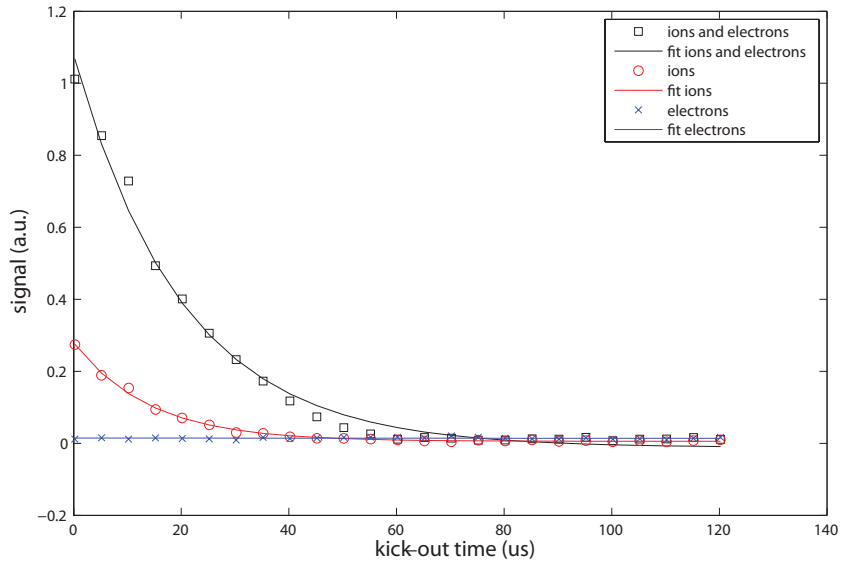
Figure 3.6: Number of anions remaining in the trap as a function of the release pulse time. The data show the presence of a heavy mass component in the trap. The experiment was repeated in the same conditions with electrons only, anions only and loading anions in a trap preloaded with electrons. The pulse time >1 μs required for particles to escape indicates the presence of negative ions heavier than e^- (see Fig. 3.3). The signal is present only if the anion beam was guided through the trap. The exponential fit (solid lines) yields a storage time of 14.0(4) μs. Adapted from [91].
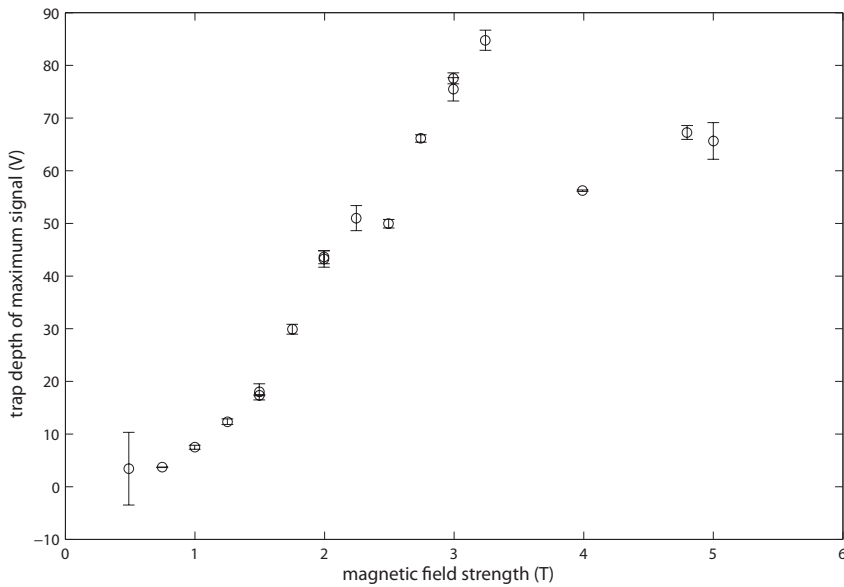
Figure 3.7: Optimal trap depth as a function of the confining magnetic field. Adapted from [91].

3.3 Anion trapping with a e⁻ buffer plasma

The results presented in the previous section shows the underlying mechanisms of ion trapping. If stronger cooling is provided, the process is expected to become more efficient. Like in antiproton trapping, electrons can constitute a buffer medium that can cool negatively charged particles via Coulomb interactions without adversely affecting the vacuum.

To test the loading efficiency in the presence of electrons, the trap was preloaded with electrons (see Sec. 3.1). We calculated that about $10^9 \ldots 10^{10}$ e⁻ could regularly be present. After e⁻ have been confined, the trap potential was set to the deceleration value for anion capture. The measurement of the loading efficiency with respect to the front potential and trap depth shows that the presence of electrons modifies the previous potential values shifting the optimal stopping and trap depth potentials (Fig. 3.8). The best stopping potential was found equal to the beam acceleration energy and not lower than in the absence of electrons. In the measurement, we loaded the trap for 20 s and observed a significant increase (three orders of magnitude) of the final number of anions when electrons were present. The increase is to be attributed to the strong cooling provided by the e⁻ plasma. The incoming anions not only experience a momentum redistribution due to the interaction with other charged particles but also a net kinetic energy reduction which enhances the efficiency of the confinement.

Extending the loading time is necessary for obtaining a denser plasma containing more anions. Loading ions for a time longer than a few seconds may prove useful in a future application and be of primary importance when only weak anion currents are available like in the La⁻ case. However, the innermost cloud of electrons and its field tend to expand, pushing the anions radially away from the trap axis and thus imposing a time limit on the loading process. The expansion was already observed without anions (Fig. 3.1), and it speeds up under the influence of the continuous stream of the incoming beam. The expansion of the plasma reduces the capture efficiency by decreasing the e⁻ density and by dragging anions towards the electrode surface. The rotating wall can be used to add torque to the trapped plasma and counteract this effect, as already presented (Fig. 3.1). Thus, the rotating wall allows extending the loading time, leading to a larger number of anions being trapped. In the measurement presented in Fig. 3.9 we adopted the trap configuration with front, central and back voltages equal to (5 V, 49 V, −100 V) optimizing the floating reference of the trap for optimal load. The current of anions entering the trap was 5(1) nA. During the loading, the rotating wall was kept on with a frequency of 3 MHz and amplitudes depending on the acquisition. As expected, when the correct drive is applied, the shape of the electron cloud can be preserved for longer times, extending the loading time and capturing more anions. Comparing the data with zero RW amplitude with the others, we observe comparable efficiency for slightly more than one minute (at 80 s around 8×10^6 anions are trapped in all conditions) because the expansion has not yet become detrimental for the loading process. Then, under the influence of the correct rotating wall drive, we managed to preserve the radial shape of the e⁻, extending the time for efficient loading. By using an amplitude of 120 mV we trapped up to 2.9×10^7 anions after loading for 160 s, and conversely, the number of anions did not further increase from the initial value of $< 10^7$ without rotating wall even after longer loading times.

Further optimization can be carried out by investigating the effect of a different rotating-wall drive frequency. Moreover the RW induces heating effect that preserves distributed densities of both e⁻ and anions in the trap volume. As we will see in the next section, if the system is allowed to evolve freely, centrifugal separation of the two species sets in as the system thermalizes to the temperature of the surrounding environment (a few tens of kelvin) thanks to the emission of synchrotron radiation by the electrons.
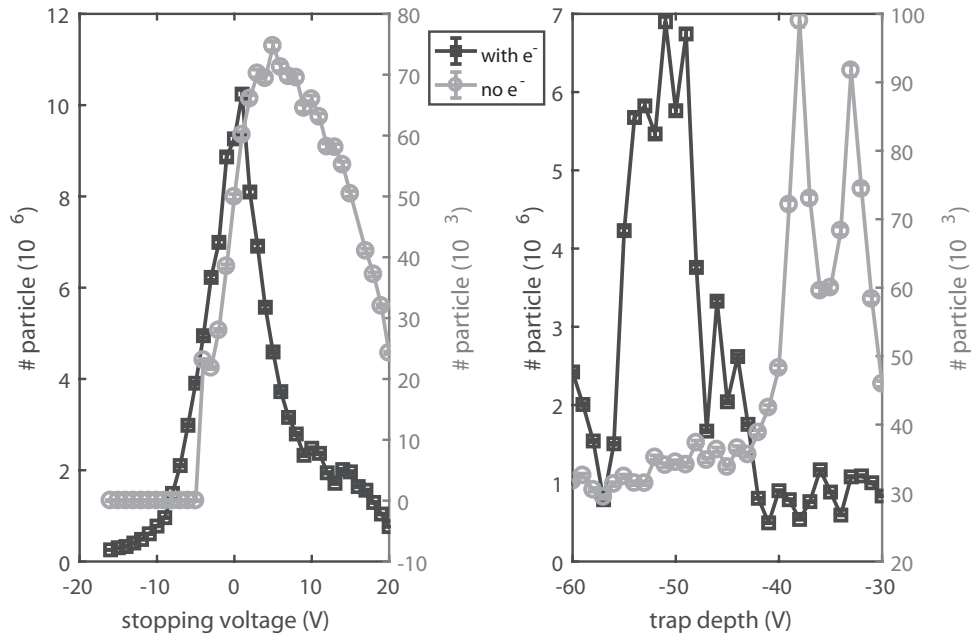
Figure 3.8: Number of anions trapped as a function of the stopping voltage (left) and trap depth (right). Ions were loaded for 20 s at a beam energy of 1006 eV with and without electrons. Data acquired with and without electrons are compared in the plots. Data acquired with no e⁻ pre-loaded in the trap have the scale on the right side of the plots. The lines are meant to guide the eye. Left Pane: Stopping voltage is relative to the anion beam energy. Front, central and back potentials were 5 V, 56 V and −100 V for acquisition with electrons and 5 V, 44 V, −100 V for data acquired without electrons. Right Pane: Influence of the trap depth on the trapping efficiency. Floating, front, back potentials were −1008 V, 5 V, −100 V respectively.
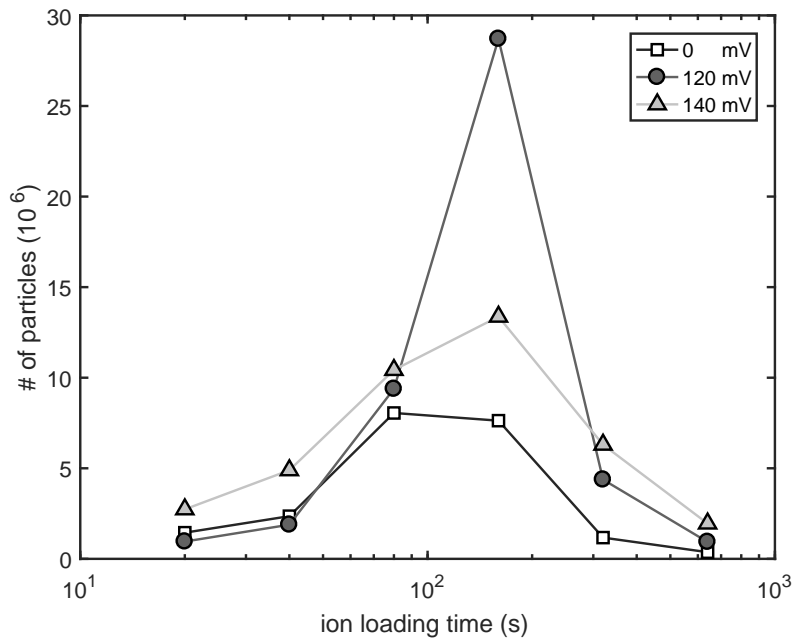
Figure 3.9: Number of anions as a function of loading time. If electron are kept compressed using the rotating wall excitation the loading can last longer, increasing the total number of captured anions. The rotating-wall frequency was 3 MHz with the peak to peak amplitude specified in the legend. The lines are meant to guide the eye.

3.4 Sympathetic cooling of anions by e⁻

Electrons confined in a Penning trap radiate away excess energy by emitting synchrotron radiation. The radiation is emitted because e⁻ are light charged particles subject to a centripetal acceleration induced by the strong magnetic field that curves their trajectory in confined orbits (cyclotron motion). The e⁻ thermalize with the surrounding environment and may be used to cool a second species which populates the same trapping region. When heavier anions are introduced into the trap, they will occupy the same volume and exchange momentum with the electrons via Coulomb repulsion. The presence of e⁻ in the trap can therefore not only favor anion capture but is a pre-cooling step before laser cooling.

When the average kinetic energy becomes sufficiently low, the two species tend to occupy different regions of the trap due to their mass difference. At low temperature, the heavier species will migrate away from the trap axis in favor of the lighter ions. With a box-shaped electric potential (as in our case), the problem can be treated in the plane orthogonal to the magnetic field by assuming a uniform geometry of the plasma along the axis. In such conditions, a dense thermal plasma rotates inside the trap as a rigid rotor if the energy spread is limited. The rotation frequency for each species differs from one another for a plasma column that has not yet come to thermal equilibrium. Since each species rotates at a different angular frequency there is a collisional drag and the resulting drag force F (in the angular direction) produces a $F \times B$ drift in the radial direction that causes *centrifugal separation* between species [7]. In our system, the anions will hence leave the inner axial region occupied by the electrons.

We investigated this separation in our system with a dedicated experiment in order to understand the rates of cooling processes for heavy anions and electrons and the temperature limit temperature for anions achievable in our system. At first, we loaded the electrons with a trap depth of 60 V in a 5 T magnetic field[3]. 25 s after the e⁻ loading, the trap depth was reduced to 51 V to remove some excess electrons. This stabilizes the number of loaded electrons which might be affected by possible fluctuation in the yield of the electron gun. Our estimate on the space charge limit imposed by the trap geometry indicates that 6×10^9 electrons were trapped. The direct measurement with the MCP image gives a number of e⁻ fluctuating in the range $2.2 \ldots 2.4 \times 10^9$. Then, the trap already containing electrons was loaded with Au⁻ for a short time (5 s) without the use of rotating-wall excitation, capturing about 10^6 anions[4]. The large difference in number (three orders of magnitude) leads us to conclude that the plasma properties and the charge space potential are mainly determined by electrons. After electron and ion capture, the system was left to evolve freely, and the distributions of anions and electrons (mixed with anions) were reordered separately for different storage times at intervals of 25 s.

In the beginning, the system is at high temperature due to the heating effect of the anion beam entering the trap. Only after a few minutes centrifugal separation of anions from electrons is observed. We can consider this process as a phase transition that occurs due to the cooling. To identify the evolution of the phase transition, we calculated the *hollowness* of the acquired anion images as a function of time. The hollowness H is defined as [72]

$$H = \left\langle r^2 \right\rangle^{1/2} \cdot \left\langle r^4 \right\rangle^{-1/4} \quad , \tag{3.1}$$

where the angle brackets denote the average over the radial profile. The hollowness expresses the properties of the plasma distribution by analyzing the relative density from the trap axis, yet is insensitive to the real dimension. The value is $H = 0.841$ for a Gaussian profile, $H = 0.915$ for a constant density ellipsoid, and $H = 1$ for a thin annulus. The phase transition can be identified as a transition in the value of the hollowness from the two limiting cases when the anions are still mixed in the center with electrons ($H \approx 0.7$) to the condition when their projection on the MCP assumes the final annular form ($H \approx 0.95$). The separation takes place after storing the ions for about four minutes (Fig. 3.12). Even well after separation (about 350 s), the anion expansion does not stop, and the average orbit radius increases faster

---

[3]The central electrode was realized by shorting electrodes from 3 to 7 and therefore resulting in a 64 mm long trapping region.

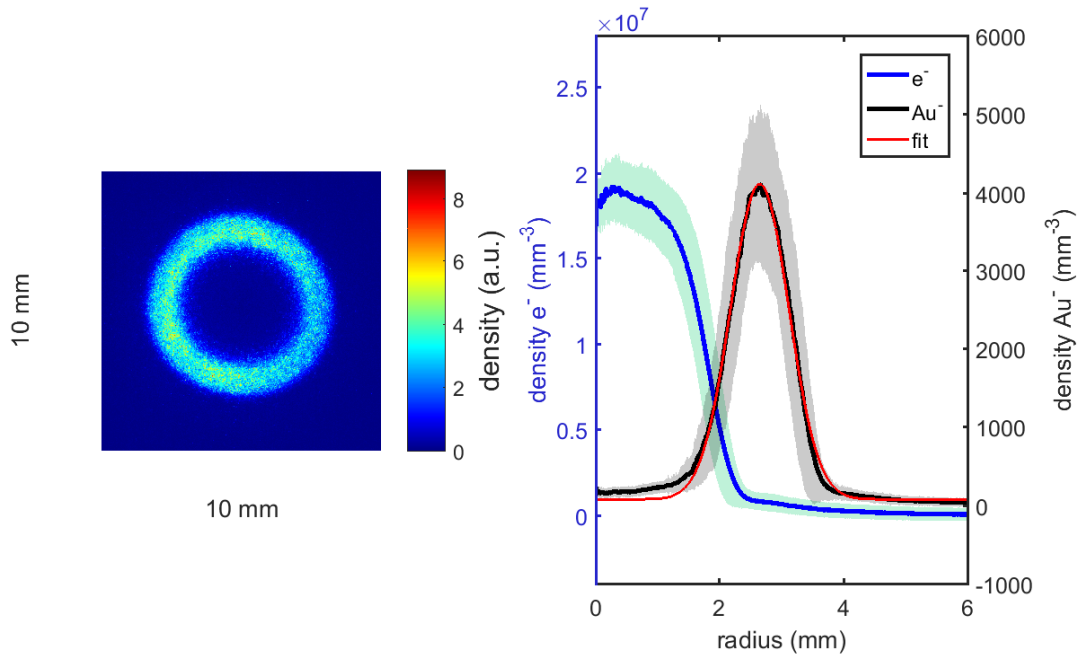[4]More precise data are available in the appendix in Sec. A.6.

Figure 3.10: Left pane: Camera image of anions on the MCP after 351 s. Right pane: Radial density of the anions and the corresponding nearest available measurement of e⁻ at 361 s. The shaded area corresponds to the standard deviation of the profile. The red line is the fit of the anion distribution following the Boltzmann distribution, as described in the text.
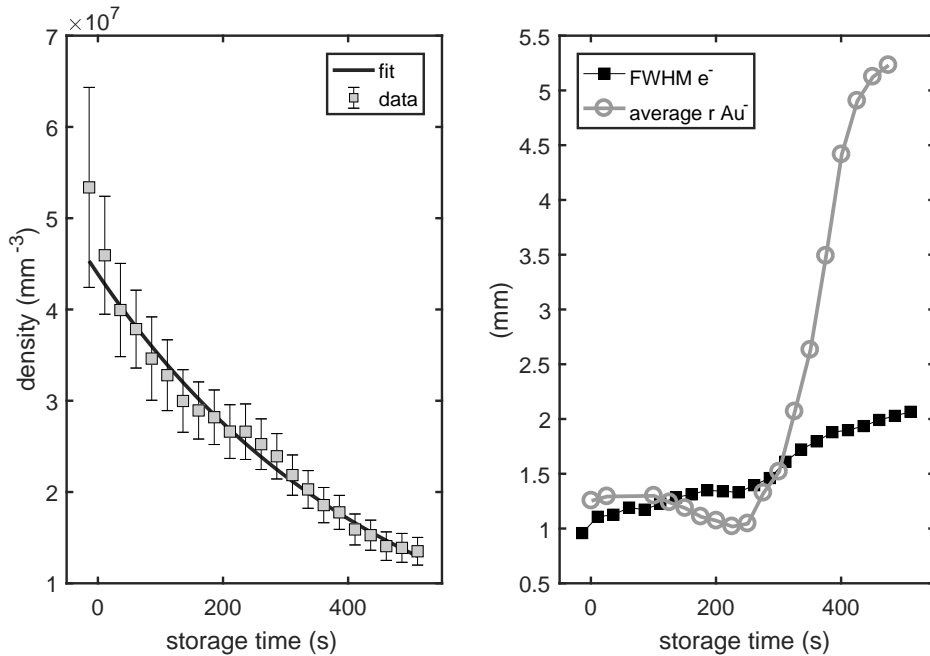

Figure 3.11: Left pane: On-axis density of the electron plasma as a function of the storage time. The exponential fit $n_0 \exp(t/\tau) + n_{inf}$ gives $n_0 = 4.56(38)10^7$ mm^{-3}, $\tau = 4.52(85)10^2$ s, $n_{inf} = -2(5)10^6$ mm^{-3}. Right pane: Dimension of the plasma are reported. As dimension of the e⁻ we report the the radius where the e⁻ reaches half of the on-axis value. As dimension of Au⁻ the average of the radial position is used. The solid lines are meant to guide the eye.
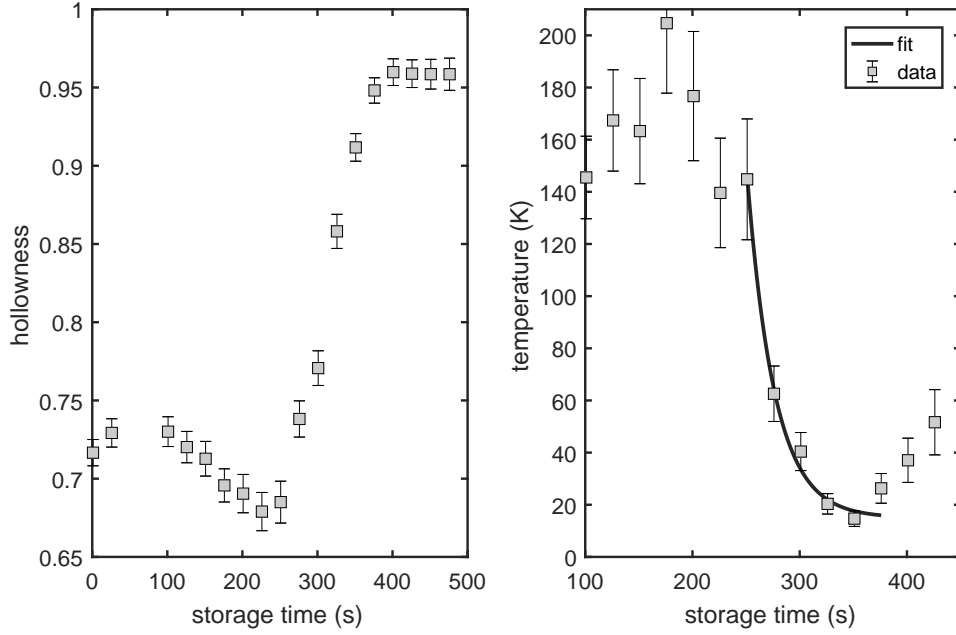
Figure 3.12: Hollowness (Eq. 3.1) and temperature evolution as a function of storage time. Left pane: Hollowness calculated as described in the text. The phase transition of centrifugal separation is evident around 300 s. Right pane: Calculated temperature of the anions during the transition. The solid line is an exponential fit $T_0 \exp(t/\tau) + T_{inf}$ to the data with parameters $T_0 = 2(9)10^6$ K, $\tau = 25.5(9.0)$ s, $T_{inf} = 15(6)$ K.

than the expansion rate of the e$^-$ plasma, which loses contact with the cooling medium. Anions are lost within 500 s total storage time (Fig. 3.11).

In thermal equilibrium at temperature T the probability distribution for an ion species of charge q_a, mass m_a, rotating wit angular frequency ω_r follows the Boltzmann distribution [87]:

$$p \propto \exp\left(\frac{q_a}{k_B T}\left(\phi(r) - \frac{m_a}{q_a}\frac{\omega_r^2 r^2}{2} - \frac{B\omega_r r^2}{2}\right)\right) \quad , \tag{3.2}$$

where r is the distance from the center and k_B the Boltzmann constant. The energy is composed of three terms: the first is the electric potential $q_a\phi(r)$ due to the space charge, the second is the kinetic energy due to the velocity $m_a\omega_r^2 r^2/2$, and the last term containing B stems from the canonical momentum with the vector potential $q_a B\omega_r r^2/2$. The electron distribution is, in general, similar to the one shown in Fig. 3.10 and we will make the approximation that it is uniform as a function of the radius. In this approximation the plasma edge is sharp, and the electric potential ϕ is proportional to r. The velocity of the plasma is approximated as the rigid rotation of particles in the form of a column rotating at the constant angular velocity given by [78]:

$$\omega_r \approx \frac{2\pi q c n_0}{B} \quad ,$$

where n_0 is the plasma density. We assumed n_0 as the density of the e$^-$ data near the axis. In the absence of e$^-$ and anions projections for equal storage time, the density of the e$^-$ was calculated where needed from the exponential fit of the data (Fig. 3.11).

The model allows fitting using Eq. 3.2 to the radial distribution of the anions in order to extract a temperature value (Fig. 3.12). We performed this fit to the data taken during the phase transition ($250\,\text{s} < t < 380\,\text{s}$). The analysis suggests that the anions are cooled to a limiting temperature comparable to the temperature of the trap electrodes within the timescale of half a minute.

Our measurement is compatible with similar experiments [30] and shows that anions can be pre-cooled in the magnetic field using electrons. The electrons can, therefore, be used to start the laser cooling at the reduced temperature of a few kelvin, thus reducing the number of photons required to reach the Doppler limit. In fact, starting from the temperature of 300 K the cooling of La$^-$ to the Doppler temperature ($\approx 0.17\mu$ K) would require 2×10^5 photons, but only 5×10^4 would be needed if the initial temperature is reduced to 20 K.

3.5 Anion trapping in the Paul trap

As described in the previous sections (3.2 and 3.3), negative ions can be trapped inside the Penning trap from a continuous beam (Ch. 3). It has been shown how to prepare the trapping volume in suitable conditions before initiating the filling process. Based on experience gathered by working with the Penning trap, we achieved trapping of anions in similar conditions with the Paul trap. Trapping was realized by streaming the anions continuously into a region floated to a high decelerating voltage. There are important distinctions in the type of radial confinement and the geometry of the electrodes that result in some differences between the loading processes in the two traps.

The beam of Au⁻ (kiteic energy 1006 eV) was directed towards the trap region, where three electrodes called *front*, *center* and *back* define the trapping region. The central DC potential is applied on the rods while front and back voltages are applied to the first and last fast switching electrodes. Please note that, as in the case of the Penning trap, the power supplies that generate the voltage levels are mounted on a high-voltage platform (rated up to 5 kV) at a common *floating* reference. This voltage can, therefore, be set to modify the potential energy of the stored ions with respect to the surrounding potential, which is the reference ground of the external vacuum chamber. In order to facilitate discussion, we introduce the *storage potential*, which is the sum of center plus the floating potentials, and *stopping* or *decelerating* potential which is the sum of front and the floating potential[5]. At load time the ion current is switched on by modifying a deflection potential before the mass spectrometer, and the ions enter the trap while the system is kept in steady conditions for a definite amount of time[6]. The trap gradually fills with anions during the loading time. The captured ions are then detected by switching the back potential and releasing the content onto an MCP with a phosphor screen biased to $U_{MCP} = 200$ V with respect to ground. The MCP potential accelerates the cloud of ions, which is projected on the detector. The total energy of the anions impinging on the detector is, therefore, U_{MCP} plus the storage potential. The alignment procedure to introduce the beam into the Paul trap was found easier than in the experiments with the Penning trap. In the Penning trap, the alignment procedure aims to match the correct direction rather than just maximizing the transmitted anion current (see Sec. 3.2). However, once suitable conditions are found, the magnetic field provides a focusing effect which extends far away from the trapping region, thus preventing small instabilities in the beamline from affecting the capture efficiency. Conversely, in the Paul trap, the best configuration was found by guiding as many anions as possible into the trap, yet we observed that the fluctuations in the beam alignment can affect the efficiency of the loading process.

After ion capture the trap reference potential is brought to a few hundred volts below the MCP potential, and the back electrode potential is switched to eject the trapped ions towards the MCP for detection. The ion cloud, hitting to the MCP entrance channels, causes secondary-electron emission in an area whose diameter depends on the accelerating potential from the back trap electrode to the MCP potential. The profile of the projection of the cloud on the MCP entrance plate can be modeled with a Gaussian distribution in line with the harmonic approximation of the radial potential (Fig. 3.14). The connection between the harmonic potential and the Gaussian approximation comes from the Boltzmann distribution, which implies that the probability p of finding a particle with velocity v within a certain distance r in the radial plane is given by

$$p \propto \exp\left(-\frac{1}{k_B T}\left(\frac{mv^2}{2} + \frac{m\omega_r^2 r^2}{2}\right)\right), \tag{3.3}$$

where ω_r is the radial frequency of the harmonic trap, k_B is the Boltzmann constant, T the temperature and m the mass of the anion. During the flight toward the detector, the cloud expands in the region between the MCP and the grounded rear plate where the radiofrequency is not present. Therefore, we observed that the dimension of the cloud projection depended on the storage voltage. Smaller radial

---

[5]see Sec. 1.5

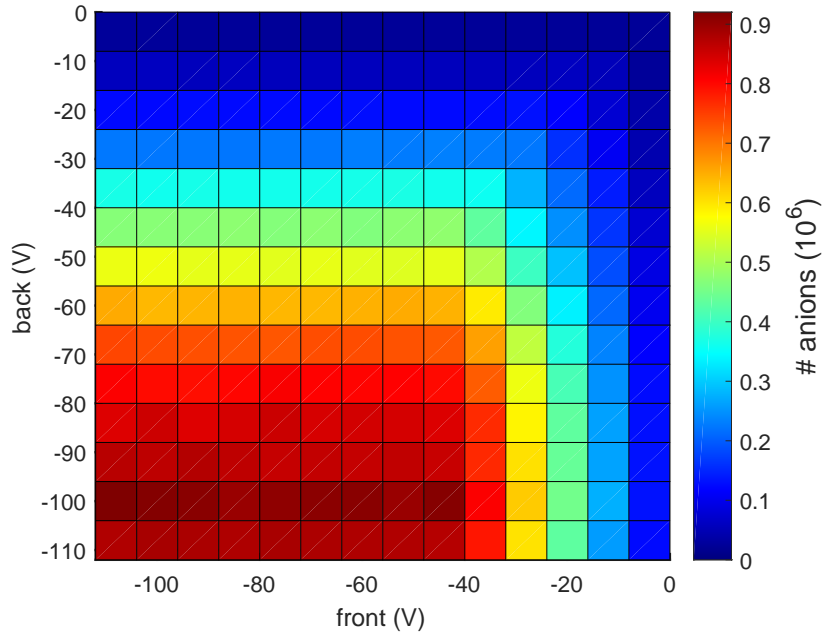[6]an overview of the experiment is presented in Fig. 1.1

Figure 3.13: Trapping efficiency as a function of front and back potentials. During the experiment the center potentials was -795 V and the loading time 10 s. Front and back potentials are relative to the central voltage. The asymmetry in the measurement indicates that a back potential more confining than the front one leads to a higher trapping efficiency.
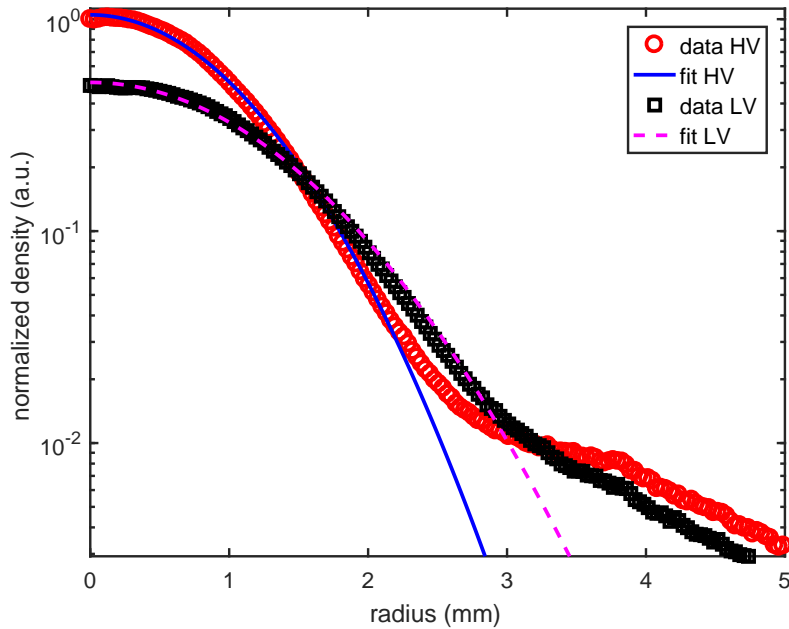

Figure 3.14: Radial profiles of ion clouds acquired by dumping anions from different storage potential after 100 s storage time. Ions were loaded in HV configuration and projected onto the detector either in HV or in LV configuration. Voltages applied were: (Front, center, back) = $x+(-50, 0, -60)$ V with $x_{HV} = -795$ V and $x_{LV} = -205$ V with x indicating the floating potential of the trap. The fit lines are Gaussian profiles of the expression $a \exp\left(-r^2/w^2\right)$. The fit yielded $a_{HV} = 358.7(4)$ $w_{HV} = 1.172(2)$ mm and $a_{LV} = 172.1(2)$ $w_{LV} = 1.521(2)$ mm.

sizes are observed for higher storage potentials because the time of flight toward the MCP. From lower potential negative ions gain more forward momentum and have less time to expand in the radial plane. To favor trapping, the back voltage should be higher than the front voltage to allow for efficient reflection on the last end cap (Fig. 3.13). In contrast to the behavior of the Penning trap, the decelerating trap voltage of the Paul trap was found less critical. While the decelerating potential (floating + front) was in the range of a few volts for the Penning trap relative to the ion energy, in the Paul trap case it was found in the range of a few hundreds of volts realtive to the incoming ion energy (see Fig. 3.5 and Fig. 3.15). We attributed this behavior to the different geometry of the end caps. First, the voltage in the center induced by the end caps is suppressed by a factor 0.18 due to the presence of the rods. Second, the long end caps of the Penning trap generate a more homogenous decelerating field compared to the electrode geometry of the Paul trap switching electrodes (see Sec. 1.7). We observed an increased trapping efficiency for stronger radial confinement. Several acquisitions, such as Fig.3.15, were made with different amplitudes of the RF field. The effect of stronger radial confinement on the trapping efficiency is directly visible by comparing the highest number achieved as a function of the RF amplitude (Fig.3.16).

In the Paul trap, a detailed study of the loading technique can be carried out without lighter contaminants, such as e^-. The loading process can be described by a bounded growth law of the number of trapped particle n. The process is influenced from one side by the rate n'_c of newly trapped particles against the rate of particle lost from the trap n'_l. The number n'_c depends on the beam current I. Conversely, the latter rate can be attributed to the space charge limit and the heating effect of the beam passing through the trap that is that induce losses by evaporation of the hottest particle or electron detachment. The variation in the number of stored particle is therefore in equilibrium between these two effects. The process can be modeled by the following differential equations:

$$
\begin{cases}
n' = n'_c - n'_l \\
n'_c = \alpha I^\beta \\
n'_l = \frac{1}{\tau} n(t)
\end{cases}
,
$$

where α, β and τ are constants. The solution is

$$
n = n_0 \left(1 - \exp\left(-\frac{t}{\tau} \right) \right) , \tag{3.4}
$$

where t is the loading time and $n_0 = \alpha \tau I^\beta$ is the trap capacity. Experimental results were found to be in agreement with the model (Fig. 3.17). The trap capacity n_0 was found to be of about 10^7 anions.

We tested the model to understand how the trapping efficiency is affected by the ion current generating the collisions. In general, we detect a higher number of stored anions if more current enters the trap. The measurement was performed by acquiring several loading time curves at different beam currents. In the acquisitions, the current of ions during loading was modified by a defocusing einzel lens located a few tens of cm before the trap. The current was varied in an interval from few pA to few nA. The loading process was studied from 1 s to 64 s for each current values. Care was taken to ensure the stability of the beam alignment during the acquisition by testing the relation between the defocusing voltage and the current intensity before and after the measurement sequence.

For short time scales, the expression of Eq. (3.4) of the stored particle may be linearized, yielding

$$
n \approx \alpha I^\beta t . \tag{3.5}
$$

Therefore the number of particles was found proportional to the loading time. We fitted the loading data of each different current with power laws in time, obtaining an exponent of 0.90(1). Combining the curves to fit only the current contribution $n^* = \alpha I^\beta$, an exponent of $\beta = 0.75(1)$ was measured (Fig. 3.18). The result indicates that the higher the current, the more efficient the loading results. The suggested loading model was found valid from the lowest adopted current of a few pA up to $0.4 \ldots 0.5\,\text{nA}$
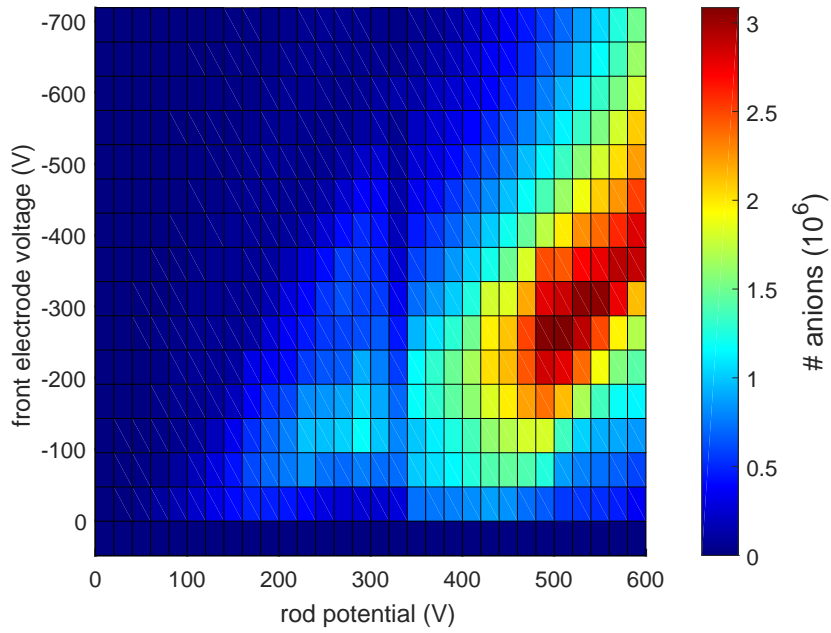
Figure 3.15: Trapping efficiency as function of storage and front potentials. The storage voltage was referenced to the beam kinetic energy. Anions were loaded for 20 s with with $Vpp = 1.55$ kV, the back voltage was -900 V relative to the rods' voltage.
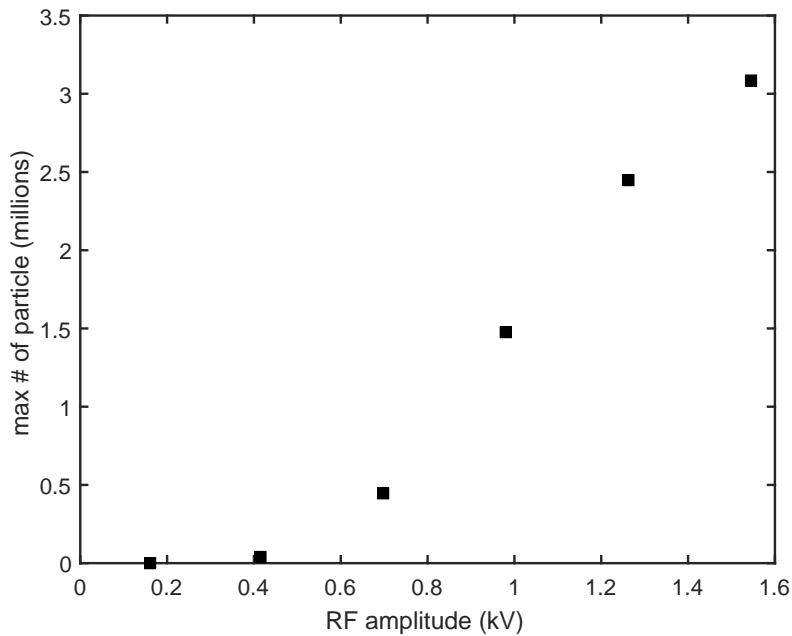

Figure 3.16: Maximum trapped particle number as a function of the RF amplitude. Experimental condition are reported in Fig. 3.15. The experiment was repeated several times for different V_{pp} and in this plot we show only the maximum values of each measurement.
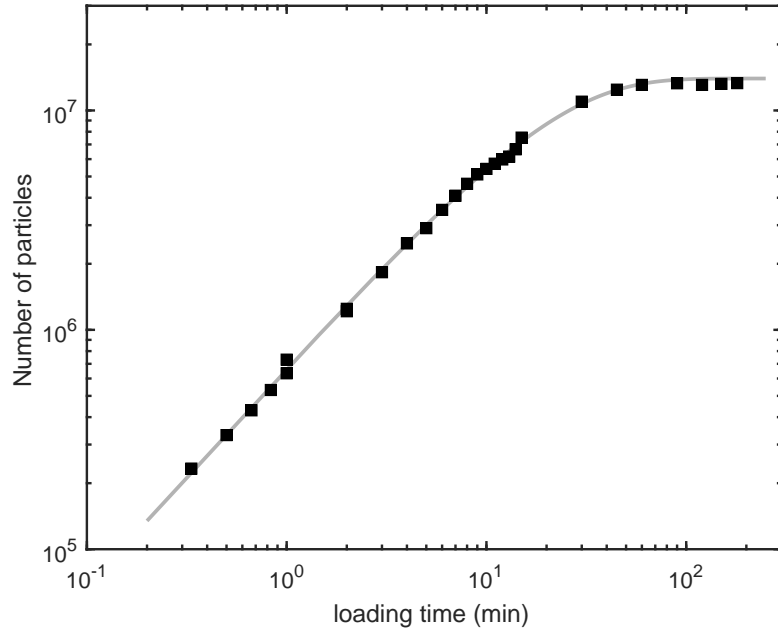
Figure 3.17: Number of trapped anions as a function of the loading time. The solid line is a fit according to Eq. (3.4) with the fit result $n_0 = 1.40(2)10^7$ and $\tau = 20.7(4)$ s. The anion current in front of the trap was several nA. Front, central, back and floating potentials were -45 V, 0 V, -500 V and -850 V respectively. The beam energy was 1006 eV. Adapted from [95]
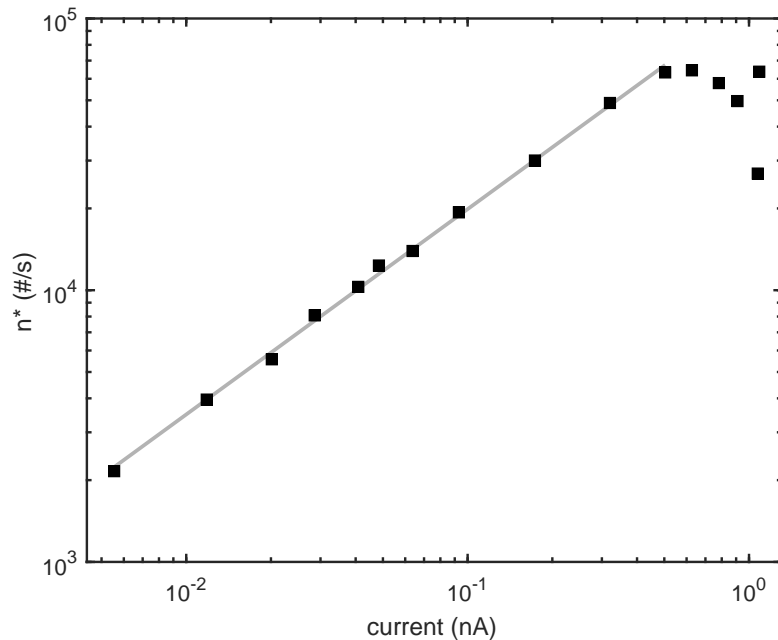
Figure 3.18: Loading ions for different currents. In the plot the solid line is a fit coefficient α of Eq. 3.5. The fitted power law in the first part $n^* = \alpha I^\beta$ with $\alpha = 113(4)10^3/s$ and $\beta = 0.75(1)$. Front, central, back and floating potentials were -50 V, 0 V, -50 V and -795 V respectively. The loading time was varied between 1 s and 64 s.
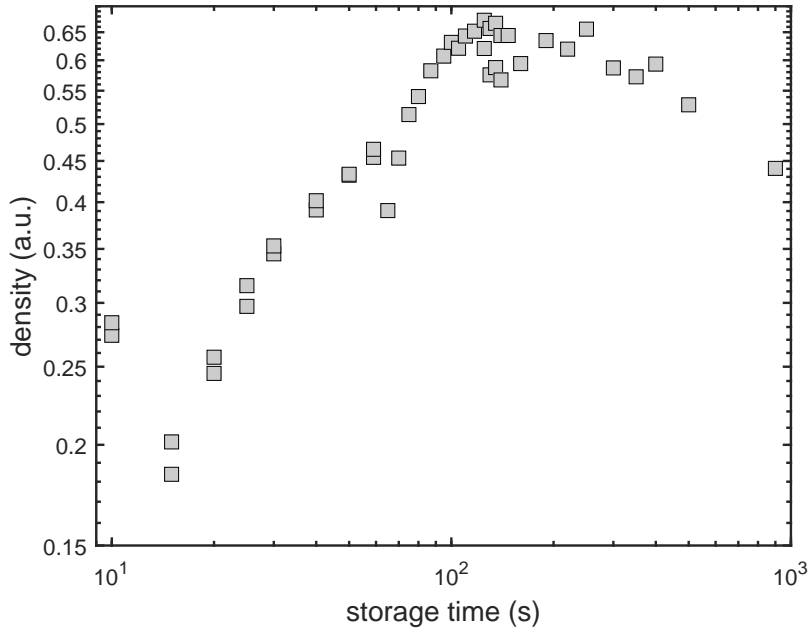
Figure 3.19: Density of anions on the axis of the Paul trap as function of time. As the storage time elapses the particle plasma cools down, resulting in a higher density of particles in the middle of the trap.

and must probably be revised for higher currents where the heating effect of the beam is likely to play a larger role. The presence of an efficiency maximum goes beyond a simple correlation with the incoming current.

An advantage of the linear Paul trap is the continuous radial pressure towards the center that is constituted by the radial confinement. This pressure favors the compression of the anions towards the central region of the trap while cooling takes place. Cooling can be attributed to an evaporating process of the hottest anions leaving the trap as well as collisions with the residual gas present in the vacuum chamber. We observed in our system, with a vacuum of a few 10^{-11} mbar, a temperature reduction of the trapped particles at a time scale of about one minute after loading anions. Cooling was observed by the dynamics of the ion cloud during the initial trapping phase. As the heating process due to the interaction with the ion beam is turned off, anions thermalize at a lower temperature. In the first minutes, the longer the storage time, the more compressed the images of the projected plasma on the MCP appears; indicating a reduction of the phase space of the trapped sample. The cooling process was observed by considering the dumped ion density, fitting a Gaussian to the radial profile and extracting the on-axis density in the bi-dimensional projection. The number of particles on axis increases with time, and this fact must be attributed to cooling taking place, as follows from Eq. 3.3. The result is shown in Fig. 3.19. A more detailed analysis indicates that in our experimental conditions anions reduce their average temperature from 2×10^4 K to 5×10^3 K with a time constant of 40 s [95].

Chapter 4

Discussion

4.1 Cooling scheme for the $^3F_2 \longleftrightarrow {}^3D_1$ transition in La⁻

The Doppler cooling of an atom involves the resonant absorption of light whose photons transfer their momentum to the atom. Thus, the photon frequency should be lower than the resonant frequency (red-shifted), allowing it to be resonant if the atom moves moves toward the photon. The operation requires a monochromatic light source to match the specific velocity of moving particles as well as sufficient power to obtain efficient excitation. Cooling with light is therefore convenient with lasers. If the system has only one ground and one excited level, then a single corresponding transition frequency is needed. Unfortunately in the La⁻ case, the laser cooling transition $^3F_2 \longleftrightarrow {}^3D_1$ splits due to the nuclear spin ($I = 7/2$) of the only stable isotope ^{139}La. The splitting leads to the existence of multiple sub-states and dark states. The level scheme can be extracted from the results reported in Ch. 2 and is shown in Fig. 4.1. The magnetic moment of the nucleus produces five non-degenerate levels in the ground state and three in the excited state identifiable by the total angular momentum quantum number F.

To close the cycle, three laser frequencies are required. The pumping strategy is focused on driving the dipole-allowed transitions towards the excited state $^3D_1$ with $F = 9/2$ (see colored lines in Fig. 4.1). The allowed transitions can be identified by the angular momentum selection rule $\Delta F = 0, \pm 1$. The rule implies that spontaneous emission will populate the ground state levels with $F = 7/2$, $F = 9/2$ and $F = 11/2$. Each of them will require a frequency to be re-pumped. This choice has the advantage, compared to other excited state levels, of providing a strategy to manipulate the entire La⁻ atoms in the five ground states, including the states where $F = 3/2$ and $F = 5/2$. In fact, all $\Delta F = +1$ transitions (red in Fig. 4.1) are very close in frequency as follows from the result of the spectroscopy experiment. In our observation, these transitions group together in the hyperfine peak 7 at the highest frequency. Therefore, while pumping the $F = 7/2 \longleftrightarrow 9/2$ transition, anions with $F = 5/2$ and $F = 3/2$ are also pumped to higher F values. The energy splitting reconstructed using the positions of all peaks indicates a maximum frequency difference among the $\Delta F = +1$ peaks of about 30 MHz. Since the natural linewidth is a few tens of kHz, the $\Delta F = +1$ peaks are expected to be well separated at low temperature (< 25 K). Consequently, some further developments might become necessary when such a low temperature is reached to reinforce the participation of all La⁻ in the cooling process. In particular, periodically chirping of the laser frequency may be a solution to pump anions towards the states with high F.

4.2 The La⁻ level structure

We collaborated with the theoretical group of M. Safranova (University of Delaware) to determine further crucial information about the structure of La⁻ and its cooling cycle. A new theoretical approach was used to compute the La⁻ energy levels, structure, decay branching ratios from the excited state of the cooling transition and relaxation times of the system. The complex electronic structure of the lanthanides (with large electronic correlations) presents major obstacles in calculating La⁻ properties. The best prior calculation of bound states [60], even though useful to identify measured lines of La⁻ spectra [82], deviates from measured excitation energies up to 33% and was improved to 2% by the new calculations. The lifetime $\tau_{\text{theo}} = 22.1(9)$ μs determined from the theoretical studies agrees with the results presented in Sec. 2.6 of $\tau_{\text{exp}} = 20.4(2.1)$ μs. The experimental and theoretical values can be directly compared because in the absence of other allowed decays, the measured $11/2 \longrightarrow 9/2$ transition rate is equal to the total decay rate from the excited state. Taking into account the respective uncertainties, the experimental and the theoretical values are in excellent agreement.

The determined transition rates and calculated branching ratios are crucial for the implementation of the cooling cycle. The laser cooling transition rate is $A_r \approx 4.5 \ldots 4.9 \times 10^4$ s^{-1}, about 50% larger than the previous prediction [69]. The laser-cooled ensemble could thus reach the Doppler temperature $T_D = 0.17$ μK (or the equilibrium temperature in case of competing heating processes) faster than
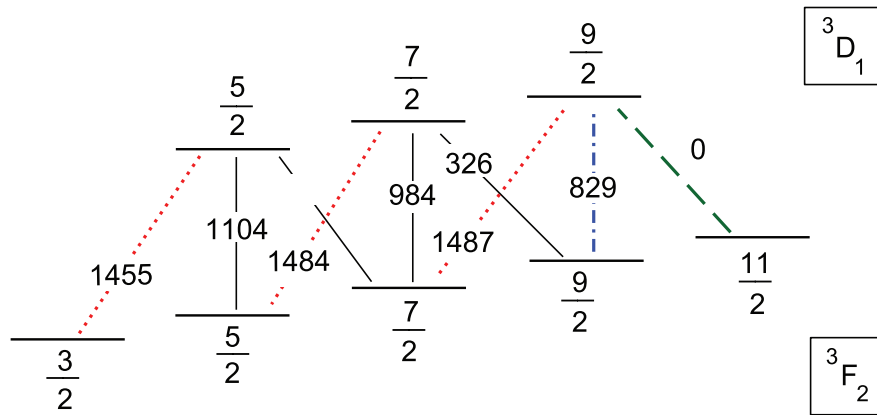
Figure 4.1: Laser cooling transition in La⁻. In the picture the hyperfine levels are indicated by their respective *F* total angular momentum quantum number. The number on the line connecting the states indicates the transition frequency in MHz relative to $11/2 \longleftrightarrow 9/2$. The colored lines (red, green, blue) indicate different laser frequencies for laser cooling and repumping.
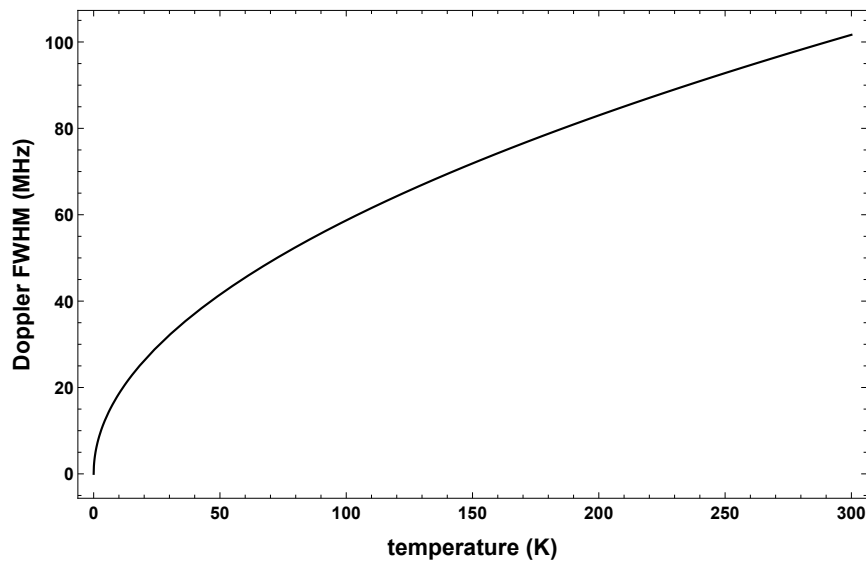

Figure 4.2: Doppler broadening of the transition lines for La⁻ as a function of temperature.

Table 4.1: Transition rates A_r, branching ratios, and lifetimes τ of transitions in La$^-$ calculated using the CI+all method. Numbers in brackets represent powers of 10.

Upper level		Lower level		A_r (s^{-1})	Branching ratio	τ
$6s^2 5d6p$	$^3D_1$	$6s^2 5d^2$	$^3F_2$	4.54[+4]	0.999974	22.1 μs
		$6s^2 5d^2$	$^1D_2$	1.18[0]	0.000026	
$6s^2 5d^2$	$^1D_2$	$6s^2 5d6p$	$^1D_2$	1.95[0]	0.956	489 ms
		$6s^2 5d^2$	$^3F_2$	9.00[−2]	0.044	
$6s^2 5d6p$	$^1D_2$	$6s^2 5d^2$	$^3F_2$	1.68[+2]	0.791	4.71 ms
		$6s^2 5d^2$	$^3F_3$	4.44[+1]	0.209	
$6s^2 5d^2$	$^3F_3$	$6s^2 5d^2$	$^3F_2$	7.56[−3]	1.0	132 s
$6s^2 5d6p$	$^3D_2$	$6s^2 5d^2$	$^3F_2$	4.50[+3]	0.1059	23.5 μs
		$6s^2 5d^2$	$^3F_3$	3.79[+4]	0.8924	
		$6s^2 5d^2$	$^1D_2$	4.41[+1]	0.0010	
		$6s^2 5d^2$	$^3P_1$	2.75[+1]	0.0006	
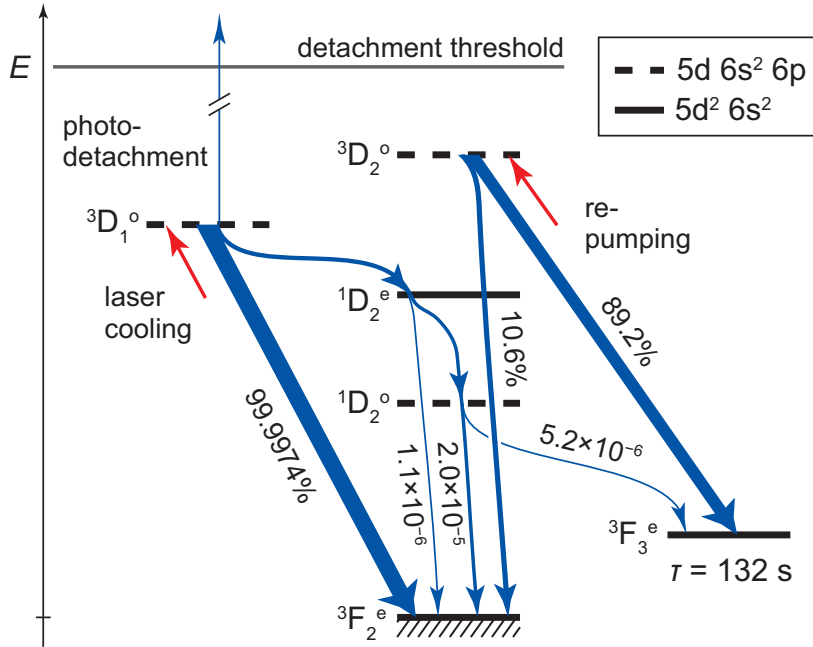
Figure 4.3: Partial energy level diagram of La$^-$ (energies to scale). The relevant decay branches from the $^3D_1^o$ excited state of the laser cooling transition, as well as from the $^3D_2^o$ excited state of the repumping transition, are indicated. Branchings at least two orders of magnitude smaller than those indicated have been neglected. Thicknesses of blue arrows are indicative of branching ratios, but not to scale.

82

previously assumed.

Another important question is the degree to which the cooling cycle is closed. We can fully deduce all relevant branchings from our present results, as illustrated in the partial energy level diagram of Fig. 4.3. The excited $^3D_1^o$ state will decay to the $^3F_2^e$ ground state in all but 2.6×10^{-5} of cases. However, only a total 5.2×10^{-6} branching to the $^3F_3^e$ state is potentially problematic, because that state cannot decay to the ground state by an allowed transition and is hence metastable ($\tau = 132$ s). If necessary, the $^3F_3^e \longrightarrow \, ^3D_2^o$ transition can be repumped, as shown in the figure.

Finally, photodetachment from the $^3D_1^o$ excited state may remove La$^-$ ions from the trap. The photodetachment cross-section is about five orders of magnitude smaller than that of resonant excitation. Its rate also depends on the time during which ions populate excited states and the laser power. Thus, the light power must be reduced to preserve a reasonable number of anions if many cycles are required, thus extending the cooling time by reducing the saturation level.

4.3   1-D laser cooling model

Considering the results presented in this thesis, we can now develop a simplified model for the cooling to assess the possible time scales for a first observation of laser cooling. To simplify the mathematical treatment, we will make the following approximations:

- There is only one spatial dimension. This can be compensated experimentally by illuminating the sample from three orthogonal directions; alternatively the cooling can be carried out in a trap where the motions are coupled, in which case the cooling times will be proportionally longer.

- The laser light has a homogenous intensity I interacting with the anions. The corresponding electric field is $E = \sqrt{2I/(\epsilon_0 c)}$;

- There is no hyperfine structure in the Doppler cooling transition, and we only consider a three-level system with ground, excited and neutralized states (see. 2.2)

- We are interested in reaching a final temperature of the sample of 0.17 μK corresponding to the Doppler limit for La$^-$.

- The anions will populate one velocity class only. This assumption can be partially compensated by rescaling the timings for the coverage of the Doppler line by the laser to consider that only a fraction of the anions will be addressed at a time.

- All anions are in the ground state of the system in the beginning.

In our model the laser has the following properties:

- The frequency of the laser is $\nu \approx 96.592$ THz.

- The wave vector is $k = 2\pi/\nu$.

- The laser bandwidth is $\Gamma_{laser}/(2\pi) = 2$ MHz. This can be easily achieved by adding a modulation to the laser line selected according to the temperature we want to reach. To actually reach the Doppler limit in the experiment it is necessary to reduce the bandwidth from this value when at the La$^-$ ions are at approximately 0.5 K.

Finally, the La$^-$ ions have the following properties:

- The transition linewidth of the laser cooling transition is $\Gamma_s = 4.54 \times 10^4$ Hz.

- The cross-section for detachment from the excited state at the laser cooling frequency is $\sigma_d = 10^{-17}$ cm^2.

The first problem to address, before considering the cooling time, is the number of particles that will remain in the trap. It is in fact of no interest to pursue the cooling and find an empty trap in the end. Thus this condition is of primary importance. The photodetachment rate Γ_d of anions from the excited state can be calculated as

$$\Gamma_d = \frac{\sigma_d I}{h\nu} \ . \tag{4.1}$$

This rate depends on the amount of light that is sent into the apparatus, and if the cooling should take a long time because of a high starting temperature, it follows that the power needs to be reduced such that less excited anions are lost. We require that at least a fraction $1/e$ of the original sample of anions remain after N cooling cycles. The fraction $1/e$ imposes the condition $N\Gamma_d = \Gamma_s$ and fixes the light intensity at

$$I = \frac{\Gamma_s h\nu}{\sigma_d} \frac{1}{N} \ . \tag{4.2}$$

The excitation rate of anions from the ground state to the excited state is given by

$$\Gamma_e = \frac{\Omega^2}{\Gamma_{laser} + \Gamma_s} \ , \tag{4.3}$$

where Ω is the Rabi frequency. The Rabi frequency can be calculated from:

$$\Omega = -\frac{E}{\hbar} \sqrt{\hbar\Gamma_s 3\pi \frac{\epsilon_0}{k^3}} \ . \tag{4.4}$$

Each cooling cycle lasts on average a time $\tau_{cool} = 1/\Gamma_s + 1/\Gamma_e$ and removes a momentum $\delta p = \hbar k$ from the anion. We can also convert the momentum to temperature by using

$$\frac{p^2}{2m} = k_B T \ . \tag{4.5}$$

Therefore to reduce the temperature to T_{low} we need to take out of the system a total momentum difference of $\Delta p = \sqrt{2mk_B}\left(\sqrt{T} - \sqrt{T_{low}}\right)$ that can be used to determine the number of cycles per anion:

$$N = \frac{\Delta p}{\delta p} = \sqrt{2mk_B} \frac{\sqrt{T} - \sqrt{T_{low}}}{\hbar k} \ . \tag{4.6}$$

In the case the lower temperature is the Doppler limit $T_{low} = \hbar\Gamma_s/(2k_B) \approx 0.17\,\mu$K. A rough correction factor due to the Doppler coverage of the line is

$$\frac{\Delta\nu_{FWHM}}{\Gamma_{laser}} = \frac{\nu}{\Gamma_{laser}} \sqrt{\frac{8k_B T \log 2}{mc^2}} \ . \tag{4.7}$$

Finally, the cooling time can be approximated by

$$t_{cooling} = N\left(\frac{1}{\Gamma_e} + \frac{1}{\Gamma_s}\right)\frac{\Delta\nu_{FWHM}}{\Gamma_{laser}} \ . \tag{4.8}$$

To distinguish the situation when no repumping laser is present, we have to take into account the branching ratio q towards the dark state. Calculating the number of cycles is important to evaluate how may ions are lost from the cooling cycles and are not participating to the cooling. Pumping the ions into dark states of the system may in fact occur. The larger the number of ions in the dark state, the worse the situation becomes, since those atoms have to be cooled by sympathetic interaction with the
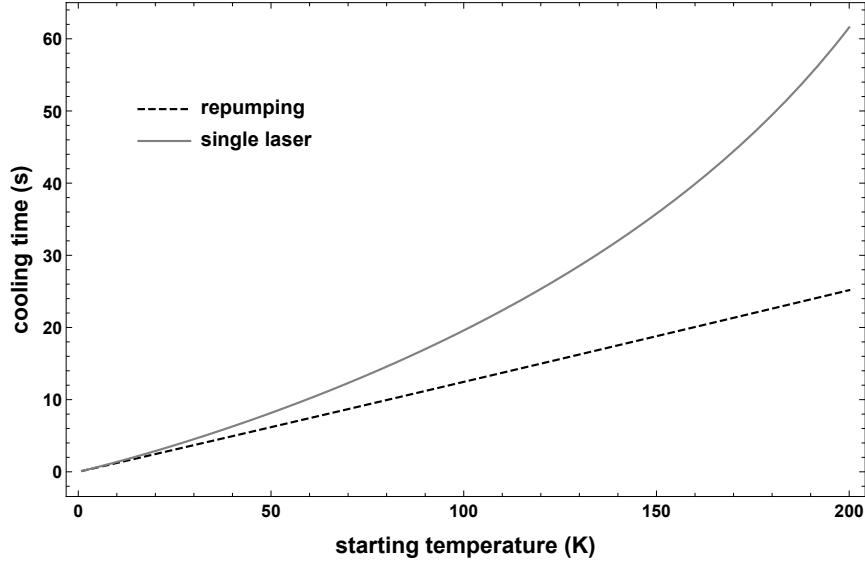
Figure 4.4: 1-D cooling times for La$^-$ anions aiming to a final temperature of 0.17 μK (Doppler limit). The curve *single laser* assumes no repumping on the dark state $^3F_3^e$ state while the curve *repumping* assumes that no anion is lost due to the presence of dark states.

still interacting ones. It follows that at each cycle slightly less momentum is taken away on average since some anions no longer interact with the light. The total amount of momentum removed after N' cycles can be calculated as

$$\Delta p' = \sum_{n=0}^{N'-1} \delta p(1-q)^n = \frac{\delta p}{q}\left(1 - (1-q)^{N'}\right) . \tag{4.9}$$

The amount of momentum to be removed for a given initial temperature is fixed by Eq. 4.6. Thus we can calculate the number of cycles required without repumping using the relation $\Delta p = \Delta p'$ and obtain

$$N' = \frac{\log(1-qN)}{\log(1-q)} . \tag{4.10}$$

To summarize, we first target a starting temperature, this fixes the number of cycles required to slow down the anions. This value yields the intensity of the laser to obtain $1/e$ anions trapped at the end of the cooling cycle and, in turn, the intensity controls the overall speed of the process. The result of our calculation is presented in Fig. 4.4.

The branching ratio towards the dark state fixes the theoretical maximum temperature $T_{max} \approx 260$ K from which the cooling to the Doppler limit can be done without repumping neglecting the required time. At this temperature, if repumping is provided, the estimated cooling time is 30 s. At half of this temperature (130 K) cooling without repumping would take approximately 30 s, and only 15 s if rempumping is provided. However it might be necessary to aim for a shorter laser cooling timescale if other cooling/heating mechanisms are present. For example, if we would like to observe the process happening within 3 s, our calculation suggests that anions should start at a temperature $T < 24$ K with the repumping laser and at $T < 20$ K if only a single laser is adopted. These temperatures are close to those obtained in the Penning trap by using electrons as buffer medium but are at least two orders of magnitude smaller than the current values recorded in our Paul trap (5000 K). Therefore, further developments are needed to reduce the temperature of the anions in the magnetic-field-free region of the experiment.

Conclusion

Laser cooling was first theoretically studied and practically applied to neutral atoms and positive ions. Laser cooling of a negative ion species has not yet been achieved, but investigated theoretically and experimentally for atomic and, more recently, molecular systems [86]. Starting from these studies, the UNIC project pursued the cooling of negative atomic ions by first studying Os⁻ and then La⁻.

In this work, La⁻ was investigated via high-resolution in-flight laser spectroscopy, finding this anion suited for Doppler laser cooling. The experimental results combined with additional theoretical studies have made it possible to develop a cooling scheme for La⁻ in the absence of a magnetic field. We determined frequencies, transition rates and branching ratios necessary for the implementation of Doppler laser cooling, overcoming the limitations imposed by the nuclear spin ($I = 7/2$) of the only stable isotope of lanthanum ^{139}La. During this thesis the hyperfine structure of the laser cooling transition $^3F_2^e \longrightarrow {}^3D_1^o$ was resolved around the center-of-gravity frequency 96.592 713(52)(75) THz and a spontaneous lifetime of the transition of $\tau = 20.4(2.1)$ μs was determined.

The presence of two loss channels is detrimental to the laser cooling application. One is the $^3F_3^e$ dark state of the system located in the same fine structure multiplet as the ground state. The second is a possible neutralization of La⁻ by absorbing a second photon of the cooling laser while in the excited state, resulting in photodetachment. These two problems impose an initial temperature on the order of tens of kelvin before starting to Doppler laser cool the anions. Our 1-D model indicates that it will take about 8 s, starting from the initial temperature of 50 K, to obtain a final temperature of 0.17 μK (Doppler limit).

Observations of an atomic system for such a long time are possible by storing anions in a trap. Two possible traps have been considered and tested experimentally during this work, a Penning trap and a Paul trap. In both traps the ions were axially confined by a DC potential well, while radially the two confinement principles are different. The DC well closed by two lateral potential barriers was found convenient for capturing the cloud of ions as well as for the subsequent handling of the cloud for measuring purposes. In capturing ions the potential well was biased to a potential sufficient to reduce the incoming ion energy of some keV to few eV when captured. The trapping was realized in a static trap condition, allowing ions to enter the trap and to partly lose and partly randomize their coherent momentum, finally becoming captured.

Once captured the anions must be pre-cooled to reach a temperature suitable for the further step of laser cooling. The ions can lose their energy by evaporating the hottest anions with a photodetachment cooling scheme as suggested in [19]. However, this process has the drawback of reducing the number of ions useful for subsequent laser cooling. The second mechanism, applied in this work, was to combine ions and electrons in the strong magnetic field of a Penning trap for sympathetic cooling. By using electrons as a buffer medium, millions of anions can be trapped in a few minutes and thermalized to the temperature of the surrounding environment (the temperature of the electrodes was $\approx$ 30 K). This would constitute a good starting condition to attempt laser cooling, if the magnetic field were not present. Thus a possible solution to this problem is to transfer ions from the Penning trap to a near Paul trap, magnetically shielded, where laser cooling could be carried out. A combined RF and Penning trap could also be considered where the magnetic field is switched off after electron cooling.

Our experimental configuration favors antiproton capture and integration in the experiment at the AD at CERN. The design would allow combining antiprotons with electrons and anions such as to cool antiprotons to sub-kelvin temperatures by laser cooling the anions. Finally, it is possible to eliminate the La$^-$ by photodetachment or by briefly lowering the trapping barriers and letting antiprotons escape from the trap since their mass is 139 times lower than that of the anions. The target temperature for that experiment would be 0.1 K since it corresponds to the recoil limit of antihydrogen formation via positronium charge exchange.

The radiofrequency trap could be designed with a larger number of poles than a quadrupole trap. We suggest a trap made of wires, similar to the standard design with 22 poles of Ref. [27]. In this kind of traps, a series of wires/rods are mounted in a cylindrical geometry. Like in the quadrupole trap, a radiofrequency of a few MHz, with phase shift π, is applied to neighboring wires (poles). The symmetric arrangement of the wires resembles the cylindrical geometry of Penning trap electrodes and generates a large RF-free region near the axis. The symmetry allows the RF field of neighboring electrodes to compensate each other in the axial region. Thus, if the trap is used in a magnetic field, it may emulate the behavior of Penning trap electrodes better than a quadrupole design. This would favor the thermalization of electrons that otherwise would be heated by the RF field. In the absence of a magnetic field, and for a given RF amplitude, the trap depth of multipolar traps is shallower than the quadrupole one but still enough at a temperature of a few tens of kelvin.

Concerning antihydrogen studies, the transparency provided by the wire design favors the transfer of positronium from a porous silica target which converts e$^+$ into Ps [57]. It is a well-established technique that produces positronium by implanting e$^+$ into solid targets which subsequently emit Ps with high efficiency ($\approx$30%). These targets cannot occupy the trap volume, and a certain transparency of the trap walls to Ps is required for the Ps to reach $\bar{p}$ in flight. The multipole trap also has a better mass acceptance than a quadrupolar trap, readily confining both heavy anions like La$^-$ and antiprotons. Finally, the internal region, free from an RF field, is useful for precision measurement on antihydrogen, which can be excited by lasers without the influence of trapping fields.

Appendix A

A.1 Trap compiler manual v1.1

The trap compiler is used to create a program (pulse sequence and timing) to be loaded in the Pulse Card when it is in Slave mode. This pulse program is then executed by the Pulse Card when it is in Master Mode.

The compiler performs the following operations

- reads the script

- translates the script into a sequence of pulses

- download program and starts the Pulse Card

Scripts are text files denoted by extension ".txe" (Please use paths, including names. Spaces are not allowed). In the following examples italics indicates that the character in the word can be changed at will. To run the compiler use the following shell commands:

> trap_compiler_v_1_1.exe *namescript*.txe *outputfile*.txt

Or

> trap_compiler.exe *namemainfunction*.txe

This is equivalent to drag and drop "*namemainfunction*.txe" on the icon of "trap_compiler_v_1_1.exe". In the latter case the output log is sent to standard output. The log file produced by the compiler shows the compilation step performed to setup the pulse sequence. The compilation steps are:

- Main script open

- Function find and replace in the main script

- Variable to numbers calculation and loop unrolling

- Loading the basic statements into a time ordered table

- Generate pulse sequence for the 24 channels

- Download the sequence to the card and start execution

The configuration file "trap_compiler_config.txt" that is in the same folder of the compiler is provided to modify the basic behavior of the compiler. Command lines in this file are:

> function_directory   *functiondirectory*
> end_behaviour   *status*

Use tab as separator. The first line is used to specify where the functions should be read. The second line is used to specify if the program should stop or start again from the beginning as the actual sequence of pulses terminates. In place of *status* use

- "stop". It will stop the sequence at the end of execution

- "infinite_loop". It will make the sequence restart forever. In this case first and last statuses must be the same. The last status defines when the next repetition of the program starts.

Basic statement

A statement (or instruction) is a line of script. Each line is parsed as a different instruction. The basic statement is like the one in the following example:

1000, 5, 0

The statement means. At absolute time 1000 ns the logic output of channel 5 is set to 0. The following conditions apply:

- Time should be an integer number in ns

- The channel number should be any integer number x such that $1 <= x <= 24$ (corresponding to the output channels of the card)

- The output value to be set can be only 0 or 1

The program is reduced to basic statements before interpreting any pulse sequence.

Absolute time is only for reference and does have nothing to share with the time the pulse sequence is started. Negative numbers are allowed as absolute time. After the reduction to basic statements the least time is set to zero and the others adjusted accordingly. Time order of the basic statements is performed before sending the commands to the card, so it is allowed to write basic statements not in time order. Minimum time precision is 10 ns, however no pulses shorter than 50 ns are allowed. For example it is allowed to ask for 60 ns square pulse, but neither 40 ns nor 61 ns.

Variables

The user can define variables. They are considered as integer values with 64 bit. Allowed operations among variables are

- "+", "-", "*", "/", "&&", "||" , "?:" (ternary operator C)

- Priority operators "(", ")" are allowed as well

Allowed characters in variables names are "a-z", "A-Z", "0-9", "_". Numeric only names are not allowed. Use assignment statement to define or change the value of a variable.

Assignment

Code examples of the assignment statements are:

Varold = 100
Varnew = Varold

In the example there are 2 variables named "Varold" and "Varnew". Both have value 100. The order of the two lines matters: first the value of 100 is given to "Varold" and only later assigned to "Varnew". The character "=" can only be used in this way. Right to "=" only a mathematical expression leading to a numeric value can be used

Function

The statement that starts a script is as follows:

> function *namefunction*[*var_1*, *var_2*, *var_3*]

namefunction must be equal to the filename (without extension) that contains the script. The keyword function is used both to

- Identify that the file is a script

- Find the first code line

- Look for "[", "]" which contains the number of variables to be passed to the function-script. There are no limitation to the number of variables.

Functions are resolved by string substitution of their content in the main program. Please note the following consequences.

- Every variables defined internally to a function is global.

- Variables passed to a function will be substituted in the function during the string substitution process. This can create an unresolved conflict. For instance if a variable is modified inside a function, but a numerical constant is passed instead this might lead to unwanted behavior. It is recommended to use variable to be passed to a function and assume they might be end up modified inside since their value is global.

- Recursion is not allowed.

The main function that determines the general execution cannot have variables. There must be only one function per ".txe" file

Call

To use a function use the following statement

> call *namefunction*[*var_1*, *var_2*, *var_3*]

This instruction string-copy the content of ".*functiondirectory**namefunction*.txe" into the script. Only variables names are searched and replaced to match the names of the calling script. Warning! Any variable defined in a called function will become global. Conflicts are not detected.

Loop

Batched operations has the following syntax:

> loop 5
> *any_valid_statement_1*
> *any_valid_statement_2*
> . . .
> endloop

In the example the statements between "loop" and "endloop" are copied 5 times.

Hardware loop

To repeat several times operations without saturating the card memory it is possible to implement hardware based loops. The statements are similar to loop statements with the following modifications

- "loop" $\longrightarrow$ "hardwareloop"

- "endloop" $\longrightarrow$ "endhardwareloop"

The following rules applies

- Nested hardware loops are not allowed.

- Hardaware loops must be isolated in time for their entire execution. No external statement can be executed in between. This check is not performed by the compiler and might lead to undefined behavior.

- Between two hardware loops there must be at least a basic statement.

- The statements inside the hardware loop are intended to program the first cycle of the hardware loop.

- The first and the last statements output status of the card in the hardware loop must be equal. The time of the last status define the start of the next cycle.

Comment statement

Any empty line or a line which contains "%" will be ignored.

Examples

Some example will be given with reference to experimental situation.

*

Command to computer This example set the output of channel 5 to 1 for 1 μs and then send to the computer the command to exit Slave Mode. In the example this command has code number 1 in one byte representation. Main script

```
function procedure[]
time = 10
time, 5, 1
time+1000, 5, 0
call end[time]


function end[time]
call pc_command[time,0,0,0,0,0,0,0,1]


function pc_command[time,v7,v6,v5,v4,v3,v2,v1,v0]
time,pc_channel_7,v7
time,pc_channel_6,v6
time,pc_channel_5,v5
```

```
time,pc_channel_4,v4
time,pc_channel_3,v3
time,pc_channel_2,v2
time,pc_channel_1,v1
time,pc_channel_0,v0
```

Train of pulses

Pulsing of the last endcap in front of the MCP can be realized with the following scripts. Main script

```
function procedure[]
time = 1000
nloop = 5
loop nloop
    call endcap2[time, 1]
    time = time  1000
    call endcap2[time, 0]
    time = time  1000
endloop
call end[time]
```

Function script

```
function endcap2[time, status]
time, channel_driving_endcap2_switch, status
```

The example will produce a train of 5 pulses. We performed scan operation with similar script: in the example it is necessary to produce several files modifying the line "nloop = 5" to obtain a train of pulses with different number of pulses from 5.

Trapping example

The sorting of the instructions in time can simplify the handling of the parallel work-flow of different devices during procedure execution. A typical example is the acquisition of the image from the MCP detector. In this case the following events need to happen in sequence:

1. the computer starts the camera program waiting for an image to come,

2. MCP voltage is turned on,

3. trigger of the camera,

4. MCP voltage is turned off.

This type of sequence is handled sending three different commands at different times to the computer: 1, 2, and 4; and one of the output channels of the pulse card is connected directly to the camera to perform 3. The computer commands can request a certain amount of time to be executed and to account for this time a function can be written so that at a definite time *time* after the beginning the snapshot will be acquired. The functions may look like this

```
function camera_snapshot_MCP[time]
% send command to computer to wait for a picture to be transferred from the camera
call camera_snapshot[time-5*s]
% send command to computer to power MCP detector
call MCPimaging_on[time-2*s]
% send trigger command to the camera
call camera_trigger[time]
% send command to computer to turn off MCP detector power supply
call MCPimaging_off[time+1*s]
```

```
    function camera_trigger[time]
% triggering camera with falling edge
time - 100*ms, camera_trigger_channel, 1
% 50 microsecond is the jitter from the manual of the camera
time - 50*us, camera_trigger_channel, 0
```

Function scripts sending a command to the computer () are equivalent to the "end" function already described.

The operation of acquiring a picture is bounded to something happening into the experiment, like releasing trapped particle by switching the final endcap. The switch is controlled through another output of the pulse card and a new instruction

5. switch the endcap

needs to be introduced between 3 and 4. The time sorting of the instructions avoids the programmer to actively code the sequence. In fact, instruction set 1-4 can be written into a function to be used in different experiments so that at a certain time *time* the picture will be acquired. The time sorting of the instruction will insert instruction 5 between 3 and 4 automatically.

A sample program that streaming the beam of anions trough the trap attempting to load ions for 5 seconds, storing them for 10 and measuring the content may look like the following

```
function procedure[]
% quantities definition
ns = 1
us = 1000*ns
ms = 1000*us
s = 1000*ms
% logic statuses definition
status_trap_close = 0
status_trap_open = 1
beam_on = 1
beam_off = 0
% experimental timing definition
loading_time = 5*s
storage_time = 10*s
%————————————————
% EXECUTION
% close the trap
time = 1*s
```

```
call endcap1[time,status_trap_close]
call endcap2[time,status_trap_close]
time = time + 1*us
% send anion beam towards the trap
call beam[time, beam_on]
time = time + loading_time
call beam[time, beam_off]
% store particles
time = time + storage_time
% release particles and acquire image
call camera_snapshot_MCP[time]
call endcap2[time,status_trap_open]
% end acquisition
time = time + 2*s
call end[time]
```

The function "endcap1" and "beam" are similar to the function "endcap2" already described.

For practical reason we also coded some standard function to define the wiring of the trap to the channels that were always called at the beginning of each main procedure.

A.2 Counting detectors

Detectors like channeltrons or MCPs may be used to detect single particle and to measure the number of incoming particles in a definite amount of time. Often, dealing with single event, the amplitude of the signal is disregarded favoring counting detection via a threshold definition. If the amplified current pulse exceeds the threshold the event is counted.

Count acquisition may be affected by counting error induced by pileup events during the dead time of the instrument. This fact may be taken into account adjusting the count value and its uncertainty. If the pileup is present more than one particle arrives within the detection time while only one event may be recorded. Assuming that the probability per unit time of receiving one event is constant and that event timing is independent, then the probability to receive n events during unit time interval follows a Poisson distribution of average λ :

$$P(n) = e^{-\lambda} \frac{\lambda^n}{n!}$$

This probability defines also the probability to receive no events in the unit time which is

$$P(n = 0) = p = e^{-\lambda}$$

Since count rate is uncertain due to pile up it is more convenient to determine lambda from the rate events do not occur.

Calling f the number of registered events and N the total number of acquisition we may numerically approximate $p = 1 - f/N$. This gives for the average λ and the its uncertainty $\Delta\lambda$:

$$\lambda = -\log\left(1 - \frac{f}{N}\right) \qquad \Delta\lambda = \frac{\sigma_p}{p} = \sqrt{\frac{f}{N - f}}$$

The number f can be rescaled for time intervals bigger than the relevant interval for pileup (dead time of the instrument) by rescaling the measured number of count F with the ratio of the dead time t against the interval size T :

$$f = F \frac{t}{T}$$

The count rate on the time base of the dead time and the associated uncertainty would be calculated as follows:

$$\lambda = -\log\left(1 - \frac{F}{N}\frac{t}{T}\right) \qquad \Delta\lambda = \frac{t\sqrt{F}}{NT - Ft}$$

A.3   Lens for imaging the MCP

A common problem found in experiments that acquire images from MCP detectors is to couple the appropriate lens to the camera sensor used for imaging. In our setup the distance of the MCP to the camera is fixed, as well as the dimension of the phosphor screen and the camera sensor. The camera is outside the vacuum chamber, mounted as close as possible to the detector to collect the maximum amount of light. The choice of the optimal lens to image the MCP is determined by the mutual dimension of the MCP and the camera sensor.

As usual we will call:
– p the distance of the lens to the MCP
– q the distance of the lens to the sensor
– k the MCP diameter
– h the length of one side of the sensor
– f the focal length of the lens

The thin lens formula that connects p, q and f is

$$\frac{1}{p} + \frac{1}{q} = \frac{1}{f}$$

Using ray trace approximation for central rays and the relation of similar triangles we can conclude that

$$\frac{k}{p} = \frac{h}{q}$$

Typically, p must be larger than the optical distance p_{min} measured from the MCP to the first point outside the vacuum chamber. The condition is imposed if the lens is intended to be outside the vacuum, possibly firmly attached directly to the camera. The optimal value for f is the one that leaves the camera as close as possible to the MCP to collect the highest amount of light. Therefore

$$f > p_{min} \frac{h}{h+k}$$

A.4 MCP imaging calibration

Microchannel Plate Detectors can transform particles entering each channel in a current of electrons amplified by avalanche multiplication due to the electrical polarization of the two-channel extremities. Placing a phosphor screen at the exit face of the MCP allows converting the amplified current emitted by each channel into light. In this section, we describe the calibration procedure to convert the fluorescence signal into particle numbers. These data were used counting gold ions.

The calibration was performed with ion energy of 1006 eV, and a vacuum of $7 \cdot 10^{-11}$ mbar. The calibration measurements consisted in registering the light produced by the gold beam coming directly from the Middleton source and impinging onto the MCP detector. By gating the incoming beam for a definite amount of time, the number of detectable ions was selected. In this way, the number of anions has been referred to the amount of recorded light. The MCP detector was polarized applying three voltages to its electrodes. The front electrode was connected to the vacuum chamber. The second electrode, which is the back face of the detector, was connected to a variable potential source, thus allowing a variable amplification gain. The third electrode, which is connected to the phosphor screen, was always polarized at 3.5 kV relatively to the second electrode.

The gain of the camera was chosen to maximize the signal to noise ratio by trapping electrons avoiding saturation of the MCP detector.

One hundred empty pictures were acquired for all gains and exposure times selected for the experiment to measure and subtract the average background in all experimental conditions. Data were further reduced by disregarding all information outside MCP screen area. In this way, only 83.5% of the square images (1600 by 1216) were used. To spread the incoming beam of ions on a large area, the trap electrodes have been used as defocusing element of the beamline.

The ion current was measured using the MCP front face as Faraday cup connecting its terminal to the ammeter. Two values of the current were recorded before and after the imaging data acquisition to ensure compatibility of the measurement set. The current before and after was found to be 1.548(6) nA and 1.543(6) nA respectively.

The avalanche gain in the microchannels depends exponentially on the biasing potential. Given V the biasing voltage, n the number of particles and L the light collected by the camera we assumed a model function like the following:

$$\log\left(\frac{L}{n}\right) = a_0 + a_1 V + a_2 V^2 \tag{A.1}$$

where a_0, a_1 and a_2 are coefficients to be determined. The coefficient a_2 was added to allow small deviations from a perfect exponential law. This function fits our data up to the limit of less than one particle per pixel. Below this threshold, a further correction is required to account for particle detection efficiency of the MCP evaluating the value of the detected anions from the luminosity integral over the entire image (Fig. A.2). We fitted ($a_0 = -36.6 \pm 0.2$, $a_1 = (3.96 \pm 0.04)10^{-2}$ V^{-1}, $a_2 = (9.1 \pm 0.2)10^{-6}$ V^{-2}). With those fitted parameters, we tried to correct the detection efficiency at a low count rate. By the previous function, a first estimated number of particle n' could be calculated for all the data recorded. Then, we grouped all data corresponding to the same number of impinging ions averaging those values. Comparing the estimated values with the real ones we calculated a second correcting function for our first estimated value to be used when the average number of particle per pixel would be less than unity:

$$n = n'\left(1 + \eta\, e^{-\gamma n'}\right) \tag{A.2}$$

We fitted the free coefficient η and γ in finding $\eta = -8(2)\,10^{-2}$ and $\gamma = -2.2(3)\,10^{-1}$.

To conclude, we performed the calibration on a logarithmic scale due to the known intrinsic property of the detector and this function assesses the number of particles within an order of magnitudes accuracy. The calibration function was then considered reliable to count anions down to an average of 10^{-2} particle per pixel.
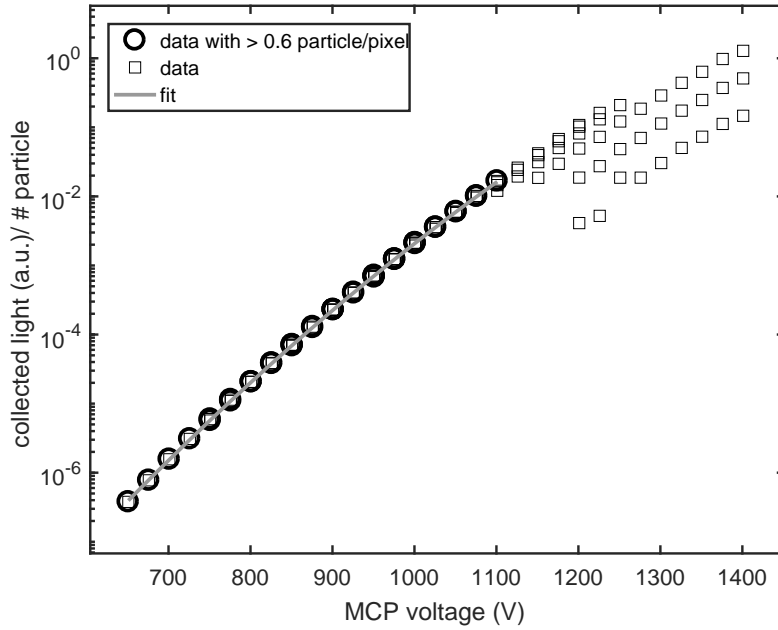
Figure A.1: Detected fluorescence normalized by the number of particle as a function of the voltage difference between MCP back and MCP front electrodes. The fit follow Eq. A.1 as described in the text Eq. A.1. The analytical fit was calculated in the range 700-1100 V where a minimum of 0.6 particle per pixel was detected.
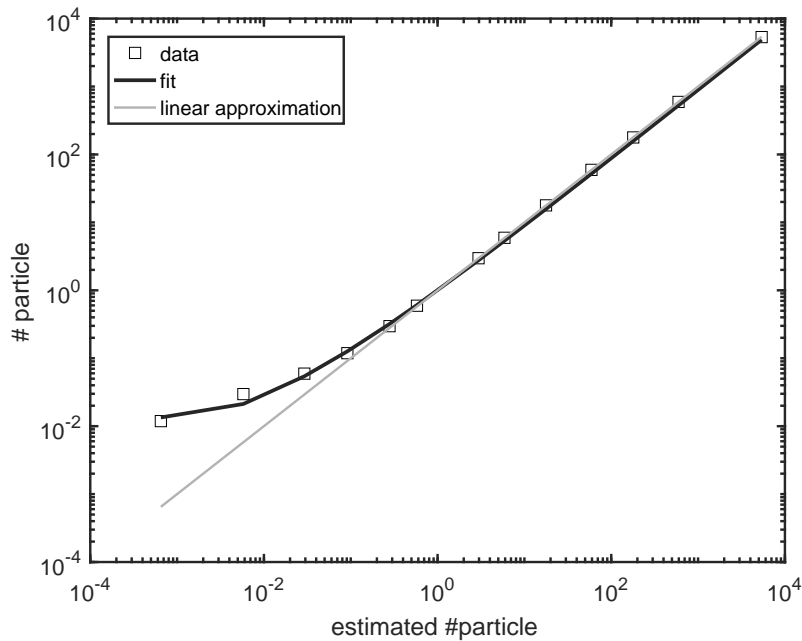

Figure A.2: The plot compares the number of detected ions using the approximation of Eq. A.1 against the real number of impinging ions. The scale is in particle per pixel. The second step of the calibration Eq. A.2 is the fit line. The correction takes into account the saturation at low particle number. The linear approximation follows the relation $n = n'$.
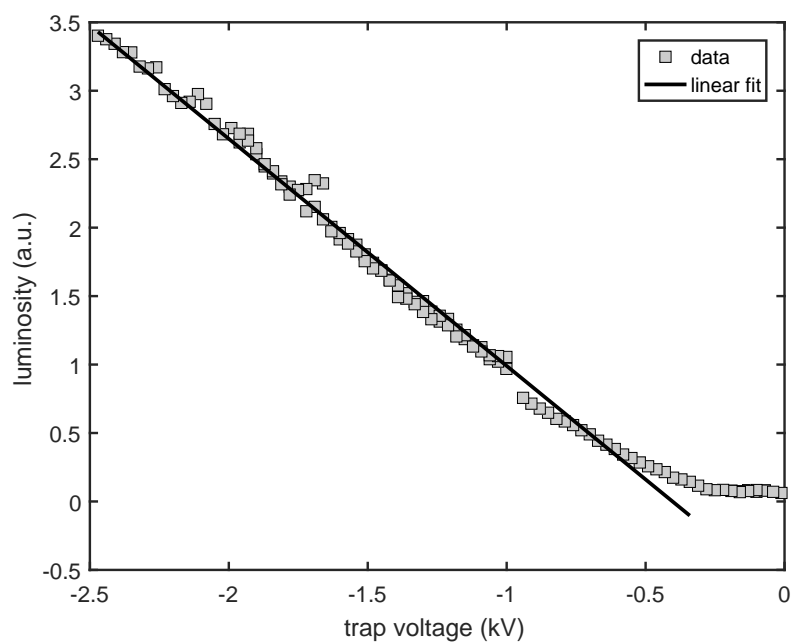
Figure A.3: Fluorescence signal obtained releasing anions from different reference voltage. The linear fit $y = ax+b$ gives $a = -6.7(2)10^2$ V^{-1} and $b = -1.66(6)$.

To account for different accelerating voltage, the fluorescence signal was further corrected in linear approximation using the data shown in Fig.A.3. The measurement was performed trapping a constant number of anions and releasing them towards the MCP at different reference voltages. The indicated trap voltage refers to the potential of the central electrode of the trap.

A.5 Electron release by central potential switching

In the text in Sec. 3.1 we described the pulsed procedure to release the electrons from the trap leaving the slower anions still confined. The electric potential on the front endcap is pulsed opening the trap from one side and observing trapped e$^-$ disappearing in less than 1 μs.

If the release is made by lowering the potential of the central electrode, electrons leave the trap according to a different timescale. To front, center, back electrodes (electrode numbers 8, 9, 10)[1] the DC potentials were applied -105 V, 0 V and -600 V respectively. In this configuration, the trap was loaded with electron and the plasma stored for 120 s. Then the central potential was switched to -420 V. With these potentials the electrons are free to leave exiting towards the front endcap direction. After a specified amount of time, the trap is restored to the original configuration, and the back electrode switched releasing the e$^-$ towards the imaging MCP for detection. Notwithstanding the similarity between the potential profile created by pulsing the endcap or the central electrode, the release time of the electron in the latter case was found much longer. After 130 μs we could still observe trapped electrons. The images (Fig. A.4) show that at the beginning the electrons spill out from the central volume of the cloud leaving a ring which in the long run becomes unstable. A study about similar instabilities in electron plasma can be found in Ref. [32]. Due to the larger release time, the technique was not considered in separating electrons from anions and was not further investigated.

---

[1]See Fig. 1.10.
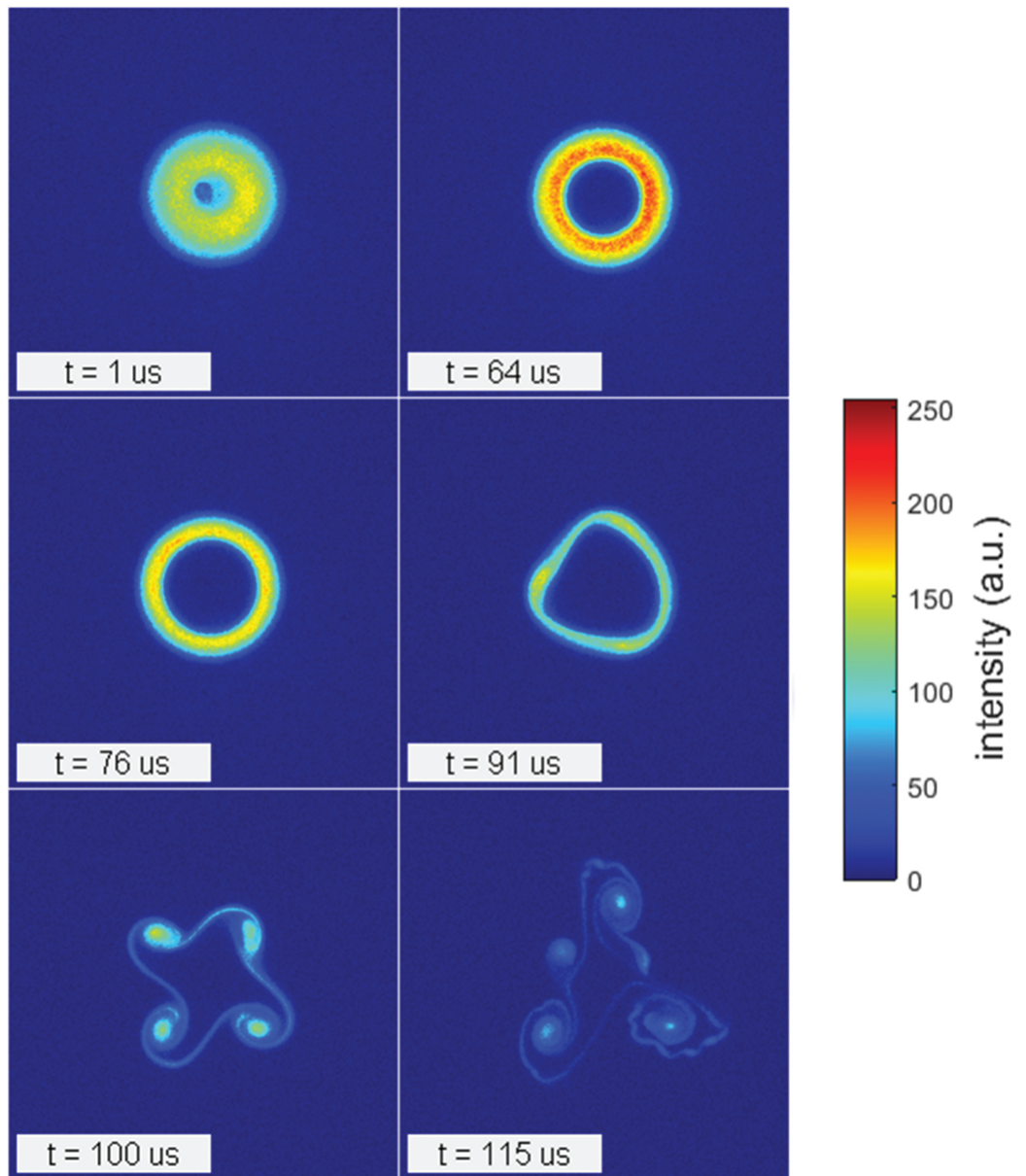
Figure A.4: Normalized MCP images of the electron plasma released by lowering the central potential. The e$^-$ leave the trap first in the center leaving a ring that collapse into vortexes. The indicated time is the time the central voltage is kept lower than the front voltage. All electrons leave the trap after 150 μs. The apparent hole in the middle of the plasma for the 1 μs image is a defect of the MCP detector.
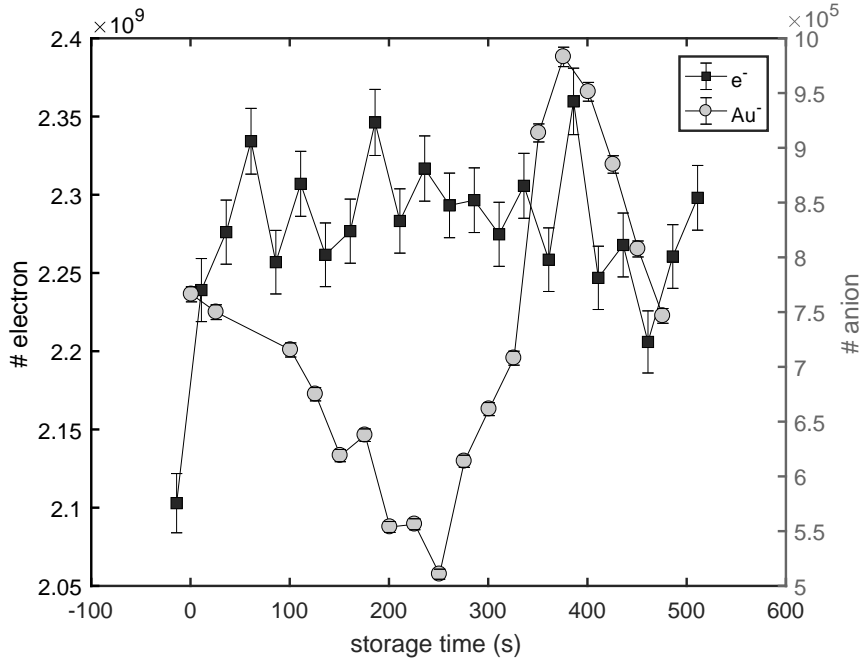
Figure A.5: Number of anions and electrons detected during the sympathetic cooling experiment. During the centrifugal separation of the two species there is an apparent increase in the number of anions.

A.6   Detected anions after e⁻ ejection from the Penning trap

In the text in Sec. 3.4 the sympathetic cooling of Au⁻ by an e⁻ plasma in the Penning trap is presented. Briefly, the anions are loaded in a dense plasma of electrons for 5 s, and the system is observed after different storage times. In the beginning, the number of anions decreases due to the collision-cooling process that destroys some anions. After 250 s the centrifugal separation occurs, and the two species separate: electrons remain close to the axis, and the heavier anions are dragged away from the axis. After the separation period (about 350-380 s), the anions distance from the axis increases and some particles are lost outside the detector area. During the separation, we observe an apparent increase of the number of anions (Fig. A.5). However, the number of anions is not expected to increase because no formation of heavy negative ion should occur. Thus we believe that this is a systematic bias due to the measurement scheme.

Has we have seen it is mandatory to remove electrons from the trap before the measuring phase of the anions since the number of anions is about $2 \cdot 10^3$ time smaller than the number of e⁻. Fortunately, the electron are hundreds of times faster than anions an a short voltage pulse to one endcap of the trap may be used to eject the electrons selectively (Sec. 3.1). Most the anions remain into the trap. However, if anions and electrons are spatially overlapped the electrons collide on the anions while accelerated on their way out. These collisions may lead to detachment of the extra electrons attached to the anions, thus reducing the number of detectable anions. With the centrifugal separation, tough, the two species occupy different regions and the electrons generate less collisions while expelled from the trap. The number of detected anions is therefore not increasing, but rather depending on the overlap of the electrons and anions. The data acquired in this experiment suggest data the pulse release of e⁻ can reduce the trapped anions by a factor of two because the detected number of particles doubles during the transition from $5.4(2) \cdot 10^5$ to $9.5(3) \cdot 10^5$.

Bibliography

[1]   Joseph A. Becker. "Thermionic and Adsorption Characteristics of Caesium on Tungsten and Oxidized Tungsten." In: *Phys. Rev.* 28 (2 1926), pp. 341–361.

[2]   A L Bennani, J Pebay, and B Nguyen. "Measurement of the absolute electron detection efficiency of a channel multiplier (channeltron)." In: *Journal of Physics E: Scientific Instruments* 6.11 (1973), p. 1077.

[3]   T. A. Patterson et al. "Resonances in Alkali Negative-Ion Photodetachment and Electron Affinities of the Corresponding Neutrals." In: *Phys. Rev. Lett.* 32 (5 1974), pp. 189–192.

[4]   H. H. Andersen. "Sputtering and Ion-Source Technology." In: *IEEE Transactions on Nuclear Science* 23.2 (1976), pp. 959–966.

[5]   G. Ihmels, E. Jaeschke, and R. Repnow. "Improvement of the emittance of a Middleton type sputter source." In: *Nuclear Instruments and Methods* 138.3 (1976), pp. 407 –410.

[6]   J. Slater et al. "Alkali negative ions. III. Multichannel photodetachment study of Cs^- and K^-." In: *Phys. Rev. A* 17 (1 1978), pp. 201–213.

[7]   T. M. O Neil. "Centrifugal separation of a multispecies pure ion plasma." In: *The Physics of Fluids* 24.8 (1981), pp. 1447–1451.

[8]   K.-H. Moebius and K. Blatt. "The source for negative sodium ions at the Heidelberg MP-tandem accelerator." In: *Nuclear Instruments and Methods in Physics Research* 225.2 (1984), pp. 293 –297.

[9]   A. E. Siegman. *Lasers / Anthony E. Siegman*. English. University Science Books Mill Valley, Calif, 1986, xxii, 1283 p. :

[10] J. L. Yntema and P. J. Billquist. "Formation of negative ions in Cs sputter sources." In: *Review of Scientific Instruments* 57.5 (1986), pp. 748–750.

[11] K. H. Chang et al. "Search for long-lived doubly charged negative atomic ions." In: *Phys. Rev. A* 35 (9 1987), pp. 3949–3951.

[12] N. N. Semashko et al. "Production of negative ions by double charge exchange and their acceleration." In: *AIP Conference Proceedings* 158.1 (1987), pp. 334–345.

[13] P. Baumann et al. "The Heidelberg Heavy Ion Test Storage Ring TSR." In: *Nuclear Instruments and Methods in Physics Research Section A: Accelerators, Spectrometers, Detectors and Associated Equipment* 268.2 (1988), pp. 531 –537.

[14] D J Larson et al. "Physics with Negative Ions in Ion Traps." In: *Physica Scripta* 1988.T22 (1988), p. 183.

[15] C. Meis, M. Desaintfuscien, and M. Jardino. "Analytical Calculation of the Space Charge Potential and the Temperature of Stored Ions in an rf Quadrupole Trap." In: *Appl. Phys. B* 45 (1988), p. 59.

[16] G. Gabrielse, L. Haarsma, and S.L. Rolston. "Open-endcap Penning traps for high precision experiments." In: *International Journal of Mass Spectrometry and Ion Processes* 88.2 (1989), pp. 319 –332.

[17] G. Gabrielse et al. "Cooling and slowing of trapped antiprotons below 100 meV." In: *Phys. Rev. Lett.* 63 (13 1989), pp. 1360–1363.

[18] R. Middleton. *A negative-ion cookbook*. Electronic version prepared by Michael Wiplich, Brookhaven National Laboratory, 1989.

[19] A Crubellier. "Theory of laser evaporative cooling of trapped negative ions. I. Harmonically bound ions and RF traps." In: *Journal of Physics B: Atomic, Molecular and Optical Physics* 23.20 (1990), p. 3585.

[20] Chris H. Greene. "Photoabsorption spectra of the heavy alkali-metal negative ions." In: *Phys. Rev. A* 42 (3 1990), pp. 1405–1415.

[21] Rollin.J.Parker. *Advances in Permanent Magnetism*. John Wiley & Sons, 1990.

[22] S. H. Vosko et al. "Theoretical study of even- and odd-parity states in La$^-$ and Ac$^-$: Evidence for the uniqueness of La$^-$." In: *Phys. Rev. A* 43 (11 1991), pp. 6389–6392.

[23] Guo-Zhong Li and G Werth. "The combined trap and some possible applications." In: *Physica Scripta* 46.6 (1992), p. 587.

[24] H.-A. Synal et al. "Carbon Clusters from a Cs-Sputter Ion Source." In: *Clustering Phenomena in Atoms and Nuclei: International Conference on Nuclear and Atomic Clusters, 1991, European Physical Society Topical Conference, Åbo Akademi, Turku, Finland, June 3–7, 1991*. Ed. by Mårten Brenner, Tom Lönnroth, and F. Bary Malik. Berlin, Heidelberg: Springer Berlin Heidelberg, 1992, pp. 453–453.

[25] Debasis Datta and Donald R. Beck. "Electron affinities of opposite-parity bound states in Th$^-$: Relativistic-configuration-interaction studies." In: *Phys. Rev. A* 50 (2 1994), pp. 1107–1111.

[26] Konstantin Dinov, Donald R. Beck, and Debasis Datta. "Electron affinities of six bound states of Ce$^-$ formed by attachment of 6p and 5d electrons to Ce." In: *Phys. Rev. A* 50 (2 1994), pp. 1144–1148.

[27] Dieter Gerlich. "Ion-neutral collisions in a 22-pole trap at very low energies." In: *Physica Scripta* 1995.T59 (1995), p. 256.

[28] X. Luo, X. Zhu, and K. et al. Gao. "Origin and manifestation of the anharmonic potential felt by an ion-cloud in an actual Paul trap." In: *Appl. Phys. B* 62 (1996), p. 421.

[29] T. Gudjons, P. Seibert, and G.Werth. "Influence of anharmonicities of a Paul trap potential on the motion of stored ions." In: *Appl. Phys. B* 65.1 (1997), pp. 57–62.

[30] Guo-Zhong Li, Shenheng Guan, and Alan G. Marshall. "Sympathetic cooling of trapped negative ions by self-cooled electrons in a fourier transform ion cyclotron resonance mass spectrometer." In: *Journal of the American Society for Mass Spectrometry* 8.8 (1997), pp. 793–800.

[31] Guo-Zhong Li et al. "Radiatively Self-Cooled Penning-Trapped Electrons: A New Way To Make Gas-Phase Negative Ions from Neutrals of Low Electron Affinity." In: *Journal of the American Chemical Society* 119.9 (1997), pp. 2267–2272.

[32] D. R. Durkin. *Experiments on 2D Vortex Patterns in a Malmberg-Penning Trap with a Photocathode*. 1998.

[33] M. Scheer et al. "Experimental Evidence that the $6s6p\,^3P_J$ States of Cs$^-$ Are Shape Resonances." In: *Phys. Rev. Lett.* 80 (4 1998), pp. 684–687.

[34] M.A van Eijkelenborg et al. "Ion dynamics in a novel linear combined trap." In: *International Journal of Mass Spectrometry* 188.3 (1999), pp. 155 –161.

[35] John David Jackson. *Classical electrodynamics*. 3rd ed. New York, NY: Wiley, 1999.

[36]   A. G. Libinson. "Tilt dependence of the secondary electron emission at low excitation energy." In: *Scanning* 21.1 (1999), pp. 23–26.

[37]   Steven M. O'Malley and Donald R. Beck. "Electron affinities and $E1$ f values for 11 bound states of La$^-$ formed by $6p$ and $5d$ attachment." In: *Phys. Rev. A* 60 (3 1999), pp. 2558–2561.

[38]   V. Baglin et al. "The Secondary electron yield of technical materials and its variation with surface treatments." In: (2000).

[39]   René C. Bilodeau and Harold K. Haugen. "Experimental Studies of Os$^-$: Observation of a Bound-Bound Electric Dipole Transition in an Atomic Negative Ion." In: *Phys. Rev. Lett.* 85 (3 2000), pp. 534–537.

[40]   M. Drewsen and A. Broner. "Harmonic linear Paul trap: Stability diagram and effective potentials." In: *Phys. Rev. A* 62.4 (2000), p. 045401.

[41]   E. M. Hollmann, F. Anderegg, and C. F. Driscoll. "Confinement and manipulation of non-neutral plasmas using rotating wall electric fields." In: *Physics of Plasmas* 7.7 (2000), pp. 2776–2789.

[42]   Steven M. O'Malley and Donald R. Beck. "Electron affinities and $E1f$ values for 15 bound states of Ce$^-$ formed by $6p$ and $5d$ attachment." In: *Phys. Rev. A* 61 (3 2000), p. 034501.

[43]   Y. Saitoh et al. "Production of Ce negative ions in a Cs sputter ion source." In: *Review of Scientific Instruments* 71.2 (2000), pp. 955–957.

[44]   Z. J. Ding, X. D. Tang, and R. Shimizu. "Monte Carlo study of secondary electron emission." In: *Journal of Applied Physics* 89.1 (2001), pp. 718–726.

[45]   Whikun Yi et al. "Study of the secondary-electron emission from thermally grown SiO2 films on Si." In: 397 (2001), pp. 170–175.

[46]   T. Andersen. "Atomic negative ions: structure, dynamics and collisions." In: *Physics Reports* 394.4 (2004), pp. 157 –313.

[47]   Andreas Osterwalder et al. "High resolution photodetachment spectroscopy of negative ions via slow photoelectron imaging." In: *The Journal of Chemical Physics* 121.13 (2004), pp. 6317–6322.

[48]   G.Werth F.G. Major V.N. Gheorghe. *Charged particle traps*. Springer, 2005.

[49]   Yasuo Kokubun Kenichi Iga. "Encyclopedic Handbook of Integrated Optics." In: CRC Press, 2005.

[50]   L. Suess, Y. Liu, and F. B. Dunning. "Selective removal of electrons from a Penning trap for negative ion autodetachment studies." In: *Review of Scientific Instruments* 76.2 (2005), p. 026116.

[51]   Simon Cotton. "Lanthanide and Actinide Chemistry." In: John Wiley & Sons, Ltd, 2006.

[52]   "Springer Handbook of Atomic, Molecular, and Optical Physics." In: *Springer Handbooks*. Ed. by Gordon W F Drake. Berlin, Heidelberg: Springer-Verlag New York, 2006.

[53]   Alban Kellerbauer and Jochen Walz. "A novel cooling scheme for antiprotons." In: *New Journal of Physics* 8.3 (2006), p. 45.

[54]   G. Dobrychev et al. "Proposal for the AEGIS experiment at the CERN Antiproton Decelerator (Antimatter Experiment: Gravity, Interferometry, Spectroscopy)." In: (2007).

[55]   J. Meier. *Matching the beam form a negative-ion source for capture in a Penning trap*. 2007.

[56]   C. W. Walter et al. "Infrared photodetachment of Ce$^-$: Threshold spectroscopy and resonance structure." In: *Phys. Rev. A* 76 (5 2007), p. 052702.

[57]   S. Mariazzi, A. Salemi, and R. S. Brusa. "Positronium cooling into nanopores and nanochannels by phonon scattering." In: *Phys. Rev. B* 78 (8 2008), p. 085428.

[58] Romain Ravaud et al. "Analytical Calculation of the Magnetic Field Created by Permanent-Magnet Rings." In: *IEEE Transactions on Magnetics, Institute of Electrical and Electronics Engineers* 44.8 (2008), pp. 1982–1989.

[59] C.G.H. Walker et al. "The secondary electron emission yield for 24 solid elements excited by primary electrons in the range 250-5000 eV: a theory/experiment comparison." In: *Scanning* 30.5 (2008), pp. 365–380.

[60] S. M. O'Malley and D. R. Beck. "Valence calculations of lanthanide anion binding energies: $6p$ and $6s$ attachments to $4f^m(5d + 6s + 6p)^3$ thresholds." In: *Phys. Rev. A* 79 (Jan. 2009), p. 012511.

[61] M. S. Safronova et al. "Development of a configuration-interaction plus all-order method for atomic calculations." In: *Phys. Rev. A* 80.1, 012516 (July 2009), p. 012516.

[62] U. Warring et al. "High-Resolution Laser Spectroscopy on the Negative Osmium Ion." In: *Phys. Rev. Lett.* 102 (4 2009), p. 043001.

[63] Ulrich Warring. *Laser Spectroscopy on Os⁻: A Prerequisite for the Laser Cooling of Atomic Anions*. University of Heidelberg, 2009.

[64] A. Fischer et al. "First Optical Hyperfine Structure Measurement in an Atomic Anion." In: *Phys. Rev. Lett.* 104 (7 2010), p. 073004.

[65] R. Flory, J. Ametepe, and B. Bowers. "A randomized, placebo-controlled trial of bright light and high-density negative air ions for treatment of Seasonal Affective Disorder." In: *Psychiatry Research* 177.1-2 (2010), pp. 101–108.

[66] G. Gabrielse et al. "Centrifugal Separation of Antiprotons and Electrons." In: *Phys. Rev. Lett.* 105 (21 2010), p. 213002.

[67] H. Kreckel et al. "A simple double-focusing electrostatic ion beam deflector." In: *Review of Scientific Instruments* 81.6 (2010), p. 063304.

[68] Steven M. O'Malley and Donald R. Beck. "Lifetimes and branching ratios of excited states in La⁻, Os⁻, Lu⁻, Lr⁻, and Pr⁻." In: *Phys. Rev. A* 81 (3 2010), p. 032503.

[69] Lin Pan and Donald R. Beck. "Candidates for laser cooling of atomic anions: La⁻ versus Os⁻." In: *Phys. Rev. A* 82 (1 2010), p. 014501.

[70] J. Pedregosa et al. "Anharmonic contributions in real {RF} linear quadrupole traps." In: *International Journal of Mass Spectrometry* 290.2-3 (2010), pp. 100–105.

[71] Daniel Rodríguez. "Production and investigations of negative osmium ions for fundamental applications: REOSTRAP." In: *Hyperfine Interactions* 196.1 (2010), pp. 253–260.

[72] G. B. Andresen et al. "Centrifugal Separation and Equilibration Dynamics in an Electron-Antiproton Plasma." In: *Phys. Rev. Lett.* 106 (14 2011), p. 145001.

[73] C. Diehl et al. "Ion optical design of a collinear laser-negative ion beam apparatus." In: *Review of Scientific Instruments* 82.5 (2011), p. 053302.

[74] A. Kellerbauer et al. "Isotope shift of the electric-dipole transition in Os⁻." In: *Phys. Rev. A* 84 (6 2011), p. 062510.

[75] A. Heilmann. *Production and characterization of a mass-separated lanthanum anion beam*. University of Heidelberg, 2012.

[76] M. Schwarz et al. "Cryogenic linear Paul trap for cold highly charged ion experiments." In: *Review of Scientific Instruments* 83.8 (2012), p. 083115.

[77] J. M. Camacho and V. Sosa. "Alternative method to calculate the magnetic field of permanent magnets with azimuthal symmetry." In: *Revista Mexicana de Fisica E* 59 (2013), pp. 8–17.

[78] D. H. E. Dubin. "Equilibrium and dynamics of multispecies nonneutral plasmas with a single sign of charge." In: *AIP Conference Proceedings* 1521.1 (2013), pp. 26–34.

[79] Shenglan Qiao. *Constructing a Linear Paul Trap System for Measuring Time-variation of the Electron-Proton Mass Ratio*. 2013.

[80] C. Amole et al. "The ALPHA antihydrogen trapping apparatus." In: *Nuclear Instruments and Methods in Physics Research Section A: Accelerators, Spectrometers, Detectors and Associated Equipment* 735 (2014), pp. 319 –340.

[81] A. Kellerbauer, A. Fischer, and U. Warring. "Measurement of the Zeeman effect in an atomic anion: Prospects for laser cooling of Os⁻." In: *Phys. Rev. A* 89 (4 2014), p. 043430.

[82] C. W. Walter et al. "Candidate for Laser Cooling of a Negative Ion: Observations of Bound-Bound Transitions in La⁻." In: *Phys. Rev. Lett.* 113 (6 2014), p. 063001.

[83] Ulmer S. et al. "High-precision comparison of the antiproton-to-proton charge-to-mass ratio." In: *Nature* 524 (7564 2015), pp. 196–199.

[84] E. Jordan. *High-resolution Doppler laser spectroscopy of the laser cooling candidate La-*. University of Heidelberg, 2015.

[85] E. Jordan et al. "High-Resolution Spectroscopy on the Laser-Cooling Candidate La⁻." In: *Phys. Rev. Lett.* 115 (11 2015), p. 113001.

[86] Pauline Yzombard et al. "Laser Cooling of Molecular Anions." In: *Phys. Rev. Lett.* 114 (21 2015), p. 213001.

[87] F. Anderegg. *Rotating Wall Technique and Centrifugal Separation*. World Scientific Review, 2016, pp. 221–238.

[88] K. C. Chartkunchand et al. "Radiative lifetimes of the bound excited states of Pt⁻." In: *Phys. Rev. A* 94 (3 2016), p. 032501.

[89] R. von Hahn et al. "The cryogenic storage ring CSR." In: *Review of Scientific Instruments* 87.6 (2016), p. 063115.

[90] Eric R. Hudson. "Sympathetic cooling of molecular ions with ultracold atoms." In: *EPJ Techniques and Instrumentation* 3.1 (2016), p. 8.

[91] C. Koenig. *Trapping of Negative Gold Ions in a Penning Trap*. 2016.

[92] D. Krasnický et al. "Cross section for Rydberg antihydrogen production via charge exchange between Rydberg positroniums and antiprotons in a magnetic field." In: *Phys. Rev. A* 94 (2 2016), p. 022714.

[93] Kensei Kitajima et al. "Mass spectrometric study of negative secondary ions emitted from ethanol microdroplet surfaces by fast heavy ions." In: *The 30th International Conference on Photonic, Electronic and Atomic Collisions (ICPEAC XXX)*. Cairns, Australia, 2017.

[94] E.S. Endres et al. "Incomplete rotational cooling in a 22-pole ion trap." In: *Journal of Molecular Spectroscopy* 332.Supplement C (2017). Molecular Spectroscopy in Traps, pp. 134 –138.

[95] S. Erlewein. *Trapping of gold anions in a linear Paul trap*. 2017.

[96] Thomas J. Millar, Catherine Walsh, and Thomas A. Field. "Negative Ions in Space." In: *Chemical Reviews* 117.3 (2017). PMID: 28112897, pp. 1765–1795.

[97] David H. Dowell. "ELECTRON EMISSION AND CATHODE EMITTANCE." In: ed. by Stanford Linear Accelerator Center.

[98] lenntech. *Osmium - Os*. URL: http://www.lenntech.com/periodic/elements/os.htm#ixzz4thrVnWMX.

[99] *Risheng Magnets*. URL: http://www.rishengmagnets.com/.

Acknowledgment

I feel lucky to have had the opportunity to work with Alban Kellerbauer for my doctoral studies dissertation, and I would like to thank him for his outstanding support. He agreed to take me on as a Ph.D. student and encouraged me to pursue my ideas. I have never met a more reliable supervisor, he always paid attention to the people in the group and created the ideal environment to work on the project. I am grateful for all the thorough and precious suggestions he gave me to improve this dissertation.

Vielen Dank to my colleague and friend Elena Jordan with whom I worked during the first years of this thesis. We worked together during some night of data taking on the spectroscopy experiment, and we always pushed each other to obtain results. She also spent some time to proofread part of this dissertation.

Many thanks go to the students that made their university theses in the group. Charlotte König made her bachelor degree thesis working on the Penning trap results and helped assembling the high voltage platform for the trap system. Stefan Erlewein pursued his Master thesis in the group, and I had the pleasure not only to closely work with him in the lab on the Paul trap but also to meet him the air. He gave me some good pieces of advice to improve the sections dedicated to the Paul trap.

Merci beaucoup to Pauline Yzombard for participating in the last months of lab work. All discussions, suggestions and the Wolfram Mathematica scripts were extremely useful to improve this thesis.

Thanks to Aurelian, Kristin, Lena and Anika and all the bachelor students which I tried to entertain with some experiments at MPIK by being enthusiast about physics: I really had a lot of fun.

I am grateful to all my colleagues at the Max-Planck-Institut für Kernphysik and of the AEgIS experiment. I always felt welcome in opening a scientific discussion with everyone and free to ask any questions. Special thanks go to Jose R. Crespo L.-U. for giving us the channeltron detector on a late Friday afternoon and, later, the quadrupole mass filter to which the linear Paul trap is inspired.

The MPIK accelerator group and workshop always provided outstanding assistance with the ion source and the manufacturing of the critical part of the experimental setup. I would like to thank all people involved, in particular: Thorsten Spranz, Frank Müller, Manfred König, Felix Metz and Peter Gahn.

The European Research Council program (ERC) supported this study for two years; one year was founded by the The International Max Planck Research School for Quantum Dynamics in Physics, Chemistry and Biology (IMPRS-QD) and the final two years has been supported by the Max Planck Gesellschaft (MPG).

Declaration

Ich versichere, dass ich diese Arbeit selbstständig verfasst und keine anderen als die angegebenen Quellen und Hilfsmittel benutzt habe.

Heidelberg, den 05.02.2018,

Giovanni Cerchiari